SEARCH FOR TEV GAMMA-RAY EMISSION FROM NEARBY STARBURST GALAXIES

by

Tomoyuki Nagai

A dissertation submitted to the faculty of
The University of Utah
in partial fulfillment of the requirements for the degree of

Doctor of Philosophy

Department of Physics

The University of Utah

August 2005

UMI Number: 3174938

THE UNIVERSITY OF UTAH GRADUATE SCHOOL

SUPERVISORY COMMITTEE APPROVAL

of a dissertation submitted by

Tomoyuki Nagai

This dissertation has been read by each member of the following supervisory committee and by majority vote has been found to be satisfactory.

3/9/2005

Chair: Vladimir Vassiliev

3/9/2005

David Kieda

3/9/2005

Yong-Shi Wu

3/9/2005

Benjamin Bromley

3/9/2005

Jingyi Zhu

THE UNIVERSITY OF UTAH GRADUATE SCHOOL

FINAL READING APPROVAL

To the Graduate Council of the University of Utah:

I have read the dissertation of Tomoyuki Nagai in its final form and have found that (1) its format, citations, and bibliographic style are consistent and acceptable; (2) its illustrative materials including figures, tables, and charts are in place; and (3) the final manuscript is satisfactory to the supervisory committee and is ready for submission to The Graduate School.

5/29/2005
Date

Vladimir Vassiliev
Chair, Supervisory Committee

Approved for the Major Department

Pierre Sokolsky
Chair/Dean

Approved for the Graduate Council

David S. Chapman
Dean of The Graduate School

ABSTRACT

Observations of four starburst galaxies (SBGs), which are IC342, M81, M82, and NGC3079, have been conducted with the Whipple 10-m gamma-ray telescope from January 2001 to March 2004. A search was made for TeV gamma-ray radiation from cosmic ray (CR) interactions with the local ambient gas in the galaxies. SBGs are galaxies that have regions of intensive star formation often associated with high density interstellar medium (ISM) and a supernova (SN) rate 10 to 100 times that of the Milky Way. These regions are expected to have a high CR production and interaction rate, which may result in a large flux of gamma rays with energies between 100 MeV and 100 TeV. It has long been thought that CRs are accelerated in the strong shocks formed in supernova remnants (SNRs), producing large fluxes of gamma rays. However, the gamma-ray production mechanism in the detected SNRs has not been unambiguously identified with secondary neutral pion decay resulting from CR interactions, or with Inverse Compton (IC) scattering from ultra-relativistic electrons. SBGs provide another interesting site to test this SNR CR acceleration hypothesis. Selected SBGs are located just outside the Local Group, at a distance of a few Mpc, sufficiently close that attenuation by a distance factor will be small and the very high energy (VHE) gamma-ray flux may still be detectable. As part of this work, the fluxes of VHE gamma rays from a number of SBGs were estimated by extrapolation from the known CR spectrum and SN rate of the Milky Way. A new analysis method was developed allowing for the unknown spectral properties of the sources by utilizing a multidimensional maximal likelihood method (MLM). The results of applying this method and the standard Whipple analysis method to the observations are presented. No flux is detected, and an upper limit on the emission rate from each source is calculated. These limits constrain only the most extreme predictions. Predictions for repeated observations with a more

sensitive, next-generation ground-based gamma-ray instrument, such as VERITAS, are made.

To my family and friends

CONTENTS

LIST OF TABLES

ACKNOWLEDGEMENTS

I am greatly indebted to my thesis supervisor, Dr. Vladimir Vassiliev, for his support, guidance, and encouragement throughout my graduate school work. I also would like to thank his family, Ms. Larissa Vassilieva and Ms. Sofia Vassilieva, for wonderful friendship. My thesis advisory committee members, Dr. Dave Kieda, Dr. Yong-Shi Wu, Dr. Ben Bromley, and Dr. Jingyi Zhu, are greatly appreciated for helpful discussions and suggestions. Many thanks are owed to Dr. Trevor Weekes, and to my friends, Dr. Steve Fegan and Jeter Hall, for helpful suggestions. The support of the faculties and staff at the University of Utah physics department and at the University of California at Los Angeles is gratefully acknowledged. I would like to thank my great parents and sisters in Japan, who have been always supportive.

I appreciate the generous support and allocation of observing time from the Whipple 10-m telescope and VERITAS collaboration. I also acknowledge the technical assistance of E. Roache and J. Melnick.

This research is supported by the University of Utah and the National Science Foundation under NSF Grant 0079704. This research is also supported by grants from the U.S. Department of Energy, by Science Foundation Ireland, and PPARC in the UK, and by NSERC in Canada.

CHAPTER 1

INTRODUCTION

The goal of very high energy (VHE) gamma-ray astronomy is to contribute to the understanding nonthermal phenomena in the Universe. One particular question of interest is the origin of VHE cosmic rays (CRs), which has been long unsolved. This dissertation studies CRs generated in galaxies other than the Milky Way. Prime attention is devoted to the energy range from 200 GeV to 10 TeV. The means of study of extragalactic CRs are the observations of secondary gamma rays produced when CRs interact with interstellar medium (ISM). The relatively low opacity of the ISM to VHE photons allows them to escape from the region of CR generation and deliver information about the environment in which CRs are accelerated, propagated, and have interacted. In this dissertation, I briefly review the status of gamma-ray astronomy, including previously detected VHE sources. The relation between CR-induced gamma rays and the starburst regions of the galaxies is introduced. Finally, I study several target objects from which high energy radiation could be most likely observed. The dissertation is concluded with the discussion of directions in which this work can be further developed.

1.1 Gamma-ray Astronomy

As a window to the highest energy astrophysical phenomena in the Universe, VHE gamma-ray astronomy has become an exciting field over the last 30 years. Traditionally high energy X-ray and gamma-ray astronomy have been limited to space-based detectors due to the large opacity of the Earth's atmosphere to the high energy photons. However, the number of gamma rays falls rapidly with photon energy; the brightest source in the sky, the Crab Nebula, produces one photon with energy above 300 GeV per square meter every two days. At these energies, direct observations with reasonable size space-based instruments are impractical. On the other hand, photons with these large energies interact with the atmosphere and produce enough secondary particles which can be detected from the ground. For such observations, the atmosphere is used as a calorimeter providing information on the arriving direction and energy of primary gamma rays.

The pioneer of ground-based gamma-ray astronomy is the Whipple collaboration (USA, UK, and Ireland), which utilized an Imaging Atmospheric Čerenkov Telescope (IACT), and discovered the first source of the VHE gamma rays, the Crab Nebula, and subsequently several extragalactic sources. During the last decade, significant contributions to the field have been made by several international collaborations such as, the HEGRA collaboration (Germany and Armenia) and the CANGAROO collaboration (Japan and Australia). HEGRA operated an array of telescopes consisting of five small IACTs between 1997 and 2002, confirming many of detections made by Whipple. CANGAROO operated a single telescope in the southern hemisphere and made a number of detections. Recently CANGAROO was updated to an array of four 10-m scale telescopes which are in operation at present. Two European collaborations MAGIC (single 17m telescope) and HESS (an array of four telescopes) have also constructed next-generation instruments. A number of new discoveries have been made by these next-generation IACT observatories. The VERITAS collaboration (USA, UK, and Ireland), the successor to Whipple, has finished fabricating and testing the first of four 12-m telescopes and will complete construction of the array by the end of 2006.

Space-based instruments, such as SAS-2 and COS-B during 70s and 80s, established significant results in the energy range between 30 MeV to 30 GeV. The major breakthrough in this energy range was made by the Energetic Gamma Ray Experiment Telescope (EGRET) on board the Compton Gamma Ray Observatory (CGRO, one of NASA's great observatories, which was launched in 1991) and which discovered more than 270 discrete gamma-ray sources by the time its mission ended in 2000. A new generation of satellite detectors, including AGILE and GLAST, will become operational over the next few years. GLAST will be considerably more sensitive than EGRET and is expected to discover $\sim$ 1000 new sources. The sensitivities of GLAST, EGRET, and the ground-based instruments, VERITAS and Whipple, are shown in Figure 1.1. The energy ranges to which satellite and ground-based instruments are sensitive complement one another. GLAST and VERITAS are expected to overlap at the highest and lowest energies respectively.

1.1.1 VHE Gamma-ray Sources

The EGRET discovered 271 gamma-ray sources with energy > 100 MeV, including 170 which do not have corresponding known astrophysical counterparts [1]. The all sky map by EGRET is shown in Figure 1.2. The EGRET detections can be categorized in three groups, which are extragalactic point sources, galactic point sources, and diffuse emission from the Galactic plane. Approximately 90% of the total gamma-ray luminosity detected by EGRET is from the diffuse emission from the Galactic plane. This flux is believed to be generated by hadronic galactic CRs

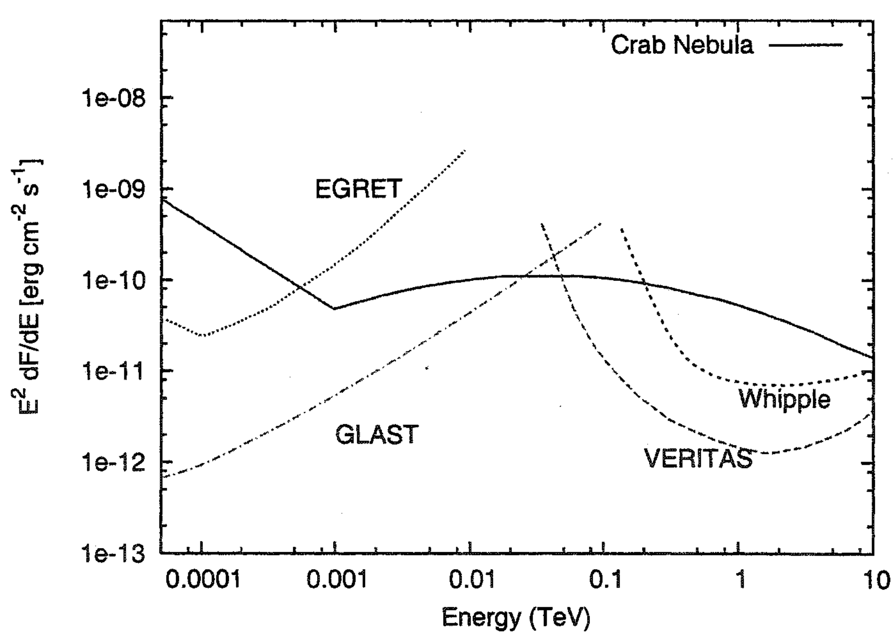

Figure 1.1. Sensitivities of some gamma-ray detectors. Crab Nebula flux is shown as comparison (section 1.1.2). EGRET and GLAST sensitivities are to achieve 5 σ with 1-year exposure. Whipple and VERITAS are to achieve 5 σ with 50-hour exposure (four energy bins per decade of energy are assumed).

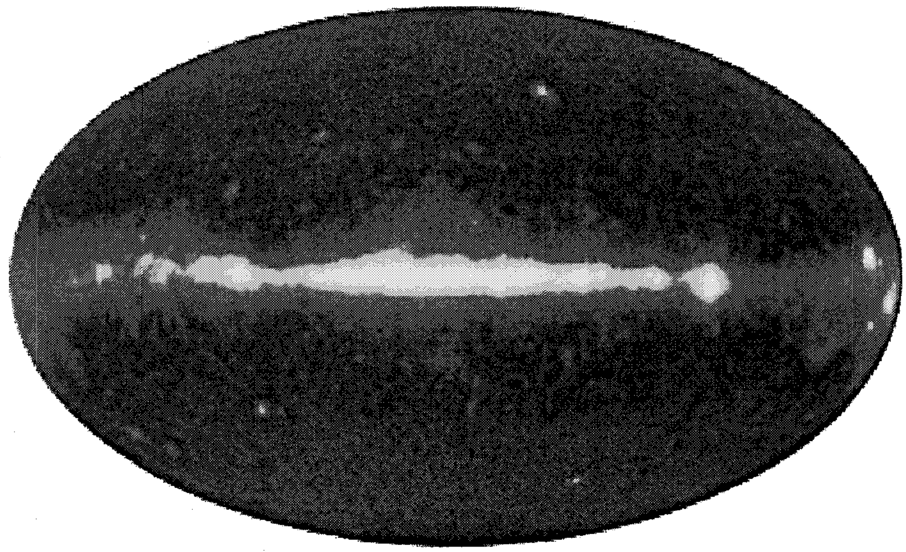

Figure 1.2. All sky map of gamma-ray emission with energies above 100 MeV detected by EGRET aboard the Compton Gamma Ray Observatory (CGRO). The bulk of the radiation results from CR interactions in the Galactic plane.

as a result of this interaction with the gas in the plane.

There are only a little more than a handful of TeV gamma-ray sources discovered thus far, in contrast to ones in the MeV energy range (see Figure 1.3 [2]).

The first discovery of an VHE (sub TeV - TeV) "extragalactic" source was Markarian (Mrk) 421 [3], a blazar belonging to subclass of active galactic nuclei (AGN), which was detected by EGRET prior to Whipple, at a lower energy range. It is located at a distance $z = 0.03$, corresponding to $\sim$ 120 Mpc ($H_0 = 75$ km/s/Mpc). AGN are believed to have supermassive black holes in their cores, which are responsible for creating relativistic jets of particles sustained by accretion. The mechanism responsible for the strong beamed gamma-ray emission from AGN, is not yet completely understood. Other known TeV extragalactic sources, such as Mrk 501, H1426, and 1ES1959, also belong to this class.

VHE observations of local galactic supernova remnants (SNRs) provide the possibility of testing VHE CR acceleration scenarios. SNR RX J1713.7-3946 was observed by the CANGAROO [4] and HESS collaborations [5] and significant emission has been found (discussed in section 1.1.3). Cassiopeia A (Cas A) is

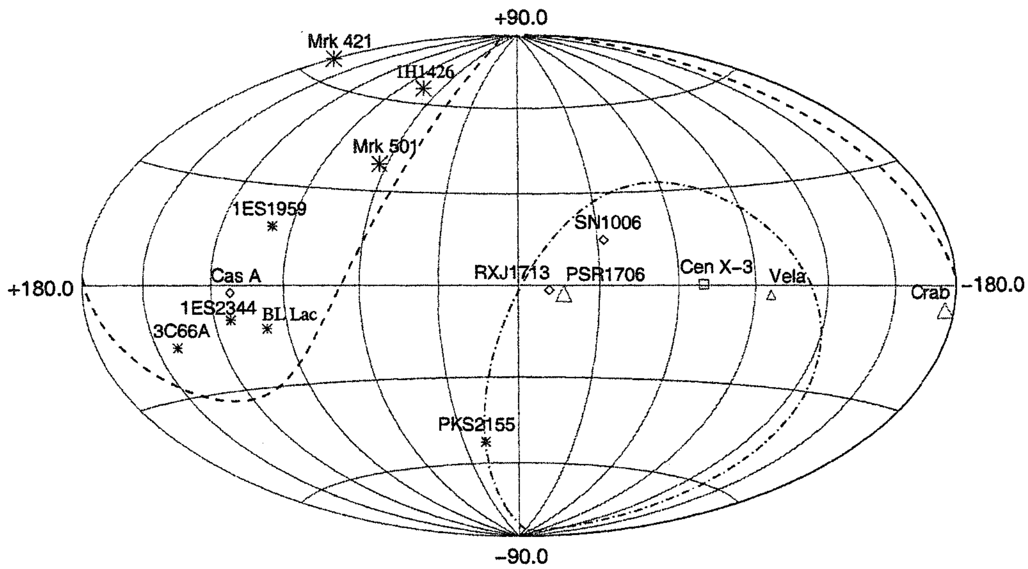

Figure 1.3. Very high energy gamma-ray all sky map (figure from Weekes 2003 [2], reproduced by permission of T.C. Weekes).

another SNR from which TeV gamma-ray emission was detected, and the observed spectrum by HEGRA is consistent with a power law with a differential index -2.5$\pm$0.4$_{stat}\pm$0.1$_{syst}$ [6].

Searches for TeV emission from a small sample of nearby starburst galaxies (SBGs) have been conducted in the northern and southern hemispheres. NGC253, a southern galaxy, was claimed as a strong TeV gamma-ray emitter by the CANGAROO collaboration [7]. This result, however, has not been confirmed by other instruments.

Gamma-ray emission from the region of the Galactic center, within a radius of $\sim 15'$ of the central black hole (Sagittarius A*), has been detected at TeV energies by CANGAROO, Whipple, and HESS [8] [9] [10].

The VHE gamma-ray counterpart of the diffuse emission from the Galactic plane had not been observed until recently. A detection of the Galactic diffuse emission is reported by the MILAGRO collaboration [11]. The integrated flux above 1 TeV was found to be $(5.1 \pm 1.0 \pm 1.7) \times 10^{-10}$ cm^{-2}s^{-1}sr^{-1} in this publication.

The first TeV source detected [12], the Crab Nebula, is discussed in the following section. A more detailed account of the VHE gamma-ray sources can be found elsewhere, e.g., [2].

1.1.2 The Crab Nebula

The Crab Nebula is a SNR with a radio pulsar, PSR 0531, near its center. The explosion of the progenitor star was noted on July 4, A.D. 1054, by Chinese astronomers, and also possibly by ancient Anasazi Indians. It is one of the few historically observed Super Novae (SNe) in the Milky Way Galaxy. The central pulsar rotates with frequency of approximately 30 Hz, creating a strong "pulsar wind" of electron-positron pairs. These electrons and positrons are accelerated to multi-TeV energy and they radiate synchrotron photons in the strong local magnetic field. A fraction of these photons interact with the population of VHE electrons and positrons, which are created there, and thereby upscattered to gamma-ray energies through the inverse Compton process. No evidence of pulsed VHE gamma-ray emission has been observed. The gamma-ray flux and energy spectrum derived by the Whipple collaboration are [13]

$$\frac{dF}{dE} = (3.25 \pm 0.14 \pm 0.6) \times 10^{-7}\left(\frac{E}{1TeV}\right)^{-2.44 \pm 0.06 \pm 0.04 - 0.151 log_{10} E} m^{-2}s^{-1}TeV^{-1}. \tag{1.1}$$

This spectrum is determined in the energy range 0.5 - 8 TeV. At 1 TeV, the differential flux scaled with E^2 is

$$E^2\frac{dF}{dE} \simeq 5.2 \times 10^{-11}\frac{erg}{cm^2 s}.$$

Because the Crab Nebula is a bright steady gamma-ray source, this flux value is frequently used to calibrate IACTs in the northern hemisphere and as a unit of measurement of VHE gamma-ray emission. As such the Crab Nebula is often thought of as the "standard candle" in VHE gamma-ray astronomy. The spectrum at lower energies was measured by CGRO [14]. The high energy nonpulsed X-ray component [15] shows a simple power low spectrum (see Figure 1.1). The detection of VHE gamma rays from the Crab Nebula provided evidence for the inverse Compton model and gave a direct measure of the local magnetic field strength [12].

1.1.3 CR Origin Problem

Since CRs were discovered in 1912 by Victor Hess, the source and mechanism responsible for their acceleration have been one of the mysteries of high energy physics. On the basis of the CR energy density in the galaxy, supernova explosions and their remnants (SNRs) have been suggested as the sites of CR acceleration in the energy range below 10^{15} eV. Almost 90% of the VHE CRs are relativistic protons. Although there is no direct proof, it is thought that CRs can be accelerated up to these energies through the Fermi mechanism in the strong shocks produced in SNRs. While propagating through the galaxy, CRs are deflected by the Galactic magnetic field and no longer retain directional information about the site of their origin. When CRs interact with ambient protons at the site of their acceleration, neutral pions are created, which immediately decay into gamma rays. For an isotropic CR spectrum, the pion decay signature has a peak at $\sim$ 70 MeV, which is equivalent to half the pion rest mass. A new generation of satellite instruments, such as GLAST, is expected to see the 70 MeV peak, if it exists. Photons at the high energy tail of the spectrum can be observed by current ground-based detectors.

Detection of gamma rays from individual local SNRs could provide direct evidences of CR acceleration. Many SNRs were observed by ground-based detectors, e.g., [16] (see Table 1.1 [17]). No clear evidence of proton CR acceleration has been found. Some indications of the existence of nonthermal electrons in SNRs have been found through hard synchrotron X-ray spectra (e.g., from supernova SN1006 [18] [19], RXJ1713.7-3946 [20], Cas A [11]). Recently, the CANGAROO and HESS collaboration detected VHE gamma-ray emission from SNR RX J1713.7-3946 [4]

Table 1.1. Observed shell-type SNR (table from S. Fegan astro-ph/0102324 [17] by permission).

Object Name	Exposure time (hours)	Flux/Upper Limit x $10^{-11} cm^{-2} s^{-1}$
CANGAROO		
RXJ 1713.7-3946	66	0.53 (≥1.8 TeV)
SN1006	34	0.46 (≥1.7 TeV)
W28	58	<0.88 (> 5 TeV[a])
HEGRA		
Cas A	232	0.058 (> 1 TeV) [b]
γ-Cygni	47	<1.1 (>500GeV)[c]
Durham		
SN1006	41	<1.7 (>300GeV)
Whipple		
Monoceros	13.1	<4.8 (>500GeV)
Cas A	6.9	<0.66 (>500GeV)
W44	6	<3.0 (>300GeV)
W51	7.8	<3.6 (>300GeV)
γ-Cygni	9.3	<2.2 (>300GeV)
W63	2.3	<6.4 (>300GeV)
Tycho	14.5	<0.8 (>300GeV)
CAT		
CasA	24.4	<0.74 (>400GeV)

[a]A different definition of Energy Threshold is used
[b]Evidence for emission at the 4.9σ level (Pühlhofer et al. 2001)
[c]Limits converted from Crab units using flux of Hillas et al. 1998

[5]. The mechanism was claimed to be neutral pion decay [21]; however, no common unambiguous explanation has been established. Although the search for evidence of proton CR acceleration by direct observations of local SNRs may be successful in the future, other approaches to the problem also exist.

1.1.4 CR-Induced Gamma Ray from Galaxies

Two discoveries of extended gamma-ray sources by EGRET stimulated the search for CR-induced gamma rays from galaxies. The first is the discovery of the diffuse gamma-ray emission from the Galactic plane of the Milky Way. Initially observed by satellite telescopes SAS-2 [22] and COS-B [23], EGRET measured emission with unprecedented detail [24], [25]. Second, is the detection of the diffuse gamma-ray emission from our neighboring galaxy, the Large Magellanic Cloud (LMC), with integrated photon flux above 100 MeV of $1.9 \pm 0.4 \times 10^{-7}$ photons cm^{-2} s^{-1} [26]. These detections show that CR interactions produce secondary gamma rays which can be observable with space telescopes. If the spectrum is extended into the TeV region, some fraction of these sources can be detected from the ground.

Starburst Galaxies (SBGs) have been suggested as potential gamma-ray emitters and, hence, are potential laboratories for testing the SNR proton acceleration scenario. SBGs are known to have intensive star formation regions, in which SN rates are expected to be higher than the Milky Way SN rate by a fraction of 10 to 100. In SBGs, star formation regions are often associated with dense gas clouds. If the density of ambient protons is high, the rate of CR loss is governed by the interaction between CR protons and ambient protons, rather than diffusive or convective processes.

VHE observations of local SBGs have been conducted by several IACT observatories recently. Observations with the Whipple 10-m telescope are reported in this dissertation. TeV gamma-ray emission from a SBG, NGC253, was reported by the CANGAROO collaboration [7]. In this southern hemisphere nearby SBG, some of the star formation regions are found to have ISM density $\geq 10^5$ protons/cm^3 (10^5 times larger than in the Milky Way). Luminous Infrared galaxies (LIGs) and Ultra Luminous Infrared Galaxies (ULIRGs), two subclasses of SBGs, have been also proposed as potential TeV sources [27]. They are located farther ($\sim$ 100 Mpc) than typical local SBGs ($\sim$ 10 Mpc), yet their high Star Formation Rate (SFR), 100 to 1000 times that of the Milky Way, might be sufficient to compensate for decrease of the flux by the large distance factor.

1.1.5 Gamma Rays from Extragalactic Sources

The largest scale gravitationally-bound stellar systems, galaxy clusters, are plausible producers of CR-induced gamma rays. Discussion and modeling of gamma-ray emissivity due to CR acceleration and interaction in galaxy clusters can be found in, e.g., [28]. In the typical scenario, each member galaxy would have been through a starburst phase early in the history of the cluster. Some fraction of high energy

CRs produced in the multitude of SNRs eventually escape from the host galaxy without interaction and enter the intergalactic space of the cluster. These CRs interact with the intergalactic shocks and might be accelerated further. Galaxy clusters are known to host large spatial scale shocks, up to 10^6 times larger than the typical SNR shocks, resulting from interactions of galactic winds. In a generic galaxy cluster (scale 1 Mpc to 10 Mpc), the typical time scale for CRs to escape from the cluster by diffusion or convection is longer than the Hubble time. Thus, the CRs are confined to the cluster and are likely to reflect the accumulated history of past stellar evolution activity. It is widely believed that in the intergalactic space of clusters, a large amount of VHE CRs accumulate and may not even reach a steady state. Although, the density of the intergalactic medium is low ($\sim 10^{-2}$ proton/cm^3) compared to the Galactic environment, it may be sufficient for the production of a gamma-ray luminosity that can be observable by ground-based detectors. The diffuse nonthermal X-ray radiation found in some galaxy clusters, e.g., [29], provides evidence for the existence of high energy CR electrons involved in the cluster scale acceleration process.

1.2 Galaxies as Extragalactic Background Light Probe

Extragalactic VHE gamma rays enable us to understand the early galaxy and star formation via their interaction with cosmological UV, visible and infrared (IR) background photons (discussions and review can be found, e.g., [30] [31] [32]).These photons, with energy of $\sim 10^{-2}$ eV to $\sim 10^2$ eV shown in Figure 1.4 [33] as a circled region next to the dominant peak due to the Cosmic Microwave Background (CMB), are frequently referred as Extragalactic Background Light (EBL). The EBL spectrum contains information about star formation, accretion processes around black holes, and interactions of the stellar light with dust out to the horizon of the Universe. Direct measurement of the EBL is difficult due to the strong foreground from the zodiacal light and the Galactic star light scattered by the interstellar gas. However, if a calibrated beam of VHE photons were known to exist from a extragalactic source, the density of the EBL could be measured by

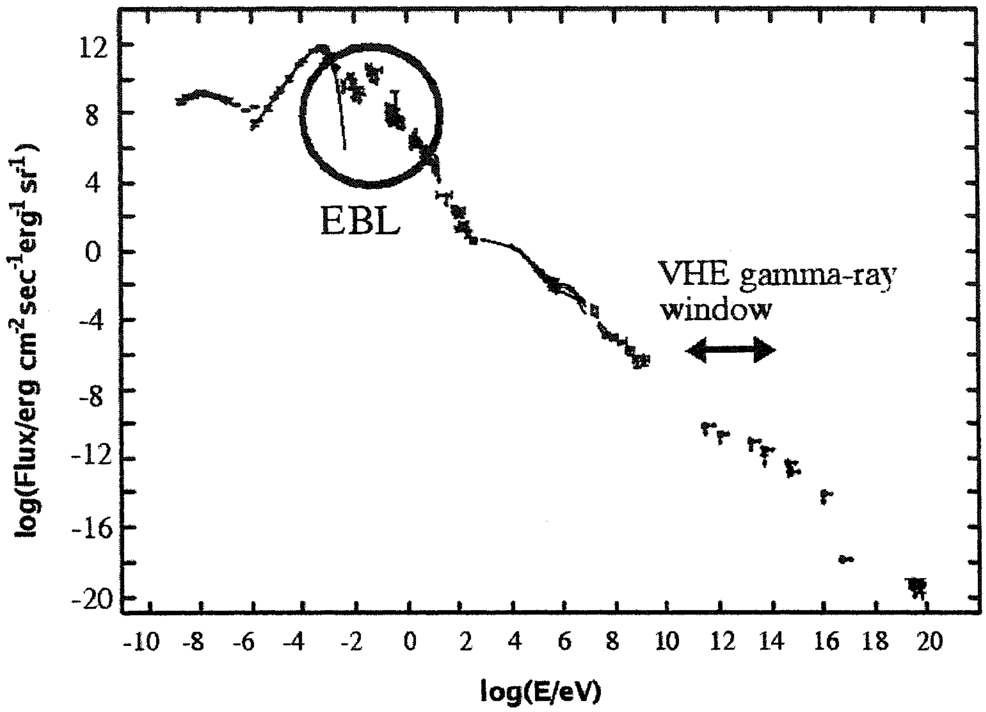

Figure 1.4. Grand Unified Photon Spectrum (GUPS), adopted from Ressell and Turner 1990 [33] by permission of the AAS. Circled part corresponds to EBL. Magnified picture of the region is shown in Figure 1.6.

studying absorption of the VHE photons due to pair production as they travel over cosmological distances (Figure 1.5),

$$\gamma_{source} + \gamma_{EBL} \longrightarrow e^{-} + e^{+}.$$

The interaction length of photon with EBL is $\sim$ 100 Mpc at a gamma-ray energy of $\sim$ 1 TeV. Therefore, the observable horizon for sources of 1 TeV gamma rays is approximately a few 100 Mpc (z = $\sim$ 0.1). Recently, observations of nearby AGN [3] [34] have been used to provide constraints of the EBL, e.g., [31] (see Figure 1.6 [35]). AGN fluxes of TeV photons are highly variable [36], and the mechanism for gamma-ray production from AGN jets is poorly understood. Because of variability, they can not be said to provide a "calibrated" source of VHE gamma rays. Therefore, the effects of photon attenuation due to EBL can not be separated from the unknown intrinsic AGN spectrum. On the other hand,

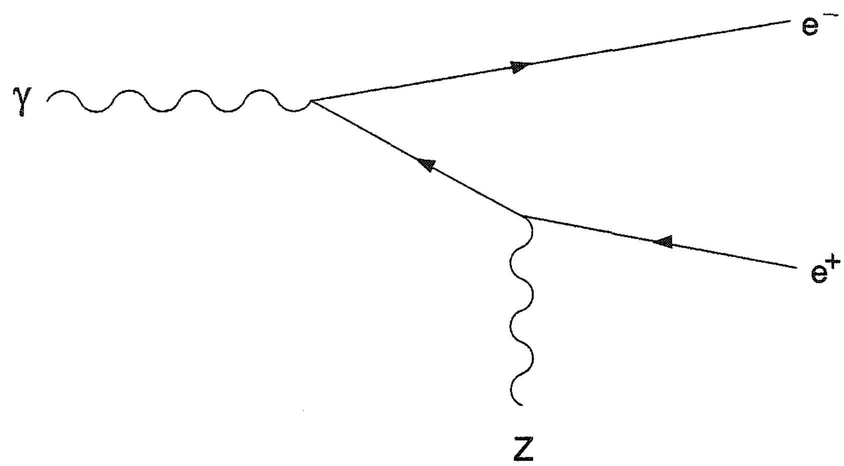

Figure 1.5. One of the two Feynman diagrams of the pair production by a photon with the electric field of a nucleus.

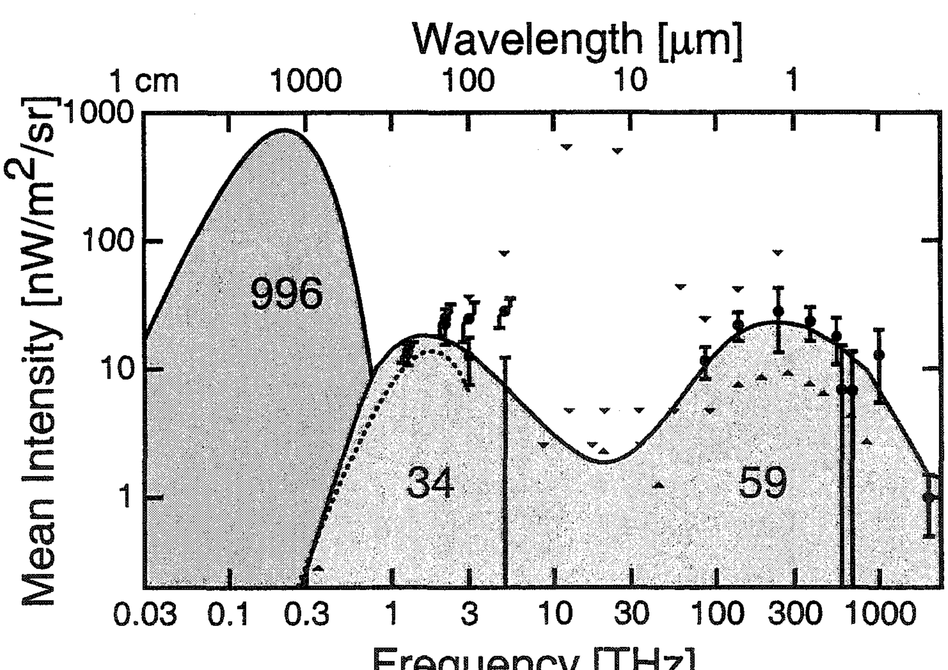

Figure 1.6. Extragalactic background light spectrum (figure from Wright 2004 [35], reproduced by permission of ELSEVIER Ltd). The upperlimit points in the region between two peaks ($\sim$ 3 THz to $\sim$ 30 THz) are set by the Whipple observation of selected AGN (e.g., [32]).

the flux of VHE gamma rays from SBGs or galaxy clusters is expected to be steady and has better understood spectral properties. Therefore, if a significant sample of galaxies or galaxy clusters is observed in the sub-TeV to TeV range, it may provide a stable, calibrated beam from which the effects of the EBL could be deconvolved.

For both AGN and galaxies or galaxy clusters, the discovery and detailed study of the photon energy spectrum from a number of sources are essential to establish the EBL measure. The new generation of IACTs should be sensitive enough to detect these sources. However, the typical field of view (FOV) of IACTs is $\sim 5°$, and they are limited to $\sim$ 800 hours/yr of observation time, too small to effectively survey the full sky. Therefore, complementary information from satellite sky survey telescopes, such as GLAST, is key to the success of such research programs.

1.3 Detection Methods

Gamma-ray detection from the ground is based on reconstruction of the energy and direction of the incident particles by studying the secondary phenomena occurring in the atmosphere. When particles with energy greater than $\sim$ 10 GeV enter the atmosphere, cascades of secondary particles, Extensive Air Showers (EAS), are induced. Since many of the secondaries are charged and relativistic, they emit Čerenkov radiation as they move through the atmosphere, resulting in the production of photons in the blue to UV parts of the spectrum. For CR and gamma-ray primaries with energy larger than $\sim$ 10 TeV, some of the charged secondary particles reach ground level. IACTs consist of large optical telescopes designed to capture the short flash of Čerenkov radiation as a pulse with duration of approximately 5 ns. On the other hand, ground-based particle detectors such as Tibet Air Shower Array [37], MILAGRO [38], and Pierre Auger [39] detect the remaining charged secondary particles from the EAS that reach ground-level. This dissertation discusses only IACT observations.

1.3.1 Čerenkov Radiation

When a charged particle travels through a dielectric medium with velocity faster than the phase velocity of light in the medium, the particle radiates photons as a consequence of resonant relaxation of electric dipole moment of molecules in the medium [40]. Called Čerenkov Radiation, this process was first observed by Čerenkov in 1934 [41] and was studied theoretically by Frank and Tamm in 1937 [42]. Čerenkov radiation is highly beamed cylindrical wave. The angle which the wave vector makes with the particle trajectory is called the Čerenkov angle . The shape of the radiation pattern is cone-like. If a charged particle is traveling through the atmosphere with velocity βc $(0 < \beta < 1)$, when βc is larger than the phase velocity of light in the medium, c/n, the particle emits photons (see Figure 1.7). From the geometry, it is clear that,

$$\cos\theta_c = \frac{1}{\beta n} \tag{1.2}$$

where θ_c is the Čerenkov angle and n is the index of refraction of air. The maximum value of θ_c happens when $\beta = 1$; therefore,

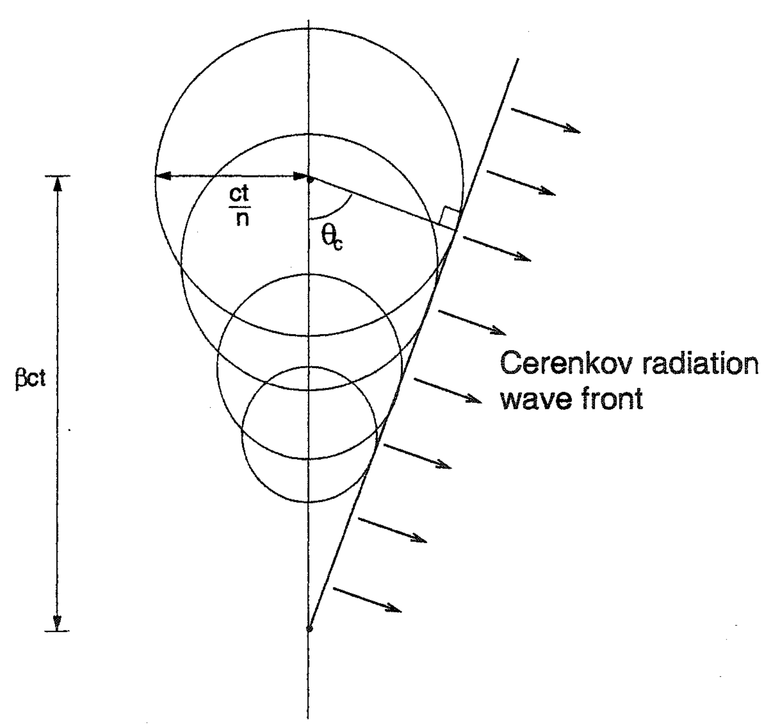

Figure 1.7. Schematic diagram of Čerenkov radiation

$$\cos\theta_{max} = \frac{1}{n}. \tag{1.3}$$

The minimum value of θ_c is 0, which occurs when the velocity of the particle is barely equal to phase velocity of light. Therefore,

$$\beta_{min} = \frac{1}{n}. \tag{1.4}$$

From this condition, the Čerenkov Radiation threshold energy of the particle can be obtained:

$$E_{min} = \gamma m_0 c^2 = \frac{m_0 c^2}{\sqrt{1-\beta_{min}^2}}. \tag{1.5}$$

The range of β which allows Čerenkov radiation to be emitted is $1/n < \beta < 1$.

1.3.2 Extensive Air Shower

High energy particles which initiate EAS are comprised mostly of isotropic CR protons, with a small fraction of ionized nuclei, CR electrons, and gamma rays. Successful discrimination between hadronic and gamma-ray events is crucial to the detection of gamma rays with IACT. Proper understanding of the physics of EAS and differences that result from CR initiated and gamma-ray initiated shower development is vital. Detailed discussion of the EAS processes is presented in many publications, e.g., [43] [44] [45] [46]. In this section, only some key elements, which emphasize the difference between developments of gamma-ray-induced and CR-induced showers, are discussed.

When gamma rays interact in the atmosphere, electron-positron pairs are produced due to the electromagnetic interaction between photon and electric fields of air nuclei (see Figure 1.8 [45]). The radiation length for the pair production in the air is 37.1 g/cm^2 [2], almost a constant for VHE photons of interest. The interaction

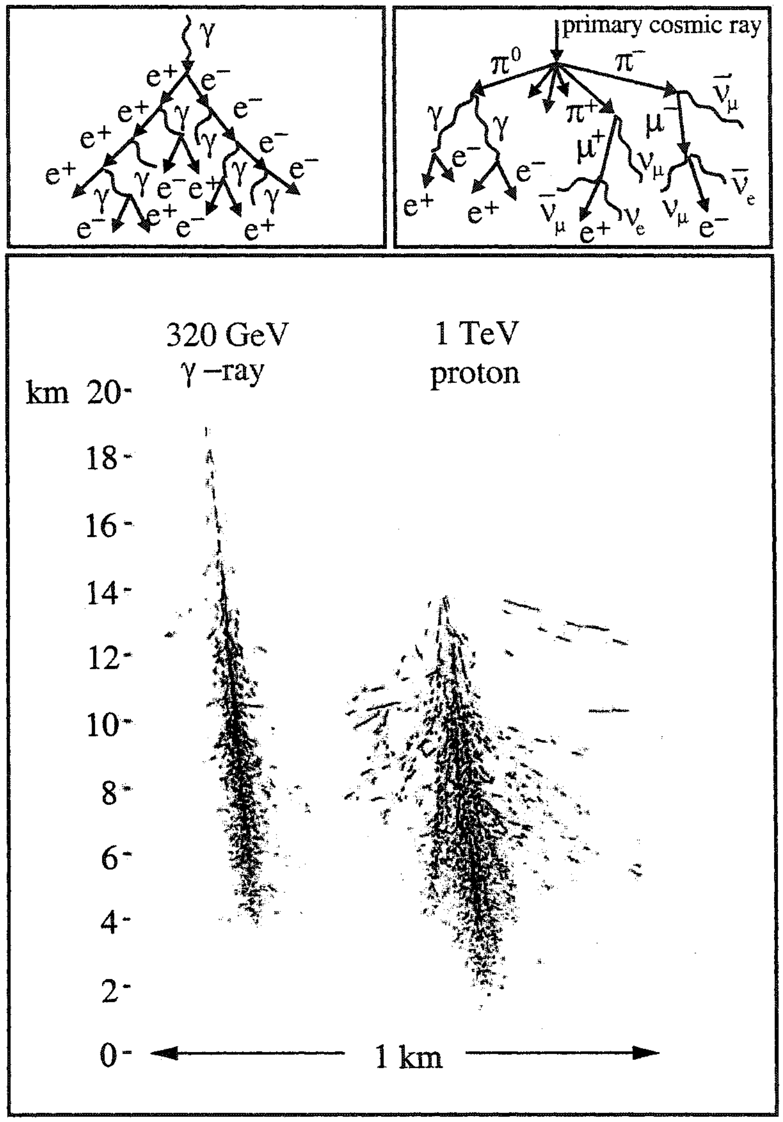

Figure 1.8. Simulated gamma-ray- and proton-induced showers (figure from Weekes 2003 [2], reproduced by permission of T.C. Weekes).

length is sufficiently short to have the reaction occur in the region very close to the top of the atmosphere. The electrons and positrons produced are very relativistic and subsequently undergo bremsstrahlung with interaction length 31.1 g/cm^2 [44], similar to that of pair production. The photons emitted through bremsstrahlung have sufficient energy to induce farther pair production. This sequence continues until the distributed energy among the many secondary particles reaches the critical energy 84.2 MeV, which is equivalent to the ionization loss per radiation length. Beyond this energy, the cascade dies rapidly. Lateral spread of the gamma-ray-induced shower is caused primarily by Coulomb scattering. The pair production and bremsstrahlung opening angles are small. Hence, gamma-ray-induced showers are strongly beamed along the trajectory of incident gamma ray.

Although gamma-ray-induced showers are largely electromagnetic in nature, the development of proton-induced showers is governed by strong force interactions. (See the top right box of Figure 1.8 for a cartoon showing the elements of shower development.) When VHE CR protons and nuclei enter the atmosphere, they induce nuclear disintegration into pions and a smaller fraction of other hadrons (such as charged K mesons). The interaction length for proton is $\sim$ 65 g/cm^2 (calculated from interaction cross section given in Gaisser [44]). Thus, proton showers develop later than those from gamma rays. The proton interaction length increases with $E^{0.06}$ [44] (E is proton energy in TeV). Thus the more energy the protons have, the later the showers develop. Neutral pions created in the shower decay into two gamma rays without interacting with other particles due to their short mean life time. Dominant decay chains are

$$\begin{aligned}
\pi^0 &\rightarrow 2\gamma & (\tau = 8.4 \times 10^{-17} s) \\
\pi^\pm &\rightarrow \mu^\pm + \nu_\mu & (\tau = 2.6 \times 10^{-8} s) \\
\mu^\pm &\rightarrow e^\pm + \nu_e + \nu_\mu & (\tau = 2.2 \times 10^{-6} s)
\end{aligned}$$

Neutrinos and antineutrinos are not distinguished in these formulae. The mean life times are obtained from the Particle Data Group database (http://pdg.lbl.gov/). Branching ratios to neutral and charged pions in the regime of primary hadron energy $\gg$ 1 GeV are roughly equal to 1/3 for each. Gamma rays from the neutral pion decay induce an electromagnetic cascade identical to the gamma-ray shower. Charged pions decay into muons or they undergo further hadronic interactions due to their relatively large lifetime. Except for very low energy muons, they reach ground level without interaction. These muons may be used for the absolute calibration of the Whipple telescope camera (see section 5.2). The lateral spread

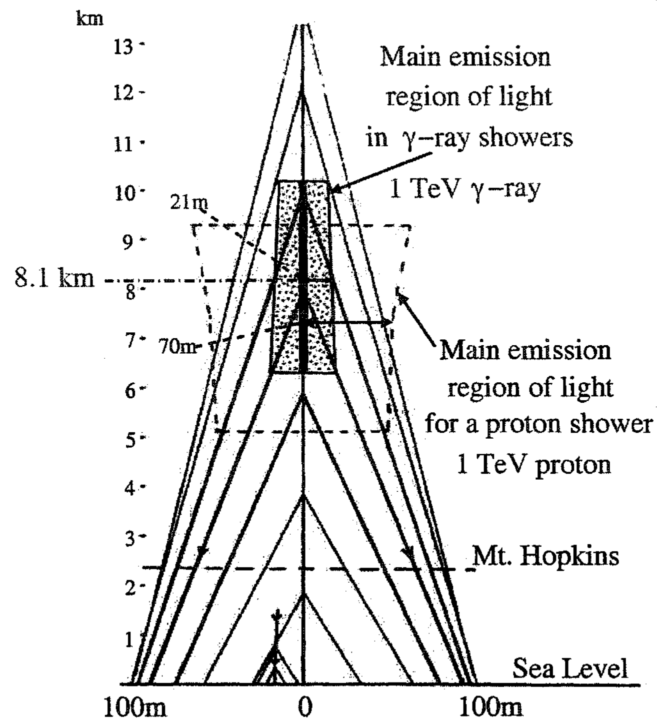

Figure 1.9. Geometry of Čerenkov radiation from EASs (figure from Weekes 2003 [2], reproduced by permission of T.C. Weekes). The shaded box shows the main emission region from gamma-ray-induced shower; half of the light comes from this region and 25% from above and also 25% below the bottom. Shower maximum and the median altitude are about 8 km above sea level, for a primary of $\sim$ 1 TeV.

of the CR-induced showers is larger than the gamma-ray-induced showers due to larger transverse momentum transfer in strong interactions rather than in the pair production and bremsstrahlung processes. The main process responsible for the lateral spread of the electromagnetic cascade is Coulomb scattering, but this process is inefficient for energies above the threshold for the emission of Čerenkov light by the particles. As shown in Figure 1.9 [45]), the geometry of the Čerenkov radiation regions for primary gamma-ray and CR-induced shower is different. The main emission region for gamma-ray-induced EAS is shown in shaded box. The median altitude is about 8 km for a vertical cascade of $\sim$ 1 TeV energy. The dashed-line box corresponds to the region from proton showers of the same energy, which is wider and lower than the gamma-ray-induced region.

It is important to note that the use of the difference of shower development from gamma rays and hadronic CRs is an essential part of the data analysis and statistical detection of gamma rays by IACT. This difference is passed on to the measured parameters of the high resolution camera images of Čerenkov radiation of EAS, so that the discrimination of hadron-induced events from gamma-ray events can be done by investigation of distributions in the image parameter space (section 5.3.5). In general, images from hadronic CR-induced showers are more spread out and contain more structure than the gamma-ray-induced images.

1.3.3 The Whipple 10-m Telescope

The Whipple 10-m IACT was built in 1968 (see Figure 1.10) at Mt. Hopkins 40 miles south of Tucson, Arizona. The altitude of the telescope is about 2.3 km above sea level. The optical reflector is of the Davies-Cotton design and comprises an alt-azimuth-mounted 10-m spherical support structure holding 248 hexagonal shape mirrors with spherical surfaces. The 10-m dish has a curvature radius $R = 7.3$ m, which is the same as the focal length of the mirror facets. Each mirror facet is aligned to a point on the main optical axis, at 2R distance from the center of the main dish. A beam of light parallel to the optical axis shone on the main reflector is focused on the camera plane at distance R from the center of the dish (Figure 1.11). The camera consists of 379 half inch (13 mm) Photo Multiplier Tubes (PMTs) with "Winston cone-like" light guides to increase the effective size of the photo cathode. PMTs with larger (28 mm) diameter were installed surrounding the inner 379 PMTs until the 2002 - 2003 season; however they are not used for the analysis in this dissertation (see Figure 1.12). The Whipple camera with inner PMTs has a field of view (FOV) of $\sim 2.2°$. Despite having ~ 75 m^2 of mirror area, the gamma-ray collecting area of the telescope is $\sim 10^5$ m^2. This large gamma-ray collecting area is determined by the size of Čerenkov light pool (circle of ~ 130 m radius), not the size of the main reflector (10-m aperture), and is the key advantage of IACT compared to satellite telescopes. The typical collecting area of satellite detectors are equivalent to the size of their instrument apertures (~ 1000 cm^2 - 1

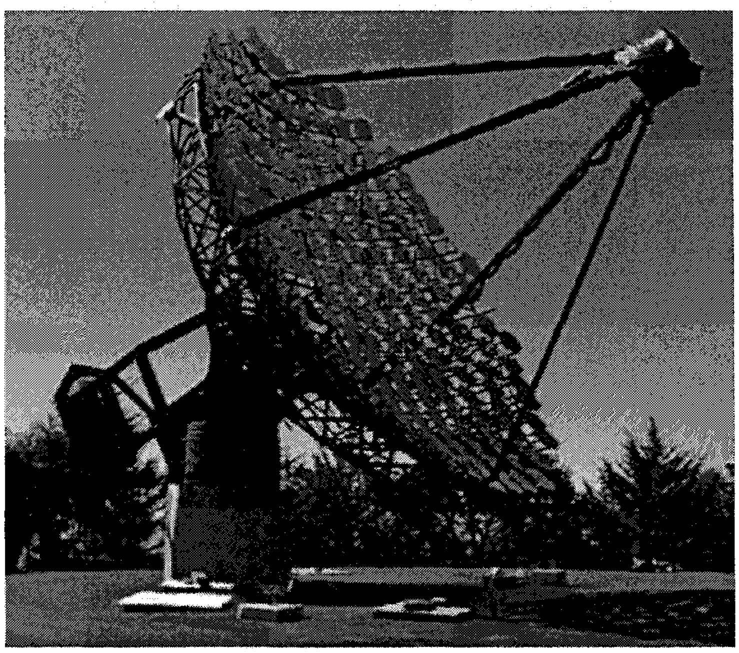

Figure 1.10. The Whipple 10-m Gamma-ray Telescope at the Fred Lawrence Whipple Observatory, Mt. Hopkins, Arizona.

m^2).

1.3.4 Data Acquisition System

The duration of a Čerenkov light pulse is approximately 5 ns. However, the pulse duration becomes broadened by the optical system and electronics to $\sim 15-20$ ns, with a rise time ~ 5 ns. Thus, fast trigger electronics system similar to those used in particle physics experiments is used to trigger the telescope. A schematic of the Whipple electronics is shown in Figure 1.13. The signals generated by the PMTs are AC coupled and amplified. Then the signals are split into two channels. One is sent to the trigger system, and another one is delayed by ~ 120 ns by passing through long delay cables. The first component of the trigger system, to which signals from the inner 331 channels are sent, is a set of Constant Fraction Discriminators (CFDs), one for each channel. The CFD threshold voltage determines the rate of events triggering that channel. The threshold is set as low as possible, to pass small events. However, if it is set too low, random fluctuations in the night sky

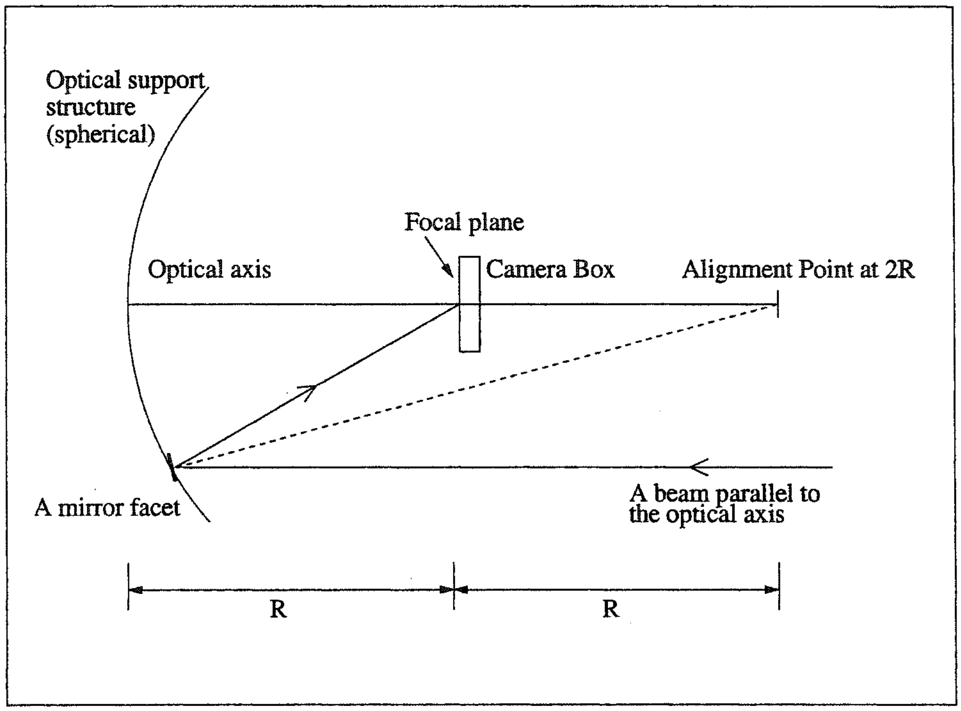

Figure 1.11. Ray tracing diagram of the Whipple telescope (Davies-Cotton design).

background (NSB) dominate the triggering rate of the system causing it to exceed the capability of the data acquisition system (DAQ). The ideal threshold setting produces recorded events at a rate of approximately 30 to 35 Hz. Those channels which exceed the CFD threshold are sent to the Pattern Selection Trigger (PST), which produces the master telescope trigger for events in which a preset (2-fold, 3-fold or more) number of neighboring channels are involved. The PST trigger timing is, unfortunately, not stable; i.e., it has an intrinsic time jitter. To remove this and to contain each delayed pulse within the trigger window, the summed CFD outputs are fed into another discriminator to set the timing for the master trigger. This is necessary, since the pulse integration window opened by the trigger for the recording is only $\sim$ 20 ns. Finally, when the system is successfully triggered, the delayed signals are integrated by charge Analog to Digital Converters (ADC), and then they are read out by the DAQ computer over a computer network.

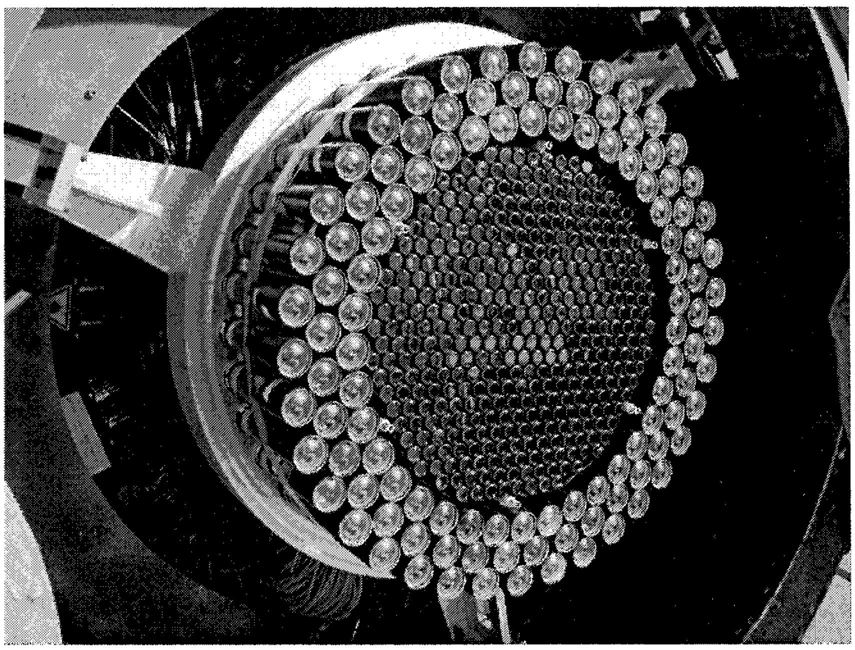

Figure 1.12. The Whipple high resolution camera. Outer tubes are removed during 2003 observation season. The camera consists of 379 half inch PMTs. The lightcone plate is not installed on the camera in this photograph.

1.4 Observations of SBGs

The ground-based observations of selected SBGs, including the nearby SBG IC342, have been conducted at the Whipple Observatory from January 2001 to March 2004. CR astrophysics, including our SBG source selection criteria, which were based partially upon photon flux estimation, are discussed in the next chapter. The observations and analysis methods (both the standard and new maximal likelihood method) are described in detail in Chapters 4 and 5; these are followed by a discussion of the results obtained. In the final chapter, the possibilities of detection with next-generation ground-based telescopes are reviewed.

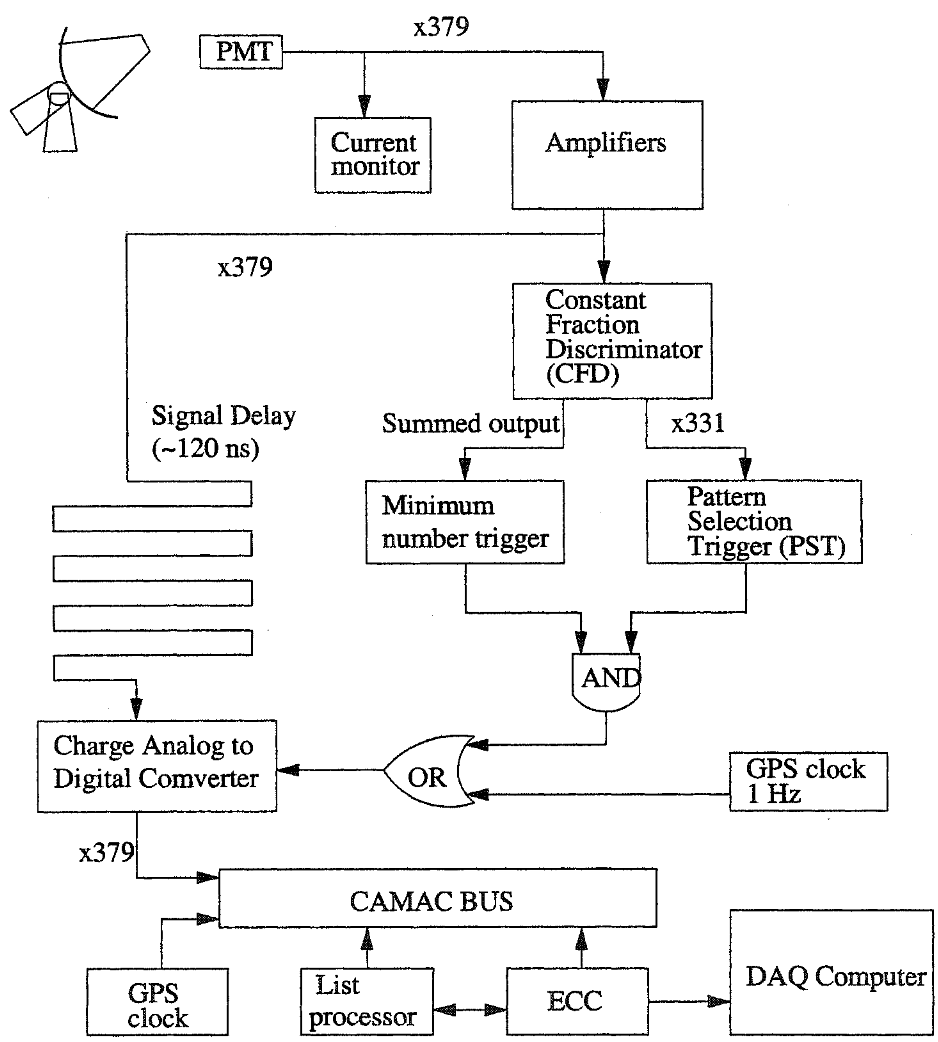

Figure 1.13. Diagram of the Whipple electronics.

CHAPTER 2

CR ASTROPHYSICS

The detection of gamma rays from the local SNR, RX J1713.7-3946, by the CANGAROO [4] and HESS collaborations [5] provided indirect evidence of high energy CR acceleration at SNR, by demonstrating the presence of at least a population of relativistic electrons. Although, Enomoto et al.[21] suggested that the origin of the gamma-ray emission is due to hadronic interactions, this is not the commonly accepted interpretation at this time. SBGs have been proposed as alternative astrophysical objects for testing the scenario of SNR as the origin of high energy CRs. These objects are known to have intense star forming regions, often associated with high density gas environments. If the regions are sufficiently old, massive O and B stars have enough time to evolve into the SN stage. A high SN rate in an environment of dense ambient gas is expected to create preferable conditions for the cumulative enhancement of gamma-ray production, possibly with a flux high enough to be detected by ground-based instruments. The proper combination of critical parameter values, such as distance, SN rate, ISM gas density, magnetic field strength, and size of the region, is necessary to maximize the flux. It is important to note that the phase of the starburst evolution is also a key element for gamma-ray production since the density of ambient ISM protons is strongly dependent on the age of the star forming region. If the phase of starburst evolution is too early, there are not enough SNe to create a high enough flux. If it is too late in the development, most ISM protons have been evacuated from the regions and the starburst ends. However this strict condition can be avoided if the star formation is ongoing and gas is continuously supplied to the regions. In this chapter, the motivations for searching for VHE gamma-ray emission from SBGs and an estimation of the photon flux based on the characteristic parameters, such as distance, ISM density, and SN rate, are developed. In the first section, the reasons why SNR may be the principal source of CR acceleration and mechanisms responsible for this acceleration are reviewed. The flux estimates are presented in the second section.

2.1 CR Acceleration at SNRs

In 1987, a type II SN was discovered in the LMC, and hence called SN1987A. An optical image taken by the Hubble telescope and a schematic picture of the SN are shown in Figure 2.1. Two distinct large outer rings can be seen with smaller central ring. One of the possible interpretations of these rings can be that the rings are created by the interactions between the bipolar jets from the SN and a surrounding bubble-like molecular shell created by the stellar wind from the progenitor star throughout its evolution. Such bubble-like structures created by stellar winds or SN explosions (often called "supershell") are frequently seen around O and B stars or star associations, even around the Sun (called the local bubble, > 300 ly in diameter). This SN provides an example of a shock propagating through the bubble, which is often described in CR acceleration scenario. A historical note for SN1987A

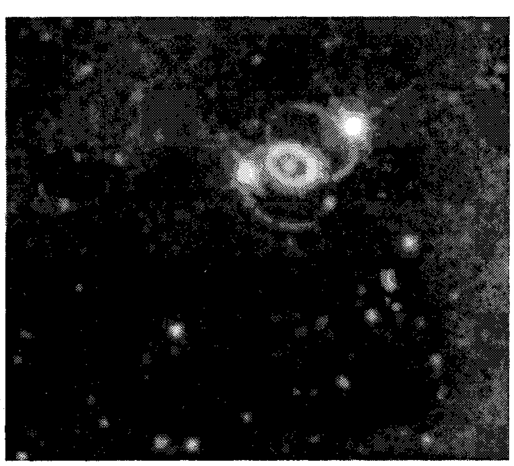

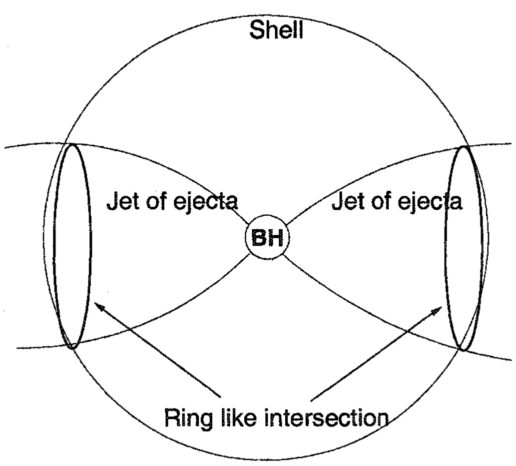

Figure 2.1. Hubble image of the supernova SN1987A. Distinct red rings are shown. Outer two rings might be created as a consequence of the interaction of the bipolar jet of ejected particles with spherical bubble-like distribution of gas surrounding the SN. The bubble was likely created by stellar wind from the progenitor star (Credit for the picture on the left: Hubble Heritage Team [AURA/STScI/NASA]).

can be found in [2].

2.1.1 Why SNRs?

In 1964, Ginzburg and Syrovatskii [47] emphasized that the Galactic SNR CR origin scenario is quite plausible in terms of maintaining the CR energy density of the Milky Way galaxy by converting SNR (Type II) ejecta mass to CRs. It is experimentally known that the local CR energy density is ~ 1 eV/cm^3. If it is assumed that this value is approximately the same everywhere in the Galactic disk, the necessary power required to maintain the CR energy density against diffusive loss (in the Milky Way, this is the dominant cause of the loss, due to low ISM density ~ 1 proton/cm^3 ~ 1 eV/cm^3) is

$$L_{CR} = \frac{V_{mw}\rho_E}{\tau_{res}} \sim 5 \times 10^{40}\frac{erg}{sec}$$

where, τ_{res} is residence time of CRs in the Galactic disk, which is estimated to be $\sim 6 \times 10^6$ years. V_{mw} is the approximate volume of the disc of the Galaxy $\sim 4 \times 10^{66}$ cm^3. Assuming that a mass of ~ 10 M$_\odot$ is ejected from a SN Type II explosion with a typical propagation velocity of $\sim 5 \times 10^8$ cm/sec at a rate of one every 30 years (typical values used in many theoretical models, e.g., [48], consistent with observations, e.g., [49]), the power available from SN explosions is

$$L_{SN} \sim 3 \times 10^{42}\frac{erg}{sec}.$$

Thus, only a few percentages of the ejecta mass energy must be transferred to CR acceleration in order to achieve the necessary power requirements. In this work, we adapt the Galactic SN rate of 1/30 yr^{-1} which agrees with estimated values in a number of publications [50] [51] [52] [53].

Shock waves are formed when the ejecta mass released from the SN explosion propagates outward as shells of plasma with velocity faster than the acoustic velocity in the plasma. These moving shocks, with inhomogeneous magnetic fields, transfer some of their momentum to charged particles in the vicinity. This process is known as the Fermi acceleration.

2.1.2 The Fermi Acceleration Mechanism

When a charged particle is injected into a moving plasma, inhomogeneities of the magnetic field behind the boundary of cloud or shock front deflect the particle and it eventually leaves the moving plasma. Due to further scattering by the diffuse external magnetic field, this particle may return to the moving plasma and cross the boundary again (see Figure 2.2 for the case with the shock front). Every time the particle encounters the boundary, it gets accelerated by the momentum transfer from the moving magnetic field due to the moving plasma. This random process of CR acceleration with moving shock front is the first-order Fermi mechanism (it is called first order, since the acceleration of the particle is proportional to the shock propagation velocity); if the particle is accelerated by the moving cloud of plasma, it is called second order Fermi mechanism. The second-order mechanism was first suggested by Enrico Fermi in 1949 [54] to explain the origin of cosmic rays.

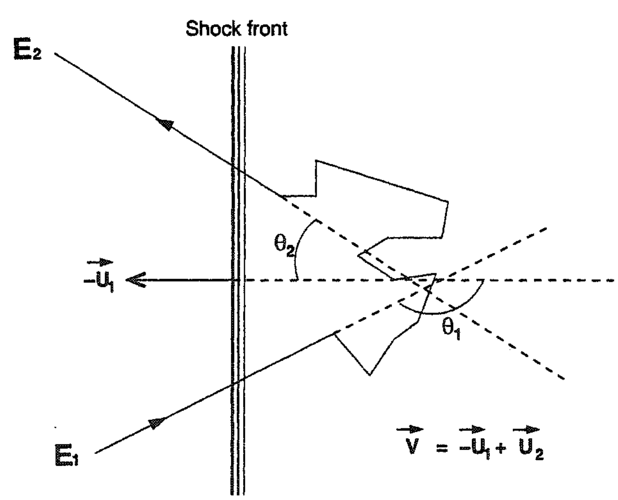

Figure 2.2. Schematic picture of a moving shock front. E_1 is the energy of injected particle, and E_2 is consequent energy of the particle. In average, $E_1 > E_2$ by the first-order Fermi acceleration.

The first order mechanism was independently proposed by e.g., [55] [56]. In this scenario, acceleration is limited by the size of the shock region, since the Larmor radius of the particle can not be larger than the size of the acceleration site. Also, the rate of re-injection limits the average energy to which particles are accelerated. Detailed study and reviews of the CR acceleration mechanism can be found in many publications, e.g., [57] [58], or more recently [59]. In the original work, Bell found that the energy spectrum of the CRs obtained in the first-order Fermi acceleration at the plane shock front is a power law with an index close to that observed for galactic CRs.

As shown in Figure 2.2, plasma particles behind the shock front, carrying the magnetic field, are moving backward relative to the front with velocity U_2. Since $|U_1| > |U_2|$, from the laboratory frame, the gas is moving to the direction of the shock propagation with velocity $V = -U_1 + U_2$.

After n encounters with the shock front, the total energy of the particle is

$$E_n = E_0(1+\xi)^n \tag{2.1}$$

where E_0 is the initial energy of the particle, ξ is given for the plane shock propagation as [44]

$$\begin{aligned} \xi &\equiv \frac{\langle E_2 - E_1 \rangle_{\theta 1, \theta 2}}{E_1} \\ &= \frac{1 + \frac{4}{3}\beta + \frac{4}{9}\beta^2}{1 - \beta^2} - 1 \\ &\sim \frac{4}{3}\beta \\ &= \frac{4}{3}\frac{U_1 - U_2}{c}. \end{aligned} \tag{2.2}$$

If the probability for the injected particle to escape the shock region is assumed to be approximately constant per injection, denoted as P_{esc}, then the probability to remain in the acceleration region after n injections is $(1 - P_{esc})^n$. The number of injections necessary to reach energy E is

$$n = ln\frac{E}{E_0}/ln(1+\xi). \tag{2.3}$$

Therefore, the number of particles accelerated to energies greater than E is propotional to

$$\begin{aligned} N(\geq E) &\propto \sum_{m=n}^{\infty}(1 - P_{esc})^m \\ &= \frac{(1-P_{esc})^n}{P_{esc}}. \end{aligned} \tag{2.4}$$

Substituting equation 2.3 into 2.4 gives

$$N(\geq E) \propto \frac{1}{P_{esc}}\left(\frac{E}{E_0}\right)^{-\gamma} \tag{2.5}$$

where

$$\begin{aligned} \gamma &= ln\left(\frac{1}{1-P_{esc}}\right)/ln(1+\xi) \\ &\simeq \frac{P_{esc}}{\xi}. \end{aligned} \tag{2.6}$$

If we denote the number density of particles undergoing acceleration by ρ_{CR}, then the rate of encounter of the particles with the shock plane is

$$\int_0^1 dcos\theta \int_0^{2\pi} \frac{c\rho_{CR}}{4\pi}cos\theta = \frac{c\rho_{CR}}{4}. \tag{2.7}$$

The rate of convection downstream away from the shock front is $\rho_{CR} \times U_2$; therefore,

$$
\begin{aligned}
P_{esc} &= \frac{\rho_{CR} U_2}{c\rho_{CR}/4} \\
&= \frac{4U_2}{c}.
\end{aligned}
\tag{2.8}
$$

Substituting equations 2.2 and 2.8 into 2.6, the integrated spectral index is

$$
\gamma = \frac{3}{U_1/U_2 - 1}.
\tag{2.9}
$$

Due to the mass flow continuity across the shock,

$$
\rho_1 U_1 = \rho_2 U_2.
$$

Using the kinetic theory of gas, we get

$$
\begin{aligned}
\frac{U_1}{U_2} &= \frac{\rho_1}{\rho_2} \\
&= \frac{(c_p/c_v + 1)M^2}{(c_p/c_v - 1)M^2 + 2},
\end{aligned}
\tag{2.10}
$$

where $M = U_1/c_1$, the Mach number of the gas in the shock region. For an mono-atomic gas the ratio of specific heat is $c_p/c_v = 5/3$; then

$$
\gamma \approx 1 + \frac{4}{M^2}
\tag{2.11}
$$

with $M \gg 1$, for a strong shock. Equation 2.11 produces a differential spectra index slightly larger than two, consistent with the measured CR spectrum near the Earth of ~ 2.7, when CR propagation losses in the Milky Way are accounted for.

The external magnetic field strength can be an enhancement factor since a strong magnetic field increases the probability that the accelerated particle reenters the shock front.

2.2 CR-Induced Gamma-ray Emissivity

VHE gamma rays provide indirect evidence of CR acceleration due to the decay of neutral pions produced as the hadronic CRs interact with the surrounding medium (life time of pion $\approx 8.3\times10^{-17}$ s. See, for example, [60]). Therefore it may be possible to utilize VHE gamma-ray astronomy to indirectly detect the sites of acceleration of CR protons. However, electrons are also accelerated by the same mechanism and can produce gamma rays through inverse Compton (IC) up-scattering of the surrounding ambient photons with wavelengths in the IR and micro wave bands. At small spatial scales, such as a site of a single SN shell, the gamma-ray flux produced by leptonic component may dominate in some astrophysical settings. However, the power loss from relativistic particles with mass Am and charge Ze through synchrotron cooling in the magnetic field is [57]

$$\left(-\frac{dE}{dt}\right)_{synchrotron} \approx 1.6\times10^{-3}\frac{erg}{sec}\left(\frac{Z}{A}\frac{m_e}{m}\right)^4 E^2B^2, \tag{2.12}$$

where E is energy of the particle and B is the magnetic field in the region. The power loss is proportional to $1/Am$ to the fourth power. Therefore, relativistic VHE electrons do not maintain their energy long enough over large scales of starburst regions or galaxies to scatter a significant number of photons. As a consequence, the electron component production of the overall gamma-ray spectrum from many SNRs is much smaller than the proton component production. This can be indirectly seen in the Galactic diffuse gamma-ray spectrum studied by Sreekumar et al. 1993 [24] and Hunter et al. 1997 [25]. A model of gamma-ray emission from the Galactic plane, where the majority of the gamma rays are believed to be produced by a hadronic interaction component, matches the observed diffuse gamma-ray spectrum well [25]. Possible enhancement of the gamma-ray emission from secondary electrons produced via *charged* pions is not included in the discussion here. These contributions for the Milky Way are believed to be small but may be significant in some cases.

2.2.1 The Milky Way and the LMC

EGRET detected diffuse gamma-ray emission (in the range of 30 MeV - 30 GeV) from only two galaxies: the Milky Way and the Large Magellanic Cloud (LMC) [24] [25] [26]. The integrated photon flux from the Galactic plane is 2.7 $\times 10^{-4}$ ph/cm^2 s ($E > 1$ GeV) and the differential spectral index is ~ 2.76 (calculated from the plot presented in [25]). These detections have stimulated interest in searching for diffuse gamma-ray emission from other galaxies. As discussed in Hunter et al. [25], the dominant component of the Galactic diffuse emission can be explained by nuclear-nuclear interactions. The observed spectrum has a knee-like feature which is predicted theoretically from the neutral pion decay envelope, with a peak half the rest mass of pion ~ 70 MeV.

The LMC is located at the distance ~ 50 kpc [61]. The reported integrated flux above 100 MeV is $1.9 \pm 0.4 \times 10^{-7}$ photons cm^{-2} s^{-1}. The photon energy spectrum using the observed integrated flux value, and assuming a differential spectral index 2.5, is also shown in the Figure 2.3. In the LMC, the SN rate is estimated to be only $\sim 4-7\%$ of the Galactic value [62], whereas the average neutral hydrogen density is ~ 2 H/cm^3 [63], slightly larger than in the Milky Way, ~ 1 H/cm^3.

The typical distance to nearby SBGs is a few Mpc. If the Milky Way was observed at a distance of 1 Mpc, the gamma-ray flux would be even smaller than the flux from LMC (Figure 2.3).

The possible gamma-ray flux from the LMC calculated and scaled flux from the Milky Way galaxy are below the sensitivities of current ground-based VHE gamma-ray instruments. However, the detection of high energy gamma rays from these galaxies by EGRET is encouraging. the Galactic SN rate is 10 - 100 times smaller and ISM density is $10^3 - 10^5$ times smaller than the typical SBG values; thus SBGs can be plausible candidates of VHE gamma-ray emitters, due to the enhancement from a higher ISM density and higher SN rate, even though they are

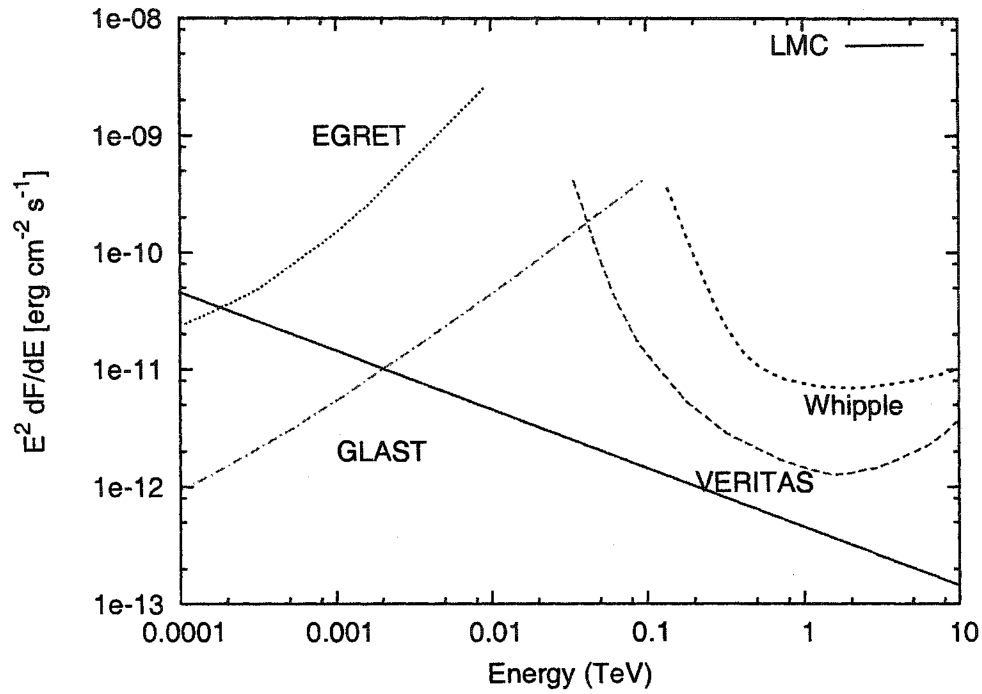

Figure 2.3. A possible spectrum of the LMC. The spectrum is calculated from the reported integrated flux ($1.9 \pm 0.4 \times 10^{-7}$ photons cm^{-2} s^{-1}) by Sreekumar et al. 1992, with the differential spectral index 2.5 assumed. The Whipple, the VERITAS and the EGRET sensitivities are plotted for comparison. The sensitivities are to achieve 5 sigma with 50-hour exposure

located further away.

2.2.2 Gamma-ray Flux Estimation

Suppose that the spectral number density of CRs at the site is known, then the rate of gamma-ray production due to hadronic interactions has the form,

$$\frac{dN_\gamma}{dt} = \frac{1}{\tau_{int}} b_\gamma \left(\frac{d\rho_{sb}}{dE} dE \right) V_{sb}.$$

The differential flux of gamma ray can then be written as

$$\frac{dF_\gamma}{dE} = \frac{1}{\tau_{int}} b_\gamma \frac{d\rho_{sb}}{dE} \frac{V_{sb}}{4\pi D^2}. \tag{2.13}$$

If this flux is rescaled with the Milky Way differential spectral number density of CRs, then

$$\frac{dF_\gamma}{dE} = \frac{1}{\tau_{int}} b_\gamma \frac{d\rho_{mw}}{dE} \frac{V_{sb}}{4\pi D^2} \left(\frac{\frac{d\rho_{sb}}{dE}}{\frac{d\rho_{mw}}{dE}} \right) \tag{2.14}$$

where

$\frac{1}{\tau_{int}}$ - p-p interaction frequency ($= n_p c\sigma$)

n_p - target proton density

σ - p-p collision cross section

c - the speed of light

b_γ - branching ratio of gamma ray from p-p collision through neutral pion decay

$\frac{d\rho_{sb}}{dE}$ - differential CR density of CR in the acceleration region

$\frac{d\rho_{mw}}{dE}$ - differential CR density of CR in the Milky Way

V_{sb} - volume of the emission region

D - distance to the emission region

A value of 0.363 is adopted for b_γ, calculated for p-p collisions with a CR spectral index 2.7, ignoring interactions between proton and He, alpha and heavier nuclei ([44], from Table 5.2 and equation 10.5). This is a pessimistic assumption; if all the other heavy nuclei are included in the process, b_γ becomes slightly larger. The last term of the equation 2.14, a scaling factor, is denoted by S.

$$S \equiv \frac{\frac{d\rho_{sb}}{dE}}{\frac{d\rho_{mw}}{dE}}. \tag{2.15}$$

The scaling factor S is proportional to the ratio of CR confinement times at the emission site and in the Milky Way. For CRs traveling through a region of gas, the CR confinement time is governed by diffusion and interaction. For example, in the Milky Way, the average density of ambient protons is ~ 1 H/cm^3. In such a dilute gas environment, accelerated CRs can easily escape by diffusion. On the other hand, in a very dense gas environment, CRs will interact with ambient protons with high probability. The CR confinement time in a region can be written as

$$\frac{1}{\tau_{res}} = \frac{1}{\tau_{esc}} + \frac{1}{\tau_{int}}. \tag{2.16}$$

Here, τ_{esc} is the time for CRs to escape diffusively or convectively from the region. Then, S can be written as

$$S = \frac{R_{sb}}{R_{mw}} \times \frac{\tau_{sb}}{\tau_{mw}} \times \frac{V_{sb}^{-1}}{V_{mw}^{-1}} \tag{2.17}$$

where, τ_{sb} and τ_{mw} are CR confinement time in the starbursting region and the Milky Way. Here R_{sb} and R_{mw} are rates of SN explosions in the whole starburst region and in the Milky Way.

In determination of the scaling factor, S, an equal average CR production efficiency per SN in the SBG and the Milky Way is assumed. This assumption is not exactly correct, since in most of SBGs, a majority of SNRs are from massive progenitor stars becoming Type II SNe, as the starburst region is often not old enough to host Type Ia SNe. Starburst regions can not be as old as the Milky Way, because if they are, the high density ambient gas would have been evacuated by the pressure from OB stars and multiple SN explosions, stopping the star formation. The typical age of starburst regions is several millions to several tens of millions of years, which is old enough to host SNe Type II, but not old enough for Type Ia. In contrast, in the Milky Way, recent SNRs are predominantly Type Ia oriented, and usually produced by much smaller progenitor star explosions. Therefore, this assumption might lead to an under estimation of the flux from SBGs.

Combining the equations 2.14 and 2.17, we get

$$\frac{dF_\gamma}{dE} = \frac{b_\gamma}{\tau_{mw}}\frac{d\rho_{mw}}{dE}V_{mw}\frac{1}{4\pi D^2}\frac{R_{sb}}{R_{mw}}\frac{\tau_{sb}}{\tau_{int}} \tag{2.18}$$

The last two factors represent the possibility of gamma-ray enhancement against the distance factor $1/(4\pi D^2)$.

2.2.3 Extreme SN Rates

Due to the high star formation rate, the SN rate is also expected to be high in starbursting regions. In typical SBGs, the star formation rate is between several and 10 times higher than the rate in the Milky Way ($\sim 1\ \mathrm{M}_\odot$). In the star formation region, which is old enough to host SNe, the SN rate is roughly proportional to SFR. On the other hand, the SFR can be estimated by the Far Infrared (FIR) luminosity emitted by the warm dust heated by embedded massive OB stars. Therefore, SBGs with high ISM density are tend to be luminous in FIR, and FIR luminosity is roughly proportional to SN rate. Luminous infrared galaxies (LIGs) and ultra luminous infrared galaxies (ULIRGs) are subdivision of SBGs, which produce an Infra Red (IR) luminosity as high as $\sim 10^{13}\ \mathrm{L}_\odot$. Such high IR luminosity is likely caused by their extremely high SN rate, which can be as high as two to three orders of magnitudes than that of normal galaxies. Unfortunately they are considerably further than the local SBGs. However, one of the closest ULIRGs, Arp220 ($\sim$75 Mpc), has been suggested as a potential TeV gamma-ray source [64] for the next-generation of IACTs, such as VERITAS. One of the SN rate estimates for Arp220 is 2 /yr [65], which is $\sim$ 100 times larger than the Milky Way value of 3.3×10^{-2} /yr or $\sim$ 20 times larger than SN rate in NGC253. Such a high SN rate, combined with large magnetic fields, which increases confinement time, might be sufficient to overcome the large distance factor and allow Arp220 to be detected with ground-based gamma-ray instruments. The estimated flux spectrum of Arp220 is shown in Figure 2.4 together with a compiled energy flux spectrum from photon flux spectrum presented in [64].

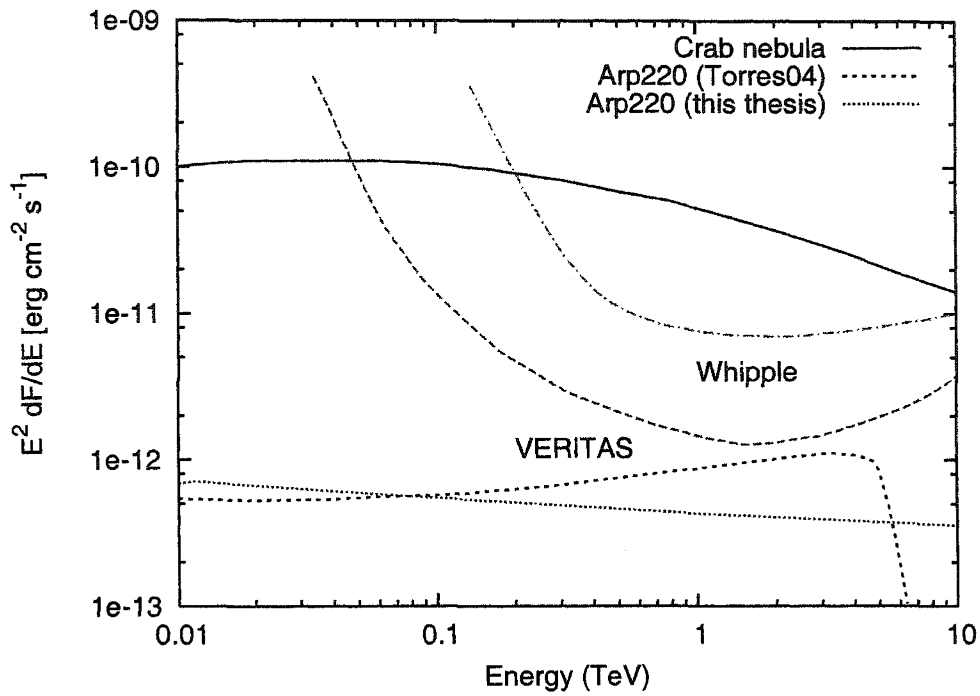

Figure 2.4. Estimated spectrum of Arp220 and predicted spectrum by Torres 2004. The predicted spectrum is compiled from Torres 2004 by permission of the AAS.

2.2.4 Interaction Dominant Regime

In SBGs, star formation regions are often associated with high density gas clouds. One of the extreme cases might be NGC253, a southern hemisphere SBG, in which the density of molecular hydrogen can reach $\sim 10^5$ proton/cm^3 (e.g., [66]). In such high density regions with sufficiently large magnetic fields, τ_{int} may become smaller than τ_{esc}, which indicates that the steady state density of CRs is governed by interactions rather than diffusion. This seems to be the case for SBGs which are plausible candidates for TeV photon emission. In this scenario, τ_{res} is almost equal to τ_{int} and the enhancement factor τ_{sb}/τ_{int} takes its maximal value 1, and the dependence on the density of target material cancels out. Equation 2.18 becomes

$$\frac{dF_\gamma}{dE} = \frac{b_r}{\tau_{mw}}\frac{d\rho_{mw}}{dE}V_{mw}\frac{R_{sb}}{R_{mw}}\frac{1}{4\pi D^2}. \tag{2.19}$$

In the Milky Way, τ_{mw} is equal to τ_{esc} due to diffusion of CRs in magnetic field [67]:

$$\begin{aligned}\tau_{mw} &\simeq \tau_{esc} \\ &= 2.39\times 10^{5}\left(\frac{E}{1TeV}\right)^{-0.6} yrs.\end{aligned} \tag{2.20}$$

Taking into account that

$$\frac{d\rho_{mw}}{dE} = \frac{dF_{CR}}{dE}\left(\frac{4\pi}{c}\right), \tag{2.21}$$

and that the Galactic disc volume is approximately 4×10^{66} cm^3 (assuming radius is $\sim$ 15 kpc, thickness $\sim$ 200 pc), we derive

$$\frac{dF_{\gamma}}{dE} = 6.99\times 10^{-7}\frac{dF_{CR}}{dE}\left(\frac{E}{1TeV}\right)^{0.6}\frac{R_{sb}}{R_{mw}}\left(\frac{1Mpc}{D}\right)^{2}(cm^{-2}s^{-1}TeV^{-1}) \tag{2.22}$$

In this equation, dF_{cr}/dE is the CR flux spectrum in the Milky Way (near the Earth), which is known to be $\mathrm{dF}_{cr}/\mathrm{dE} = 1.1\times 10^{-5}$ cm^{-2} s^{-1} TeV^{-1} sr^{-1} (calculated from the plot in Ormes and Freier 1978 [68], see Figure 2.5).

We utilized equation 2.22 for the estimation of the flux from nearby SBGs, and in addition, we checked that there are indications that the interaction dominant regime indeed takes place in them (estimated $\tau_{esc} \gg \tau_{int}$).

2.3 Source Selection

To select plausible SBGs for observation with the Whipple 10m telescope, we surveyed existing publications and considered $\sim$ 50 northern sky nearby SBGs with distance less than $\sim$ 100 Mpc. The selection list was refined by determining whether SBGs were detected in X-rays and in the radio bands, as a result of past intense star activities, evolution, and SN activities. X-ray, IR, and radio radiation

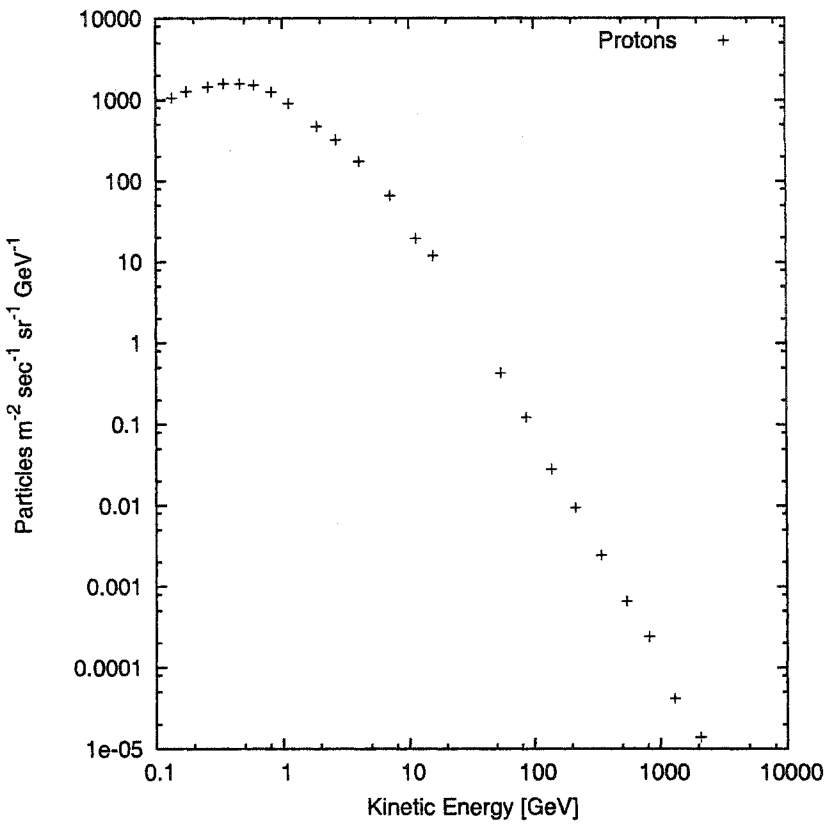

Figure 2.5. CR spectrum near the Earth (plot compiled from Ormes and Freier 1978 [68] by permission of the AAS). The proton spectrum is used for the gamma-ray flux estimation in section 2.2.2, since it is the highly dominant component of the total CR spectrum.

are typical indicators of synchrotron emission from accelerated CR electrons and from expanding SN shells. We checked that the ISM density is high enough in the starburst regions, so that $\tau_{esc} \gg \tau_{int}$ is likely satisfied. The exact information on magnetic fields in starburst regions is poorly known from existing publications. The final selection of targets is based on the evaluation of factor R_{sb}/R_{mw} $(1\mathrm{Mpc/D})^2$ as is shown in equation 2.22.

2.3.1 SN Rate Determination

The FIR luminosities from two lists of galaxies, the Pico dos Dias Survey (PDS) [69] and HCN survey [70], are investigated. HCN, which is one of the most abundant large dipole-moment molecules in galaxies, is good tracer of dense molecular gas. On the other hand, FIR luminosity is one of the frequently used tracers of SN activity. Thermal FIR luminosity is believed to be correlated with the warm dust heated by embedded massive OB stars, and nonthermal emission is due to SN activities. Strong linear correlation between FIR and HCN is also known [70]. Using the lists, SN rates are derived and sorted. The best 10 (northern sky sources) of the lists are shown in Tables 2.1 and 2.2. Arp220 and the southern sky source NGC253 are included in the list for comparison purposes. M82, IC342, and NGC2146 remain in both of the lists. SN rates are derived by the relation suggested by Manuucci et al. [71],

$$SN_r = 2.4 \times 10^{-2} \left(\frac{L_{FIR}}{10^{10} L_\odot}\right) yr^{-2}. \tag{2.23}$$

Also, Buren and Greenhouse [72] derived a similar relation,

$$SN_r = 2.3 \times 10^{-2} \left(\frac{L_{FIR}}{10^{10} L_\odot}\right) yr^{-2}. \tag{2.24}$$

This equation is derived by comparison of FIR luminosity and observed number of SN in other wave bands in nearby SBGs, such as M82 and NGC253.

Radio observations by Condon et al. [73] are also utilized to determine SN rate. SN rates and distance-weighted SN rates for NGC253, IC342, and NGC2146 are shown in Table 2.3.

Based on our survey of X-ray, IR, and radio emissions, together with the flux estimates, a group of SBGs was selected and proposed to the time allocation committee for observation with the Whipple instrument, resulting in approval of observations with large exposure on IC342 and shorter exposures on M81, M82, and NGC3079. M82 had been observed previously, and therefore data already existed.

Table 2.1. SBG candidates for VHE gamma-ray flux estimation selected from PICO DOS DIAS survey [69]. Calculated scaled SN rates are listed. The SN rates are scaled by distance square and SN rate in the Milky Way.

Object	Distance (Mpc)	$\frac{SNr_{sb}}{SNr_{mw}} \times (\frac{1Mpc}{D})^2$
M82	3.0	8.044E-01
ARP029, NGC6946	0.9	2.714E-01
NGC0253	3.4	2.087E-01
M51, ARP085	8.6	9.986E-02
ARP220, IC1127, IC4553	77.6	3.078E-02
NGC2146	15.8	2.749E-02
MRK0171, NGC3690	44.5	2.353E-02
IC0342	3.4	1.993E-02
NGC7771, MRK9006	61.1	1.780E-02
AM1025-433, NGC3256	38.9	1.768E-02

Table 2.2. SBG candidates for VHE gamma-ray flux estimation selected from HCN survey [70]. Calculated scaled SN rates are listed. The SN rates are scaled by distance square and SN rate in the Milky Way.

Object	Distance (Mpc)	$\frac{SNr_{sb}}{SNr_{mw}} \times (\frac{1Mpc}{D})^2$
M82	3.5	5.80E-01
NGC 253	2.5	5.19E-01
IC 342	3.7	1.58E-01
NGC 1068	16.7	1.57E-01
NGC 6946	5.5	8.16E-02
NGC 2146	15.2	6.68E-02
NGC 4631	8.1	4.71E-02
NGC 891	10.0	4.01E-02
NGC 3627	7.6	3.47E-02
NGC 2903	6.2	3.21E-02

Table 2.3. SBG candidates for VHE gamma-ray flux estimation selected from Radio survey [73].

Object	D (Mpc)	SN rate (yr^{-1})	$\frac{SNr_{sb}}{SNr_{mw}} \times (\frac{1Mpc}{D})^2$
NGC253	4.7	0.5	1.41
IC342	3.5	0.04	0.204
NGC2146	18	0.8	0.154

CHAPTER 3

SELECTED STARBURST GALAXIES

Flux estimations described in Chapter 2 are performed for some SBG candidates and shown in the Figure 3.1 with Arp220 as a comparison. The NGC253 flux estimate is almost exactly the same as M82 (therefore it is not shown in the Figure 3.1). As mentioned previously, TeV gamma-ray emission has been reported from NGC253 [7], which is the only such report of VHE radiation detected from an SBG to date. Flux estimates suggested that in the northern sky, the best SBG candidates are

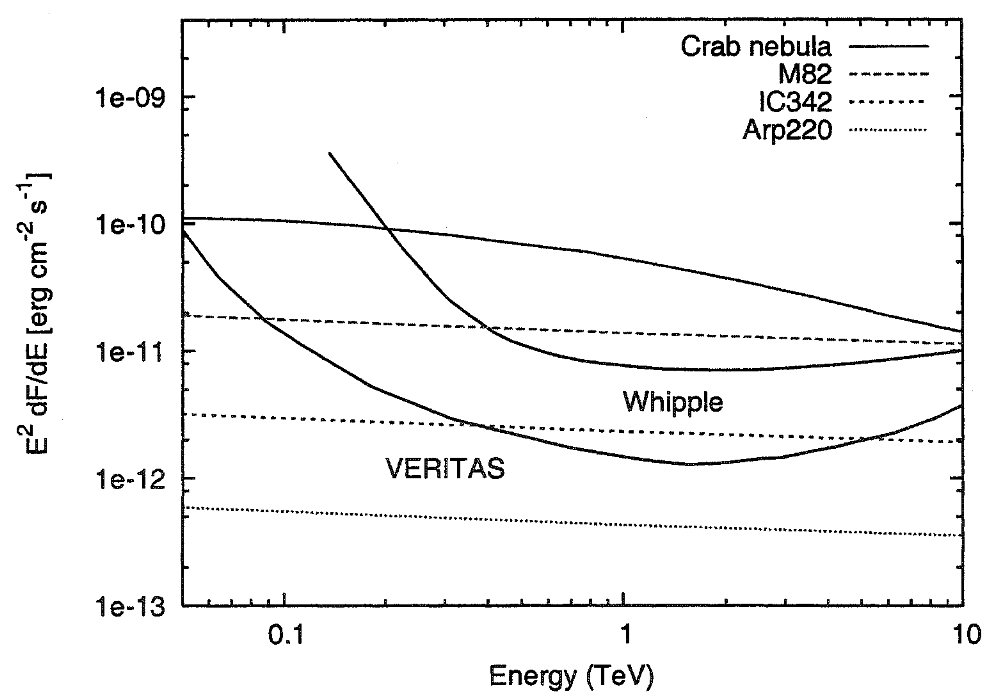

Figure 3.1. Flux estimates of selected SBGs: Whipple and VERITAS sensitivities are for 50-hour exposure and energy resolution of four log-equidistant bins per decade.

IC342, M82, and to a lesser extent M81, NGC2146, and NGC3079. IC342, M81, M82, and NGC3079 were selected as targets for observation with the Whipple telescope. Among those, IC342 was later chosen as the principal potential source for farther investigation based on the flux estimation, short exposure observations, and lack of significant conflict with other sources approved by the Whipple time allocation committee for observations during the same season.

3.1 NGC253

NGC253 is the only SBG (subclass of "normal" galaxy) from which TeV emission has been reported (CANGAROO collaboration in 2002 [7], see Figure 3.2). The gamma-ray emission from this source, with statistical significance of $\sim 11\sigma$ level, was claimed to be due to IC by relativistic electrons which spatially extend to the scale of 10 kpc into the galactic halo. The differential photon spectral index is ~ 3.75, and the integrated flux is claimed to be $(7.8{\pm}2.5)\times10^{-12}$ $cm^{-2}s^{-1}$ at energy greater than 0.52 TeV. NGC253 is an edge-on spiral galaxy at a distance of ~ 2.5

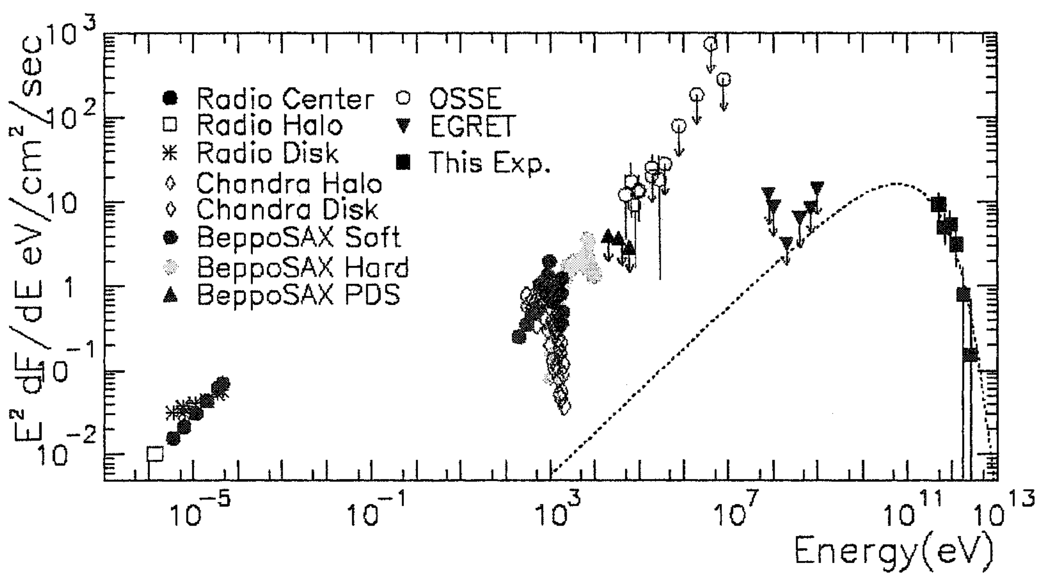

Figure 3.2. Reported NGC253 spectrum (plot reproduced from Itoh et al. 2002 [79] by permission of C. Itoh.) The mechanism is claimed to be the inverse Compton by extended relativistic electron halo.

Mpc, in the southern sky (RA 00h47m33.1s, DEC -25d17m18s). Although this source is not confirmed by another IACT observatory yet, the reported detection provides additional motivation for the search for VHE gamma-ray emission from other SBGs. As is shown in Tables 2.1, 2.2, and 2.3, in the previous chapter, the estimated SN rate and distance scaled SN rate in NGC253 are always one of the highest in all scalings. The SN rate predicted by Buren and Greenhouse 1994 [72] is ~ 0.1 per year. The interstellar proton density in the starburst regions in NGC253 is estimated $\geq 10^4$ protons/cm^3 and probably even larger (e.g., [74] [75] [76]). In some molecular clouds in NGC253, the estimated density reaches $\sim 10^6$ protons/cm^3 [66]. Diffuse X-ray emission from the inner $\sim$ 10 kpc central region has been detected, which presumably indicates a high star formation and SN activity (e.g., [77]).

3.2 EGRET Observations of SBGs

Gamma-ray emission from SBGs was not discovered by EGRET in the energy range 30 MeV to 30 GeV. Upper limits are derived for some galaxies, e.g., M82 and NGC253 [78]. It is important to note that the detection of gamma rays with energy in the sub-TeV to TeV range by ground-based telescopes is possible, even if the gamma-ray flux in the MeV to GeV region is lower than the EGRET sensitivity. However, a nondetection by EGRET would set a limit on the possible gamma-ray prediction and propagation mechanisms, perhaps favoring the leptonic origin of the spectrum.

In Figure 3.3, the softest simple power-law spectra which would be barely detectable by EGRET but could be detected by Whipple (5σ, 50 hours) and VERITAS (5σ, 50 hours) are shown. The power indices derived for these spectra are ~ 2.1 to be detected by the Whipple telescope and ~ 2.3 for the VERITAS array. If the spectrum observed by the Whipple or VERITAS telescopes were to have a softer power index, then there must be either a cut-off in the acceleration mechanism or inferred absorption feature generated at the VHE emission site, or the production mechanism of gamma-ray flux is IC, allowing the flux in EGRET energy band to

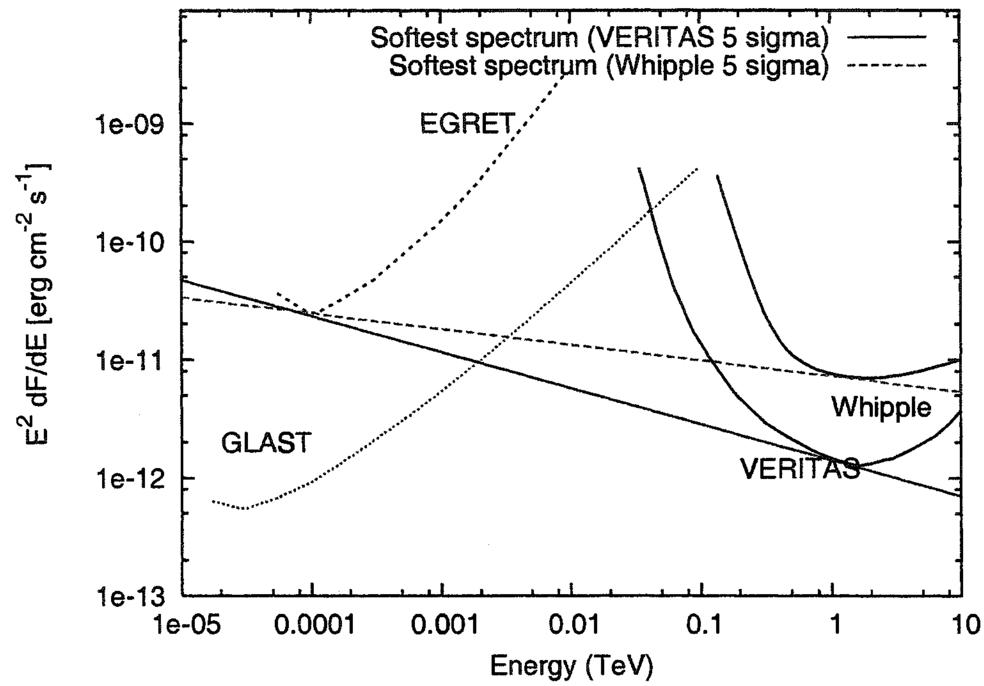

Figure 3.3. Various sensitivities and the softest possible flux. The sensitivities for Whipple and VERITAS are for 50-hour exposure and energy resolution of four log-equidistant bins per decade. The curves for EGRET and GLAST are for 1-year exposure. The softest flux lines show possibilities of gamma-ray emission detectable by the ground-based telescope without being detected by EGRET.

be much lower than established upper limits. The latter possibility was invoked to explain the detection of NGC253 by the CANGAROO collaboration [79]. The suggested emission mechanism is electron IC in the galactic halo of NGC253 with index -3.74, where the maximum Lorentz factor of the electrons introduces a steep cutoff.

3.3 Starburst Galaxy IC342

A recent study of the average distance to the IC342 galaxy group reports a value of ~ 3.28 Mpc, by Karachentsev et al. 2003 [80], consistent with the value of ~ 3.6 Mpc estimated by Krismer et al. 1995 [81]. IC342 is oriented nearly face on to our line of sight, with inclination less than 20 degrees. IC342 appears in the sky close to the Galactic plane, which is not ideal for observations, especially in the optical band, due to strong galactic extinction. Its optical size is about 21'× 21', and the optical luminosity of the disc is rather small. This galaxy is known to have a small stellar bar at the center and is stretched in the N-S direction, e.g., [82] [83]. The size of the major axis is several arcmin, and it has an "S" shape structure in the central part.

A number of gas morphology studies have been conducted for this galaxy. Regions with active star formation produce luminous radio and infrared emission, due to continuous heating of the ISM as a result of the intense UV emission and stellar winds from many massive young stars in the region. X-ray emission from the region also results from high energy CRs energized in many SN explosions of massive stars in the region.

The CO gas distribution, which is a good measure of cold H_2, has a bright central peak in the central 15 arcmin [84]. A prominent CO bar with size 2' × 5' is also seen. The central peak plus this bar contain 30% of the total observed CO emission in IC342. Neutral gas surface density (H_2 + HI) sharply peaks at the center, particularly within a radius of central 5 arcmin.

The starburst nature of the nucleus of IC342 has been known for at least 25 years, e.g., [85] [86] [87]. Both infrared observations [85] and radio observations [86] indicate strong star formation activity in the inner ~10 arcsec of the nucleus. Higher resolution observations in a variety of wave bands have revealed an interesting morphology and ISM gas dynamics of the starburst region which is mostly confined in the central ~15 arcsec of IC342.

3.3.1 Radio and Infrared Observations

The radio emission of IC342 has been extensively studied. A number of radio observations (CO, and NH_3 transition lines) have shown the detailed gas morphology of the IC342 nucleus, e.g., [88] [89] [90] [91] [92] [93]. They all agree well on the structure of the nuclear bar. Ishizuki et al. [91] suggested that emission from the nuclear region, with the size scale greater than 130 pc (adopted distance is 4.5 Mpc in the publication) may be produced by bremsstrahlung radiation from accelerated CRs.

High resolution observations in the near-infrared (NIR) also showed clumpy ring-like structure of gaseous material with a radius of ~5 arcsec around the dynamical center of IC342 [94]. These observations indicate that the arm-induced flows of molecules intersect with this inner ring and are forced to rotate along the ring [95]. The incoming gas is compressed at the intersecting regions and giant molecular clouds are created. This gaseous ring with the giant molecular clouds is the main star-forming region of IC342.

Meier and Turner [93] presented high resolution (~2 arcsec) radio emission of ^{18}CO from the IC342 nuclear region. Two strong emission sites are observed which correspond to the arm-ring interaction sites. These locations coincide with the gas ring discussed above [94] and also with the HST H_α image of IC342.

3.3.2 X-ray Observations

Bright X-ray emission from the nuclear region is observed [96]. Higher resolution X-ray observations with ROSAT also revealed emission which coincides with this nuclear star-forming region [97]. The most luminous source of X-rays from the IC342 nuclear region coincides almost exactly with the ring location, H_α, and CO emission site, discussed above (see Figure 3.4). Bregman reported the X-ray luminosity of central region to be 1.5×10^{39} erg s^{-1}, with a diameter of 400 pc (adopted distance = 4.5 Mpc in [97]). These emissions may indicate intensive heating of gas by multiple SN explosions and massive stars in the region, which created hot gas bubble [97].

3.3.3 Arm-ring Structure in the Center of IC342

To summarize, the inflow of gaseous material along the arms is responsible for the "S"-shape nuclear structure in the IC342 bar, which intersects the central ring. Large molecular clouds are created by compression at these intersections, resulting in active star formation (Figure 3.5). The age of the star-forming region in IC342 is estimated as ~4-6 Myrs [94]. The flow of the gas continuously supplies protons to the star-forming regions keeping the density of the gas high (n[H_2] $\sim 10^{4.6}$ cm^{-3} [74]) and preventing the evacuation of material due to strong UV radiation and

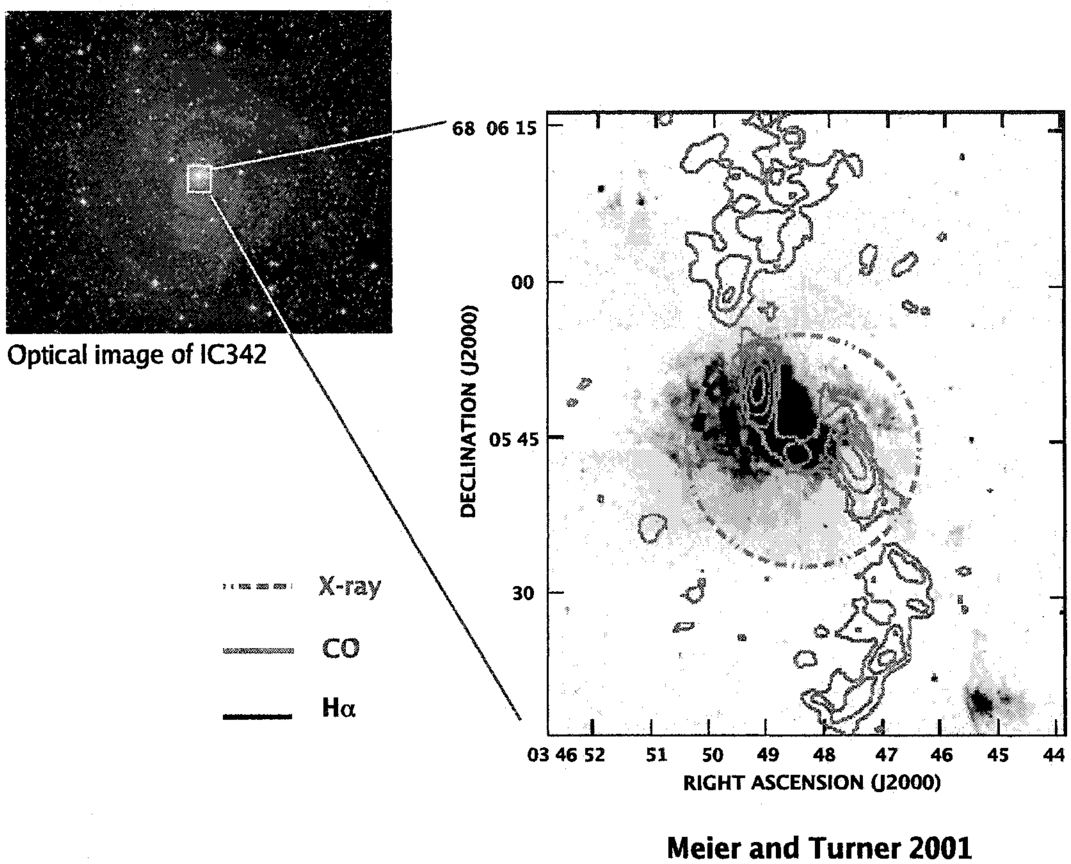

Figure 3.4. Central 15 arcsec of IC342 core (plot reproduced from Meier and Turner 2001 [93] by permission of the AAS). H_{α}, CO, and X-ray maps are superimposed. The circle indicates the location of X-ray emission detected by Bregman et al. 1993 [97].

stellar wind from massive stars and shock waves from multiple SNe.

The rate of O and B star formation in the IC342 nucleus is $\sim$0.2 $M_{\odot}$ yr^{-1}, $\sim$ 20 times higher than the rate at the center of the Milky Way Galaxy [98]. The dynamical interpretation discussed in the previous paragraph agrees with models introduced by, e.g., [99].

A small scale molecular disc formed by the gravitational potential well is also observed inside of the ring, close to the dynamical center of IC342 [100]. Although this disc coincides with the luminous young stellar cluster, it seems not to be old

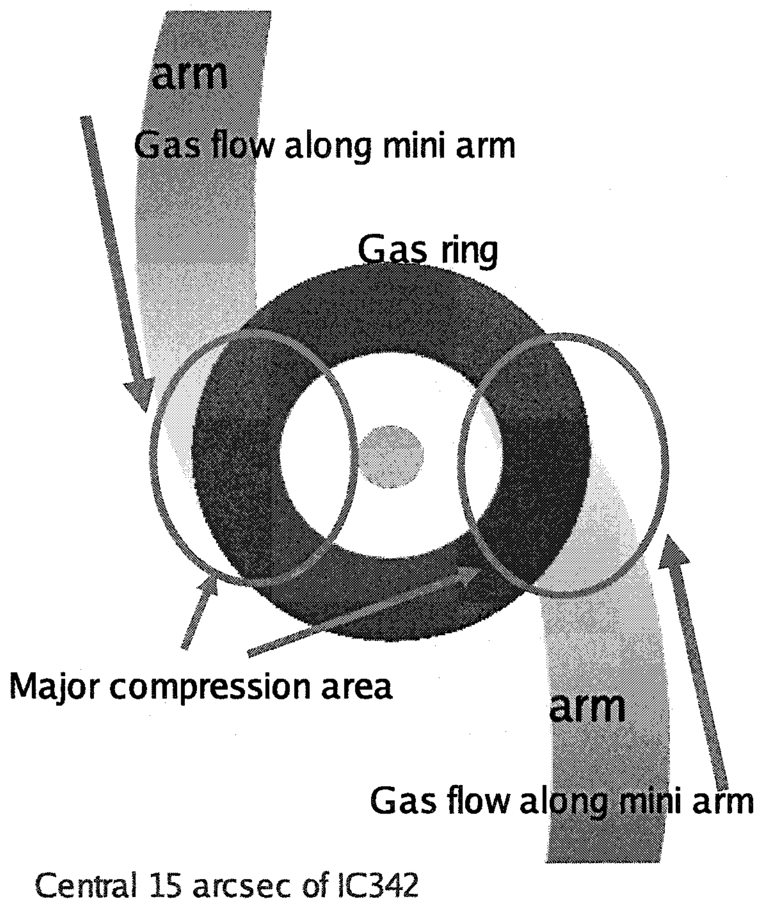

Figure 3.5. Cartoon of the central starburst regions near IC342 core. Continuous gas flow along two miniarms are known from observations of CO emissions.

enough to support SNe. However, this observation might show that the starburst in this galaxy is periodic. It is reported that the central star clusters experienced a major burst of star formation $\sim$ 60 Myr ago [101]. The hollow space inside the ring is believed to be created by the pressures from OB stars and SNe in the former starburst era. A schematic of the nuclear region of IC342 is shown in Figure 3.5.

3.4 M82

M82 is one of the most well-known and studied SBGs. It is an edge-on galaxy, at a distance of $\sim$ 3.5 Mpc. A midmass ($\sim$ 460 $M_\odot$) black hole is expected to exist in its central starburst region [102]. Starburst drives a large scale bipolar outflow of gas along the galaxy's minor axis. The outflow in kpc-scale is believed to be produced by pressure from frequent SN explosions in the central region, and it can be seen in the optical and X-ray wave bands. The star formation activity is occurring in the central part of the galaxy and likely to be the result of strong gravitational interaction in the past with its companion galaxy, M81 (discussed in the following section). M82 is bright in the radio, X-ray, and infrared. However, the optical flux from the star formation region is lower than could be expected due to absorption by dense dust. The interstellar proton density in the starburst region is estimated to be $\sim 10^4$ protons/cm^3 [66], making M82 one of the most gas-rich SBGs. Diffuse X-ray emission extending to $\sim$ 6 kpc from the central region is also detected, e.g., [77], indicating perhaps a history of past intense star formation and SN activities. The SN rate estimated by van Buren [72] is $\sim$ 0.1/yr, which is as high as in NGC253.

3.5 M81

M81 is located only 36' south of M82 and interacts strongly with its companion. M81 is a large spiral galaxy with inclination $\sim 60°$ and is twice as massive as the Milky Way. UV observations [103] show intense emission from the core and from the spiral arms. In this galaxy, the star-forming regions are in the arms, not at the center where star formation typically occurs in SBGs. The size of the star-forming region is much larger than the typical value of a few 100 pc. The X-ray emission from M81 is relatively bright, $\sim 3 \times 10^{40}$ ergs s^{-1}, and comprises a diffuse component and multiple point sources [104] [105]. One fourth of the total emission originates outside of the central region and 90% of this is from noncentral point sources [105], which coincide with the locations of SNRs and superbubbles. The diffuse component overlaps the UV intensity profile, indicating an association with recent massive star formation activities. Approximate estimate of the star-forming region is ~ 5 kpc, corresponding to the size of the molecular cloud and X-ray, UV emission regions. This source was chosen for observation due to this large volume of star-forming region, in spite of its relatively small SFR and ISM density compared to the other candidates.

3.6 NGC3079

NGC3079 is a nearly edge-on galaxy at a redshift of $z = 0.0037$, corresponding to a distance of ~ 15 Mpc ($H_0 = 75$ km s^{-1} Mpc^{-1}). The most remarkable characteristic of this galaxy is the massive central galactic superwind, which can be observed over a wide range of wave bands. The wind is likely powered by an AGN-like mechanism [106] or intensive starburst near the core [107]. The mean density of the core can be determined by CO radio line emission and is observed to be high, 3×10^3 H_2 cm^{-3} [108], or even higher from estimates using CS emission, $\sim 10^4$ [109].

CHAPTER 4

OBSERVATIONS

TeV gamma-ray observations of the selected SBGs: IC342, M82, M81, and NGC3079, were conducted from January 2001 to March 2004, using the Whipple 10m IACT, a single telescope ground-based gamma-ray detector. The telescope is located 40 miles south of Tucson on Mt. Hopkins at the altitude $\sim$ 2.3 km above sea level. After final data screening (see section 4.2), a total exposure of 164.6 ksec was obtained on IC342, 48.6 ksec on M82, 107.2 ksec on M81, and 68.0 ksec on NGC3079.

Observations are performed only on clear dark nights when the moon is below the horizon and the sun is at least 18° below the horizon. Observations are typically suspended when the relative humidity is above $\sim$ 75%, due to possible arcing on the camera from the high voltages applied to the PMT. This arcing triggers the system at a higher rate than the telescope can operate and damages the shielding of the PMTs. Wind speed is also carefully monitored to avoid introducing tracking errors. Each night, a 10-minute "zenith run" is performed with the telescope pointing at the zenith, to determine the atmospheric condition of the night. Using the data from the zenith run, a "throughput factor" is calculated, which is a scale of brightness of the Čerenkov radiation from CR EAS, representing the condition of the atmosphere and the telescope for observing night.

Occasionally, during observations PMT currents much larger than the average level can be produced due to stars in the field of view, which increases the background beyond the ambient NSB level. PMT currents are continuously monitored by the observers during the course of the runs, and these pixels are manually turned off during the runs or in software during analysis.

4.1 Observation Modes

Observations with the Whipple 10-m telescope are made in one of three standard operation modes. A 28-minute exposure while tracking the source position to within $0.1°$ is called an "ON" run. Typically an ON run is either followed or preceded by a 28-minute OFF run, for which the telescope is pointed 30 minutes off source position in right ascension to provide an independent estimate of the CR background rate over the same patch of the sky as the ON run. An ON run without a corresponding OFF run is called a tracking (TRK) run. A summary of the observation exposure on each of the SBGs is shown in Table 4.1.

4.2 Data Selection

Selection of data for analysis is based upon the average camera pixel noise level, throughput factor, rate of malfunctioning (or turned off) pixels, and zenith angle. The weather condition during the observations is also considered. Each observing night, the sky condition is monitored by the observers and rated based on the amount of clouds and haze. Only data taken under A and B sky conditions (no clouds in the FOV) are chosen for analysis. Runs with high average noise, $\sim 2-3\sigma$ larger than the average ($\sim$ 5 qADC counts) are eliminated from the final data set. After the average noise levels are checked, the $\sim$ 10 noisiest pixels are investigated. If they correspond to background stars, the data from these pixels are removed from the analysis. Data taken with zenith angle greater than $40°$ are not included into the analysis. After the screening, the total accumulated exposure shown in Table 4.2 were used for standard analysis (discussed in Chapter 5). Only ON runs

Table 4.1. Time summary of exposure of SBGs observed by the Whipple telescope. The exposures are before final data selection screening.

Source	Total (ksec)	ON, TRK (ksec)	OFF (ksec)	ave. zenith (deg)
IC342	286.9	164.5	122.4	40.0
M82	56.2	46.8	9.4	39.9
M81	110.2	81.4	28.8	38.2
NGC3079	84.6	67.7	16.9	26.9

Table 4.2. The total amount of data used for analysis after screening.

Source	Total (ksec)	ON, TRK (ksec)	OFF (ksec)
IC342	164.6	84.8	79.8
M82	48.6	40.3	8.3
M81	107.2	78.8	28.4
NGC3079	68.0	51.4	16.6

having corresponding OFF runs were utilized for the multidimensional Maximal Likelihood Method (MLM, see Chapter 5).

CHAPTER 5

ANALYSIS

More than 99% of the events triggering the Whipple 10-m IACT are due to the isotropic background of CR. For a single telescope such as the Whipple, discrimination between gamma-ray events and hadronic events is an essential part of the data analysis. Rejection of hadronic events is achieved by exploiting the power of the 379 channel Whipple camera to form high resolution images of the shower development in the atmosphere. The distribution of image parameters is different for gamma rays and CR events, reflecting the differences which result from the different physics driving the EAS development, as described in Chapter 1. Utilizing the difference in these distributions, $> 99\%$ of the hadronic events can be rejected while still retaining $\sim 50\%$ of the gamma-ray events. By comparing the number of events which pass a set of cuts on the image parameters for the ON source and background exposures, an excess of gamma-ray-like events can be detected, and its statistical significance is determined. Two independent analysis methods are used in this dissertation. The first is the standard cuts customarily used for analyzing Whipple data sets. The second is a multidimensional maximal likelihood approach, which is tuned to the spectrum of the source. In this chapter, the techniques used in the calibration of the Whipple 10-m gamma-ray detector, the data preparation processes, and the two analysis methods used are discussed.

Calibration of the Whipple camera has two stages: relative calibration of individual channels and the absolute calibration of the instrument as a whole. Relative calibration is used to equalize responses of each channel to a uniform light source. Absolute calibration is used to determine the ratio between the digitized output from the DAQ and actual photo electron charge count produced by a "mean" PMT.

This step is necessary to reconstruct the energy of gamma rays accurately from the light collected by the camera.

5.1 Flatfielding

Incoming photons initiate a cascade of electrons in each PMT. When the system is triggered (see section 1.3.4), the charge measured by each PMT is amplified, then digitized by a ADC (qADC, in the diagram), and stored (referred to as "qADC counts" hereafter). The gain of each PMT is adjusted by changing the voltage across its dynode chain. The gain is found to change in proportion to the voltage to the eighth power. However, the amplitude of the qADC output for a uniform signal across the camera varies slightly from channel to channel, even with the same PMT voltage settings. This discrepancy between channels is largely removed by adjusting the PMT cathode voltage settings so that the response of every channel to a calibrated incoming light source is the same. This process is called "active flatfielding." The small discrepancies, which remain after this adjustment procedure, are removed using a software gain adjustment process while the data are analyzed (discussed later in this chapter). Before active or software flatfielding can occur, the relative gain of each channel must be estimated.

In the past, the relative gains were estimated by illuminating the camera with light from a light source: pulses from a nitrogen arc lamp. The nitrogen flasher is installed at the center of the main reflector and produces light pulses, which uniformly illuminate the camera. At the beginning of each observing night, 1 minute of data is taken with the pulsar switched on. These data are used to determine the relative gains. This method is simple to apply; however the shape of the pulses differs substantially from those produced by Čerenkov light, which introduces the potential for systematic errors in the gains calculated. To avoid this possible systematic error, the actual CR background data can be used as an alternative light source for flatfielding.

5.1.1 Flatfielding with CR Data

More than 99% of the events triggering the Whipple instrument are produced by background CR events. When events in a normal data run are histogramed by qADC counts, the differential rate exhibits a simple power law over most of its range. At the low end of the histogram, corresponding to low light levels, there is considerable deflection from this power-law relation due to the effects of the trigger which does not record events below a certain threshold. At the high end, the histogram may deviate from a power law due to lack of statistics (see Figure 5.1). The relationship between the differential rate and the qADC counts can be written as

$$log\left(\frac{dN}{d(qADC)}\right) = -\alpha \times log(qADC) + logC \tag{5.1}$$

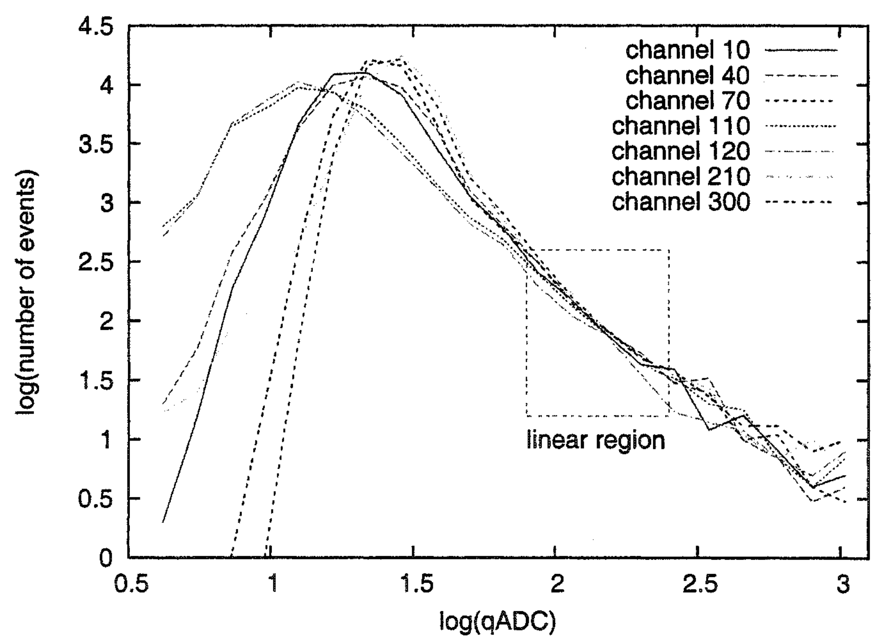

Figure 5.1. Histograms of the number of events per logarithmic bin of qADC counts. The channels shown are randomly picked from the camera. All histograms correspond to a 28-minute telescope run. The boxed area shows the linear segment used for gain calculation.

where α is the index, and C is a scaling factor for the channel. By combining data from $\sim$ 50 real 28-minute runs, an average of index 1.65±0.03 was estimated. This value is adopted as a constant in the further analysis. In the histogram (Figure 5.1), the segment between log(qADC) = 1.9 and 2.4, where all channels have reasonable statistics, is used for gain calculation. The data points were fitted with a line.

Uneven gains across the camera are manifested as lateral shifts of the power low segments of the differential rate curves with the power law index fixed. The degree of lateral shift is directly mapped to the intercept of the fitted line with the y-axis in log-log space. A least squares fit for the intercept (with fixed slope of 1.65) is performed. The mean scaling factor is then calculated. If the scaling factor for ith channel is denoted as C_i and their mean as F_0 then

$$logF_0 \equiv \frac{\sum logC_i}{N_{tot}} \tag{5.2}$$

where N_{tot} is the total number of functioning channels in the camera for the run. The relative gain ($\equiv g_i$ hereafter) is defined as the number with which the qADC values must be multiplied to flat field the camera. Therefore,

$$-1.65 \times (log(qADC) + log(g_i)) + logC_i = -1.65 \times log(qADC) + logF_0. \tag{5.3}$$

Then, the ith relative gain is

$$g_i = \left(\frac{F_0}{C_i}\right)^{-\frac{1}{1.65}}. \tag{5.4}$$

Malfunctioning channels and ones turned off during a run are excluded from the gain calculations. In active flatfielding, the voltage settings (denoted as "HV" here) for the PMTs are determined by the following log linear equation, which has been tuned experimentally to give a reasonable approximation,

$$(HV^{new})_i = (HV^{old})_i - 300 \times log(g_i). \tag{5.5}$$

This process is done iteratively (typically three, four times) to arrive at convergence of the relative gain. For the first iteration only, an additional -10 V is applied to account for the effects of PMT degradation since the beginning of last observation season.

At the beginning of the 2002 - 2003, 2003 - 2004, and 2004 - 2005 observation seasons, this method was successfully applied to flat field the Whipple camera PMTs. The latest flatfielding done between the end of October 2004 and the beginning of November 2004, reduced the RMS deviation of relative gains from 6.0% to 2.6% after four iterations (Figure 5.2).

5.2 Absolute Calibration - DC to PE Conversion

In the imaging atmospheric technique, the energy of the primary gamma ray is estimated from the shape of the image and the total number of photoelectrons (PE) recorded by the camera. The relationship between the digitized qADC counts (DC) and the number of photoelectrons in the PMT must be established. This "absolute" calibration of the instrument is difficult to establish directly; the response of the each component of the instrument (mirrors, PMTs, amplifiers, cables, ADCs) must be carefully measured and combined to give the DC/PE conversion factor. An indirect measurement can be made using a "calibrated light source," namely, the Čerenkov light produced by local muons (mean lifetime at rest 2.20 μs, $m_\mu c^2$ = 105.66 MeV/c^2, and charge = ±1).

The muons are created in abundance in proton-induced EAS, as a result of the decay of the charged pions (discussed in section 1.3.2). Because the amount of Čerenkov light produced by the muon can be analytically or numerically calculated,

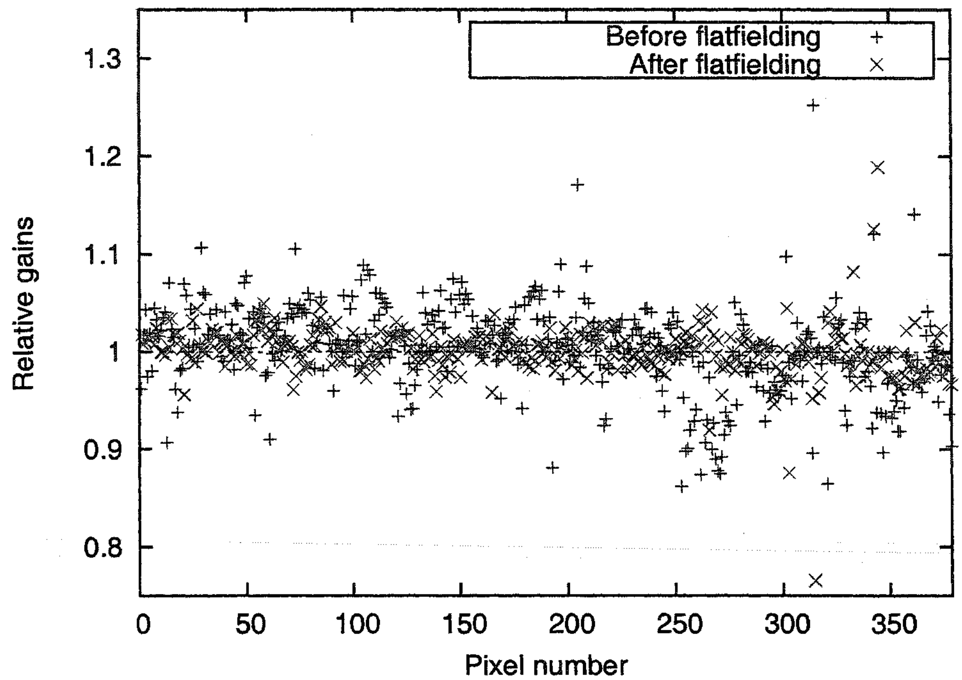

Figure 5.2. Relative gain distribution before and after the 2003-2004 season camera flatfielding.

the DC/PE conversion factor can be obtained by finding the ratio between the signals produced by real muons in the qADCs and simulated muons.

5.2.1 Čerenkov Radiation from Muons

The energy loss of a traveling charged particle due to Čerenkov radiation per unit length along the path of the particle is given by [40],

$$\frac{dE}{dl} = \frac{(Ze)^2}{c^2} \int_{\epsilon(\omega)>(1/\beta^2)} \omega \left(1 - \frac{1}{\beta^2 \epsilon(\omega)}\right) d\omega \tag{5.6}$$

where

Ze - charge of the particle

ω - angular frequency of radiated photon

$\epsilon(\omega)$ - permittivity of the medium in which the particle propagates

The integrant in equation 5.6 describes how photon energy is distributed per frequency interval $d\omega$. Since

$$\frac{dE}{dld\omega} = \frac{dN_\omega}{dld\omega}\hbar\omega$$

where N_ω is photon number density with frequency ω, with equation 5.6 and $Z = 1$ for muons, the number of photons emitted per unit of muons' path length is

$$\begin{aligned}
\frac{dN_{photon}}{dl} &= \frac{e^2}{c^2\hbar}\int_{\epsilon(\omega)>(1/\beta^2)}\left(1-\frac{1}{\beta^2\epsilon(\omega)}\right)d\omega \\
&= \frac{\alpha}{c}\int_{\epsilon(\omega)>(1/\beta^2)}\left(1-\frac{1}{\beta^2\epsilon(\omega)}\right)d\omega \\
&= 2\pi\alpha\int\left(1-\frac{1}{\beta^2\epsilon(\lambda)}\right)d\left(\frac{1}{\lambda}\right) \qquad (5.7)
\end{aligned}$$

where α is the fine-structure constant ($= e^2k/\hbar c \simeq 1/137$, where $k = 1/4\pi\epsilon_0$ for SI units, $k = 1$ for Gaussian units).

To convert the Čerenkov photons into photoelectrons in the PMTs, two major factors must be taken into account: reflectivity of the telescope optics and quantum efficiency of the PMT photocathode. The reflectivity, which is a function of photon frequency, determines how many photons actually reach to the PMTs. The PMT quantum efficiency, which is also a function of frequency, determines the probability that incoming photons reflected by the main reflector are detected by the PMTs. Taking these effects into consideration, we find

$$\frac{dN_{pe}}{dl} = 2\pi\alpha\left(1-\frac{1}{\beta^2n^2}\right)\int_{\lambda_1}^{\lambda_2}Q(\lambda)R(\lambda)d\left(\frac{1}{\lambda}\right) \qquad (5.8)$$

where

$Q(\lambda)$ - Quantum efficiency of the PMTs

$R(\lambda)$ - Reflectivity of the telescope optics

The term in parentheses can be taken out of the integral, since the frequency dependence of the permittivity of the atmosphere (and hence its index of refraction) is negligibly small over the frequency band of the sensitivity of the PMT.

$$\frac{dN_{pe}}{dl} = 2\pi\alpha \sin^2\theta_c \int_{\lambda_1}^{\lambda_2} Q(\lambda)R(\lambda)d(\frac{1}{\lambda}). \tag{5.9}$$

Using equation 1.2 and 1.3, we derive

$$\left(\frac{\sin\theta_c}{\sin\theta_{max}}\right)^2 = \frac{1}{\beta^2}\left(1 - \left(\frac{E_{min}}{E_\mu}\right)^2\right),$$

where E_μ is energy of the propagating muon; thus,

$$\sin\theta_c = \sin\theta_{max}\sqrt{1 - (\frac{E_{min}}{E_\mu})^2} \tag{5.10}$$

assuming that β becomes nearly unity for highly relativistic muons.

The total number of photons received by the telescope strongly depends on the relative position of the main reflector with respect to the muon impact point on the ground. The impact parameter ξ is defined in terms of distance, l, between the center of the telescope reflector and the muon impact point scaled with the radius of the mirror, r (see Figure 5.3),

$$\xi = \frac{l}{r}.$$

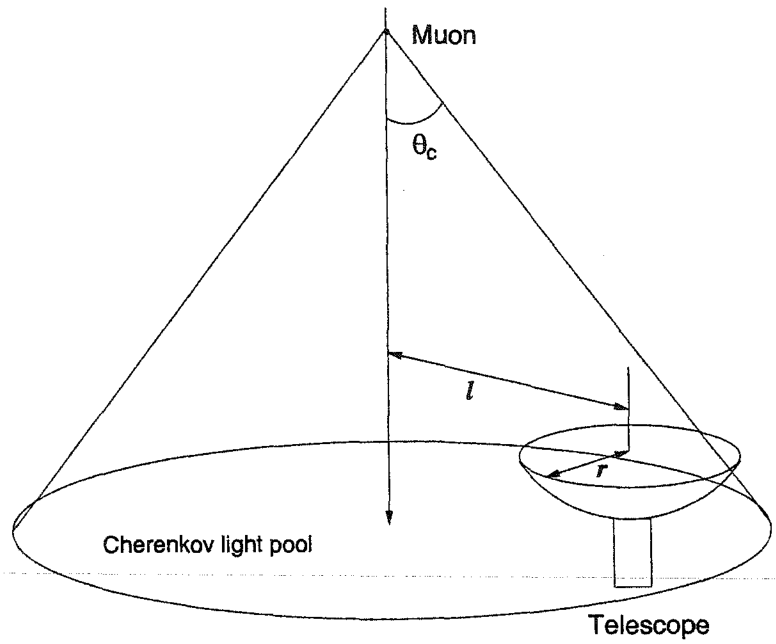

Figure 5.3. Impact parameter $\xi = l/r > 1$.

When a muon directly passes through the center of the reflector, the radiation received by the telescope is emitted by the muon over a path length of $D/(2\sin\theta_c)$ where D is the diameter of the telescope. By integrating equation 5.9, the total photoelectron count in the PMT can be expressed as

$$\begin{aligned} N_{pe} &= 2\pi\alpha\sin^2\theta_c \int_{\lambda_1}^{\lambda_2} Q(\lambda)R(\lambda)d\left(\frac{1}{\lambda}\right)\frac{D}{2\sin\theta_c} \\ &= \pi\alpha\sin\theta_c D \int_{\lambda_1}^{\lambda_2} Q(\lambda)R(\lambda)d\left(\frac{1}{\lambda}\right). \end{aligned} \tag{5.11}$$

It is convenient to define a scaling constant U_0 as

$$\begin{aligned} U_0 &\equiv \pi\alpha\sin\theta_c D \int_{\lambda_1}^{\lambda_2} Q(\lambda)R(\lambda)d\left(\frac{1}{\lambda}\right) \\ &= \pi\alpha D\sin\theta_{max}\sqrt{1-(\frac{E_{min}}{E})^2}\int_{\lambda_1}^{\lambda_2} Q(\lambda)R(\lambda)d\left(\frac{1}{\lambda}\right). \end{aligned} \tag{5.12}$$

For small θ_c,

$$U_0 \simeq \pi\alpha\theta_c D \int_{\lambda_1}^{\lambda_2} Q(\lambda)R(\lambda)d\left(\frac{1}{\lambda}\right). \tag{5.13}$$

The quantity U_0/θ_c is independent of either θ_c or ξ. The DC/PE conversion factor is then determined by calculating the ratio of the factors obtained from real muon images and simulated images. The weighting factors can be found directly from the parameters used to characterize muon images formed in the camera.

The images formed by the camera represent the intensity of incident photons mapped into angular space. A beam of incident light is mapped to a point on the camera plane whose location is determined by the direction of the initial beam with respect to the optic axis (Figure 5.4). For example, parallel beams of light incident on the reflector perpendicular to the camera plane are mapped to a point of the center of the camera. If a muon is incident on the center of the reflector,

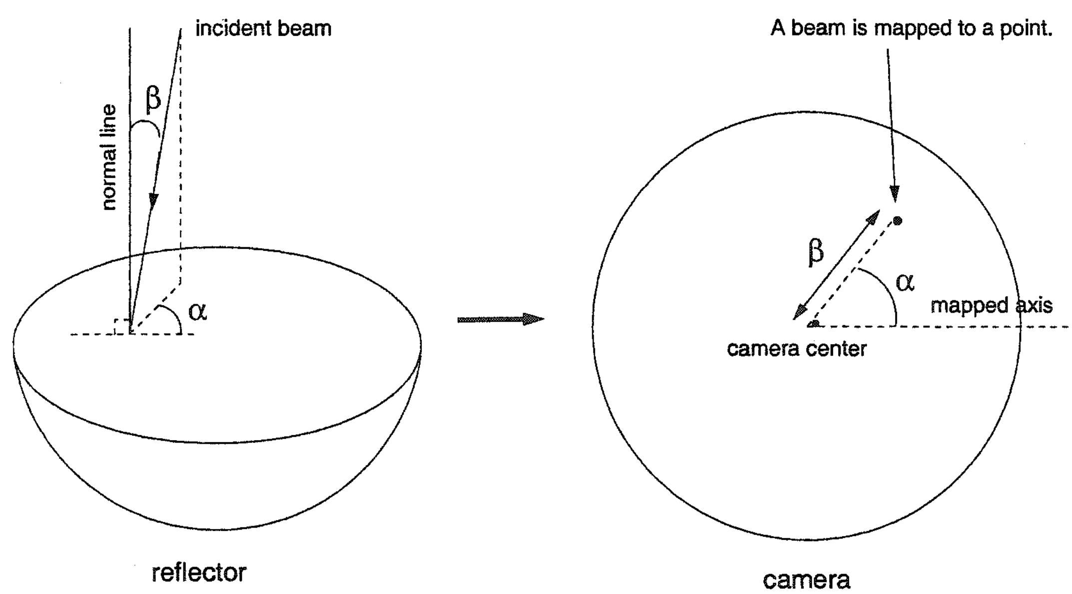

Figure 5.4. Mapping of a beam of light (real coordinate space) to the camera plane (angular space).

its Čerenkov light forms the image of a complete ring. If the impact parameter is greater than 1, i.e., it hits the ground outside of the reflector, the image becomes partial ring in the camera (Figure 5.5). An example of a real muon image is shown in Figure 5.6. The parameters which characterize the incident muons, ξ, *Energy* (equivalent to θ_c), and U_0, are mapped into angular (camera) space as a set of image parameters *Width*, *Length* of the muon ring and qADC charge. From these, the DC/PE conversion factor can be found. Details of the image parametrization is discussed in section 5.3.5 and Appendix A.

5.2.2 Muon Images with $\xi < 1$

A set of coordinates are chosen to describe an arbitrary point P with respect to the center of the reflector (origin O) in terms of the muon impact point P_0, as shown in Figure 5.7. The point P can be written as

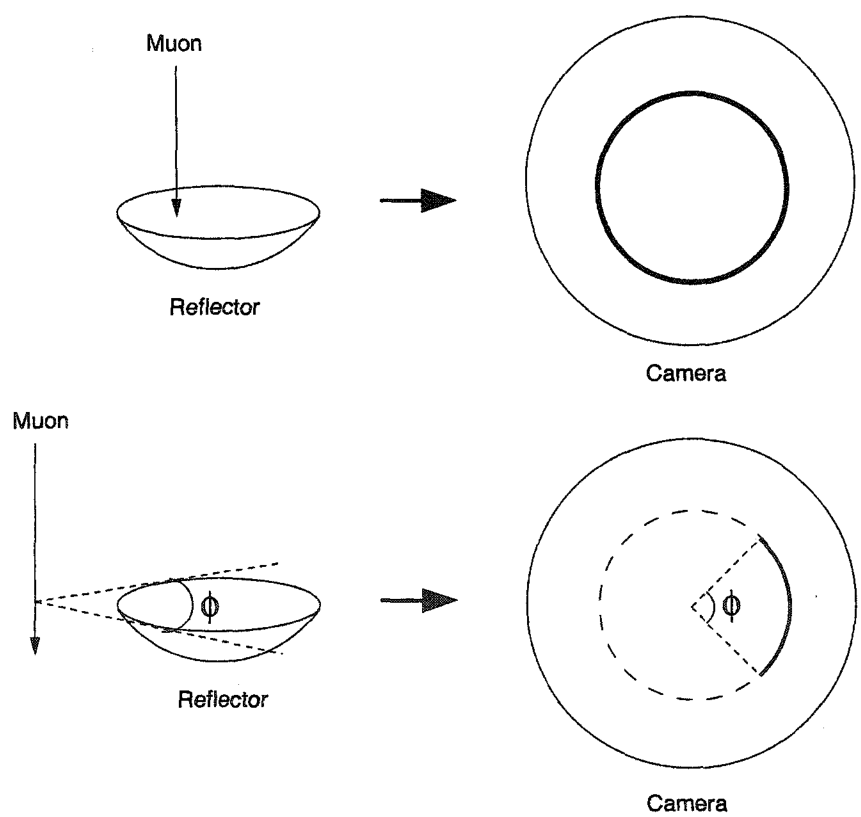

Figure 5.5. Images from muons with different impact parameters.

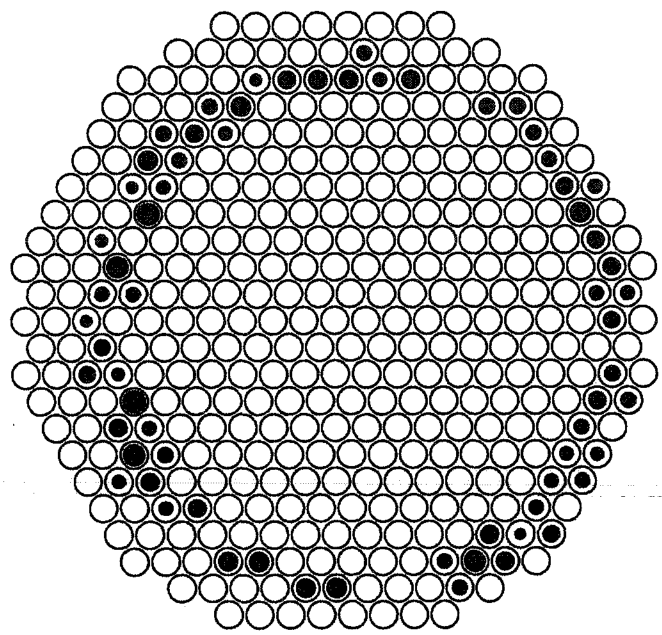

Figure 5.6. An example of the real muon image.

$$P = \begin{pmatrix} x \\ y \end{pmatrix} = \begin{pmatrix} r\xi \cos\theta + l \sin\theta_c \cos\phi \\ r\xi \sin\theta + l \sin\theta_c \sin\phi \end{pmatrix}$$

where l is length of the muon trajectory corresponding to the radius (line segment between P_0 and P) of the ring of the Čerenkov radiation striking the reflector at P and r is the radius of the reflector. The condition for P to be on the reflector is $|P| \leq r$. Therefore,

$$l = l(\xi) = \frac{r}{\sin\theta_c} \left[\sqrt{1 - \xi^2 \sin^2(\phi - \theta)} + \xi \cos(\phi - \theta) \right]$$

for the points at the edge of the reflector. The axes can always be oriented such that $\theta = 0$, in which case l becomes

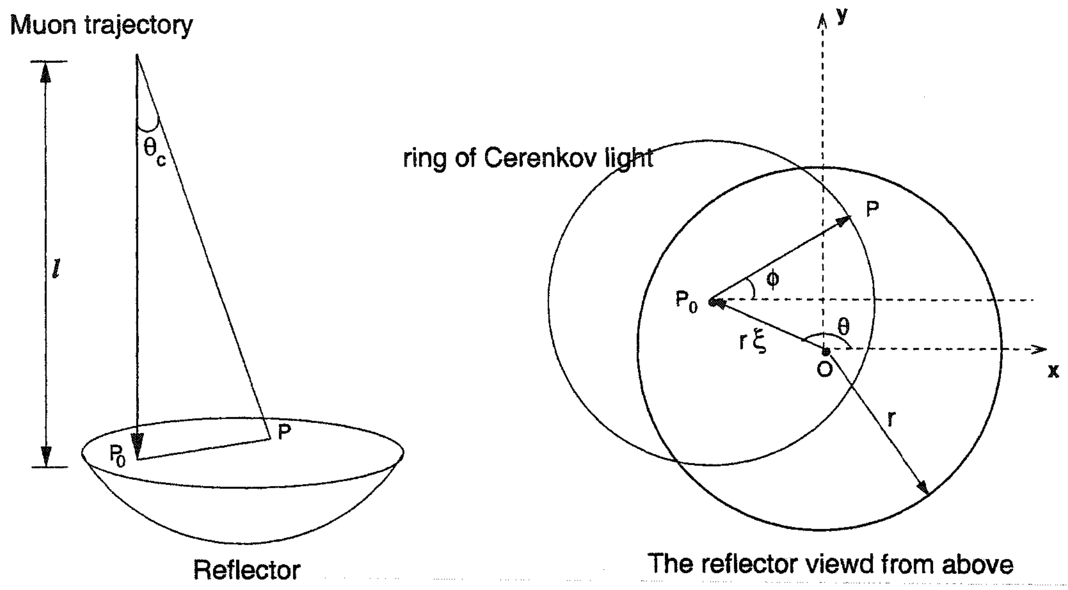

Figure 5.7. Definition of the coordinates chosen to describe a point on the reflector. The picture shows the case where the impact parameter $\xi < 1$. The definitions of coordinates are the same even for the case in which the impact point is outside of the reflector $\xi \geq 1$. θ_c is the Čerenkov angle.

$$l = l(\xi) = \frac{r}{\sin\theta_c}\left[\sqrt{1-\xi^2\sin^2\phi} + \xi\cos\phi\right]. \tag{5.14}$$

With equation 5.13, the number of photoelectrons q (called *charge* hereafter) per unit ϕ can be written as

$$\frac{dq}{d\phi} = \frac{U_0}{2\pi}\left[\sqrt{1-\xi^2\sin^2\phi} + \xi\cos\phi\right] \tag{5.15}$$

and the total charge,

$$q = \frac{U_0}{2\pi}\int_0^{2\pi}\left[\sqrt{1-\xi^2\sin^2\phi} + \xi\cos\phi\right] d\phi$$

$$
\begin{aligned}
&= \frac{U_0}{2\pi}\int_0^{2\pi}\sqrt{1-\xi^2\sin^2\phi}\,d\phi \\
&\equiv \frac{2U_0}{\pi}E(\xi) \qquad (5.16)
\end{aligned}
$$

here $E(\xi)$ is defined as

$$
E(\xi) \equiv \int_0^{\frac{\pi}{2}}\sqrt{1-\xi^2\sin^2\phi}\,d\phi.
$$

The next step is to calculate the image parameters, which are defined with dipole and quadrupole moment as described in Appendix A. As discussed above, ξ, θ_c, and U_0 are mapped into total charge, *Width* and *Length* (equation A.1, A.9, and A.8). To calculate these quantities, dipole and quadrupole moments need to be calculated (equation A.2 and A.3). The dipole moments per unit charge of the recorded muon image can be written as

$$
\begin{aligned}
\frac{d_x}{q} &= \frac{2U_0}{\pi q}\int_0^{2\pi}(\theta_x+\theta_c\cos\phi)\left[\sqrt{1-\xi^2\sin^2(\phi-f)}+\xi\cos(\phi-f)\right]d\phi \\
&= \frac{2U_0}{\pi q}\left(\theta_x E(\xi)+\theta_c\xi\pi\cos f\right) \\
&= \theta_x+\frac{\theta_c\xi\pi\cos f}{E(\xi)} \qquad (5.17) \\
\frac{d_y}{q} &= \theta_y+\frac{\theta_c\xi\pi\sin f}{E(\xi)} \qquad (5.18)
\end{aligned}
$$

where f is a factor relating to the choice of axes in mirror (position) space and camera (angular) space, which has no effect on the final *Width* and *Length*.

Quadrupole moments can be similarly obtained (equation A.3),

$$
Q_{xx} = \frac{2U_0}{\pi}\int_0^{2\pi}(\theta_x+\theta_c\cos\phi)^2\left[\sqrt{1-\xi^2\sin^2(\phi-f)}+\xi\cos(\phi-f)\right]d\phi
$$

$$
\begin{aligned}
&= \frac{2U_0}{\pi}\left[(\theta_x^2+\frac{\theta_c^2}{2})E(\xi)+\frac{\theta_c^2}{2}B(\xi)\cos(2f)+2\theta_x\theta_c\pi\xi\cos f\right] && (5.19)\\
Q_{yy} &= \frac{2U_0}{\pi}\left[(\theta_y^2+\frac{\theta_c^2}{2})E(\xi)-\frac{\theta_c^2}{2}B(\xi)\cos(2f)+2\theta_y\theta_c\pi\xi\sin f\right] && (5.20)\\
Q_{xy} &= \frac{2U_0}{\pi}\left[\theta_x\theta_y E(\xi)+\theta_x\theta_c\pi\xi\sin f+\theta_y\theta_c\pi\xi\cos f+\frac{\theta_c^2}{2}B(\xi)\sin(2f)\right] && (5.21)
\end{aligned}
$$

where

$$
B(\xi) = \int_0^{\frac{\pi}{2}} \cos(2\phi)\sqrt{1-\xi^2\sin^2\phi}\,d\phi. \tag{5.22}
$$

Now, let us define

$$
\begin{aligned}
F_0(\xi) &= 1-\left(\frac{\xi\pi}{4E}\right)^2 && (5.23)\\
F_1(\xi) &= \frac{B}{E}-\left(\frac{\xi\pi}{4E}\right)^2. && (5.24)
\end{aligned}
$$

From equation A.8 and A.9, we get

$$
\begin{aligned}
(Length)^2-(Width)^2 &= z\\
&= \theta_c^2 F_1(\xi) && (5.25)\\
(Length)^2+(Width)^2 &= \widetilde{Q}_{x_1x_1}+\widetilde{Q}_{x_2x_2}\\
&= \theta_c^2 F_0(\xi). && (5.26)
\end{aligned}
$$

The quantity $[(Length)^2-(Width)^2]/[(Length)^2+(Width)^2]$ is a function depending only on ξ, and ξ can be found numerically. Then, using the equation 5.16 for charge , the weighting factor U_0/θ_c, which is independent of θ_c, and ξ can be obtained for muon images.

5.2.3 Muon Images with $\xi > 1$

When the impact point is outside of the reflector, the muon path length corresponding to the received Čerenkov light by the reflector becomes

$$l = l(\xi) = \frac{2r}{\sin\theta_c}\sqrt{1-\xi^2\sin^2\phi}. \tag{5.27}$$

Therefore, the total charge is

$$\begin{aligned} q(\xi) &= \frac{U_0}{2\pi}\int_{-arcsin(1/\xi)}^{arcsin(1/\xi)} 2\sqrt{1-\xi^2\sin^2\phi d\phi} \\ &\equiv \frac{2U_0}{\pi}G(\xi) \end{aligned} \tag{5.28}$$

where $G(\xi)$ is defined as

$$G(\xi) \equiv \int_0^{arcsin(1/\xi)} \sqrt{1-\xi^2\sin^2\phi d\phi}.$$

Following a similar procedure to the case for $\xi < 1$, it can be shown that

$$(Length)^2 - (Width)^2 = \theta_c^2 H_1(\xi) \tag{5.29}$$

$$(Length)^2 + (Width)^2 = \theta_c^2 H_0(\xi) \tag{5.30}$$

where

$$H_0(\xi) = 1 - \left(\frac{\pi}{4\xi G}\right)^2 \tag{5.31}$$

$$H_1(\xi) = \frac{S(\xi)}{E} - \left(\frac{\pi}{4\xi G}\right)^2 \tag{5.32}$$

and

$$S(\xi) \equiv \int_0^{arcsin(1/\xi)} \cos(2\phi)\sqrt{1-\xi^2\sin^2\phi}d\phi.$$

These results are similar in form to the $\xi < 1$ case.

5.2.4 Simulated Muon Images

Complete ring muon images are simulated with energy from $\sim$ 5 GeV to $\sim$ 10 GeV. At the altitude of the Whipple 10-m telescope, 2.3 km, the minimum energy for a muon to produce Čerenkov radiation is $\sim$ 4.9 GeV. The radii for images (i.e., Čerenkov angle) of muons with energies greater than $\sim$ 10 GeV become larger than 1°, at which point these images are generally not contained by the Whipple camera (FOV $\sim$ 2.2°) without truncation (see Figure 5.8). Night sky background noise (NSB, discussed in sec 5.3.1) is inserted into the simulated muon data from typical real runs taken during the same period of time. Details of the event simulation are discussed in section 5.4.2.1.

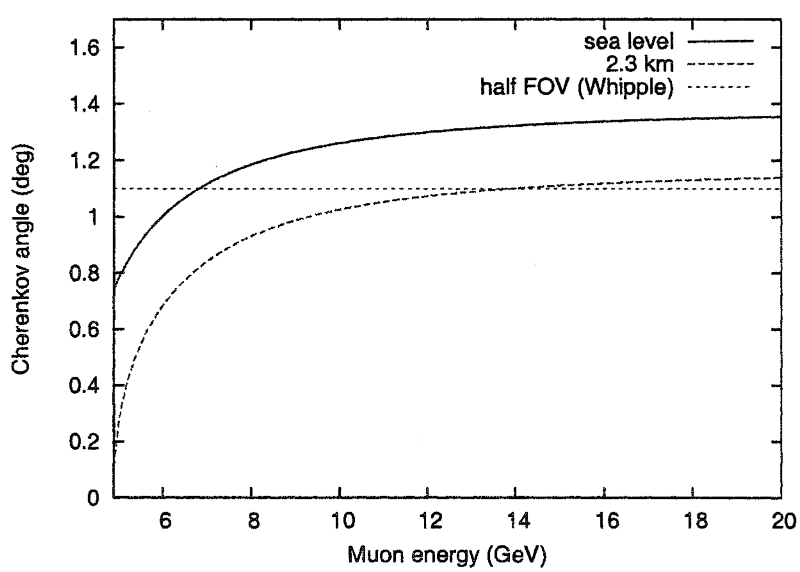

Figure 5.8. Čerenkov angle for muons at sea level and 2.3 km above sea level.

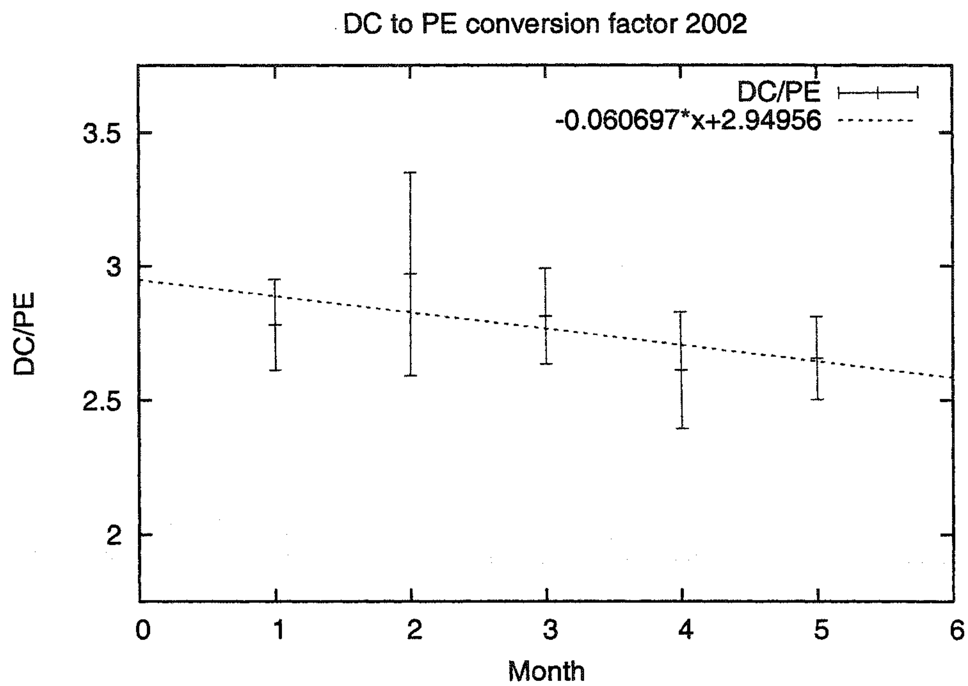

Figure 5.9. The "DC/PE conversion factor" in 2002 season.

5.2.5 Finding the DC/PE Conversion Factor

Complete muon rings are used to determine the conversion factor. Data are selected from the periods of December 2001 to May 2002. The distribution of the factor according to time is shown in Figure 5.9. Forty-four complete real muon ring images are used for the DC/PE conversion factor for the period of time. The mean value is 2.89 ± 0.26. The systematic decay error may be partially caused PMT degradation (see the fitted line in Figure 5.9).

5.3 Image Preparation

Before the events in the Whipple run data are analyzed, a set of image preparation procedures are applied. These procedures include pedestal removal, software flatfielding, and cleaning. After this, the images are parametrized. These image parameter values are stored to a MySQL database, for later reuse, if the data are revisited.

5.3.1 Night Sky Noise and Pixel Pedestal

Any data taken with an IACT, such as Whipple, are directly exposed to the night sky noise produced by fluctuations in the ambient photon field, which is present on even the darkest of nights. The number of PE recorded over the 20 ns integration window are distributed approximately as a Gaussian (see Figure 5.10). The PMT signals are AC coupled (constant component of current is removed) at the amplifiers (see Figure 1.13) to remove any low frequency noise before the trigger. Although the AC coupling removes the constant current attributed to the NSB, the statistical fluctuations about this mean current remain. In order to measure the negative fluctuations in the integrated charge, which would otherwise be impossible to digitize, a constant "pedestal" current is artificially injected into the signal. This permits 4 - 5 σ negative fluctuations in the NSB to be still recorded by the qADCs. Therefore, each event in the Whipple data contains this digitized integrated pedestal

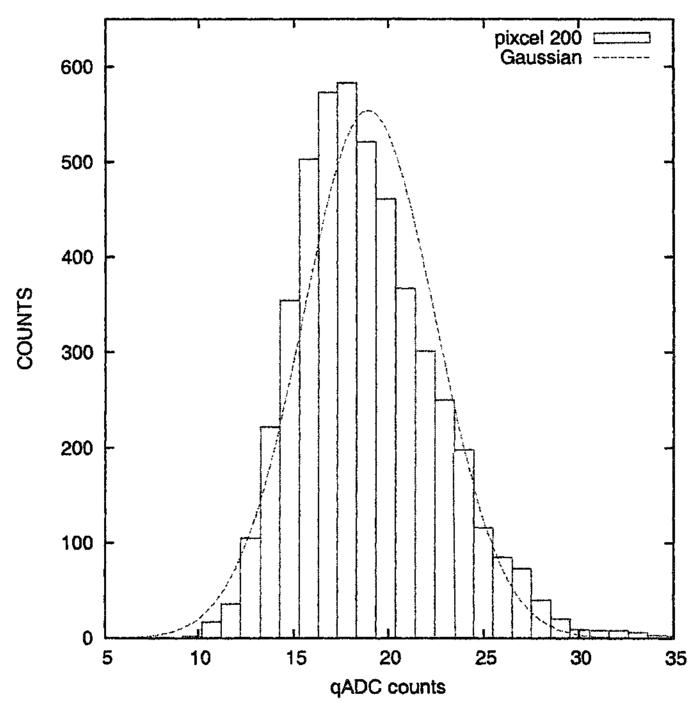

Figure 5.10. Typical night sky background histogram of 28 min exposure with Gaussian fit. The pedestal and NSB are determined by the mean of the Gaussian and the standard deviation respectively.

current as a component of the qADC values. These components must be removed in software at the image preparation stage. During normal Whipple runs, in addition to the standard trigger, the telescope is triggered artificially with rate of 1 Hz. A majority of these "pedestal" events contain only digitized NSB fluctuations (occasionally an air shower event will be present by chance). The digitized pedestal charge, or "pedestal value," is estimated for each channel by calculating the mean value recorded for these events. The variance provides an estimate of the mean NSB fluctuation. The pixel pedestal value and NSB for each channel are stored in a MySQL data base. The pedestal values are subtracted from the qADC values before events are flatfielded and cleaned.

5.3.2 Run File Padding

Even when the azimuth and elevation of the observed patches of the sky are the same, the sky brightness condition could be different between run files used in analysis as pairs (ON and dedicated OFF or ON and matching OFF run). This is especially the case when a dedicated OFF run is not available and a "matched" OFF run is used for analysis; due to the large time gap between runs, these can be large differences in the sky brightness condition. This difference in the sky brightness could introduce bias, distorting the images, when they are cleaned (section 5.3.3). To reduce this effect, NSB levels are compared between the two runs on a pixel-by-pixel basis. The pixel with less noise is "matched" with larger noise values. This matching is done by artificially adding extra noise to those channels (in either the ON run or the OFF run) with smaller noise. This process is called "Software Padding." The amount of the additional noise is determined as described in Cawley 1993 [110]. If $\hat{N}_l$ and $\hat{N}_s$ denote the level of noise in the larger and smaller of the pixel, the $\hat{N}_{add}$ is added to the smaller noise pixel for each event with $\hat{N}_{add}$ chosen as

$$\hat{N}_{add} = Gausse(0:1)\sqrt{\hat{N}_l^2 - \hat{N}_s^2} \tag{5.33}$$

here $Gausse(0:1)$ is a random number generated by Gaussian distribution with unit variance and zero mean.

If the noise levels differ, even by a moderate amount, a total number of CR background events which survive the analysis and cutting procedures could be systematically different in the ON and OFF runs without the proper padding. This could then result in a false signal and, possibly, a false detection claim.

5.3.3 Image Cleaning

AC coupling of the signals does not remove the fast fluctuation due to the NSB. Therefore, after the pedestal subtraction, the images contain noise fluctuations (see Figure 5.11). To minimize the effect of the NSB noise and enhance the Čerenkov light component in the images, a cut on the statistical significance of the signal in each channel is applied. This process is called "cleaning." After pedestal subtraction, the qADC values are kept in the image only if,

$$\begin{aligned} qADC - pedestal &\geqq 4.25\sigma_{NSB} \qquad (pixel) \\ &\geqq 2.25\sigma_{NSB} \qquad (boundary) \end{aligned}$$

where σ_{NSB} is NSB for the pixel. For paired analysis, this NSB should be the padded noise value.

5.3.4 Flatfielding of Channels in the Events

At the beginning of each observation season, flatfielding of the Whipple camera is performed as described in section 5.1. In addition, to minimize possible remaining discrepancy in pixel gains (caused by the PMT degradation, etc.), each run's data are also flat fielded for analysis. This is called "software flatfielding." The relative gain for each channel in a given run is calculated with the method described previously in section 5.1. To reduce statistical errors, the 10 nearest consecutive runs available (if not available, at least 4 nearest runs) are used to calculate the averaged relative gains. The relative gains from a given run and averaged gains ($\sim$ 10 runs) are stored in a MySQL database. After cleaning, the images are flat fielded with the average gains (i.e., each qADC value is multiplied by the relative gain for the pixel).

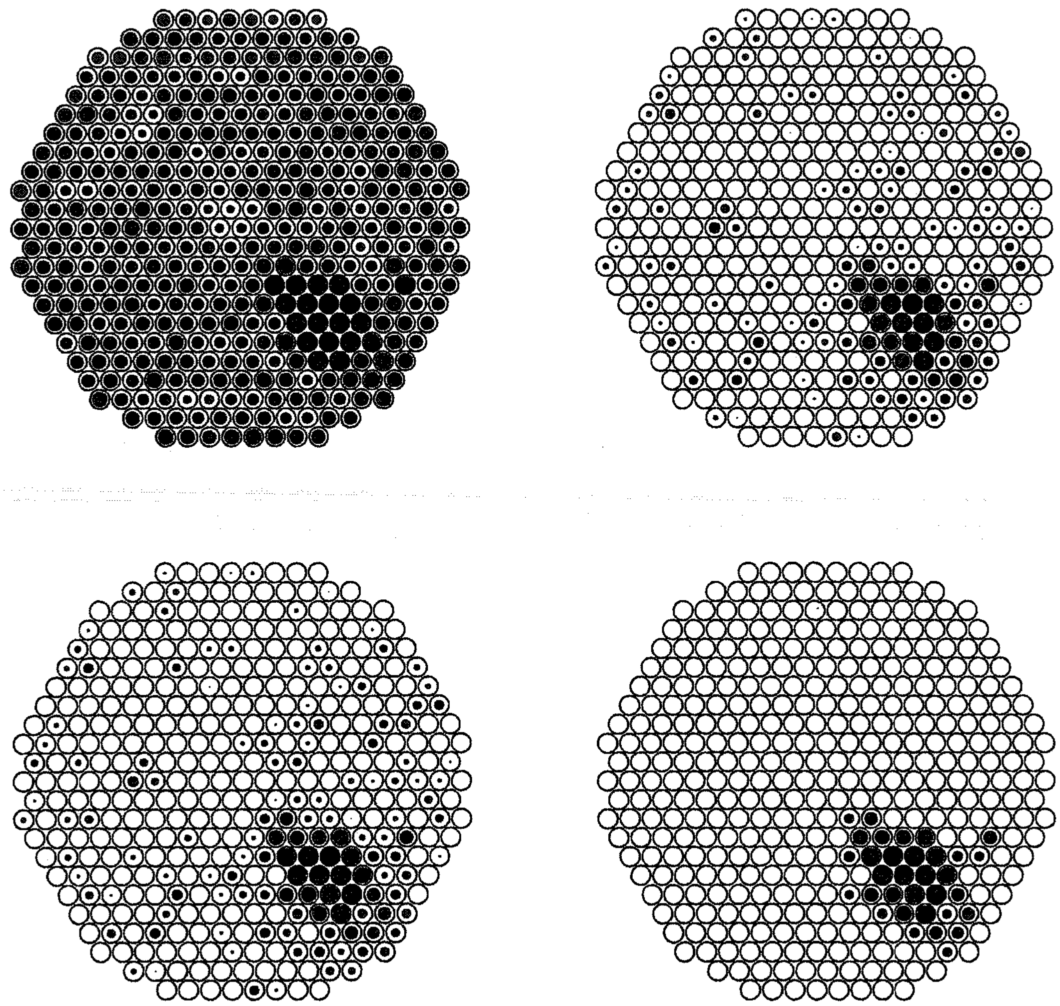

Figure 5.11. Example of gamma-ray image in different stage of data preparation process. Raw (top left), pedestal subtracted (top right), flat fielded (bottom left), and cleaned (bottom right) gamma-ray images

5.3.5 Image Parametrization

As described briefly in section 5.2.1, the cleaned images are parametrized by their dipole moments, quadrupole moments, and qADC charge counts. Figure 5.12 shows the definition of the parameters. The mathematical definitions are given in Appendix A.

For a single telescope, like the Whipple 10-m, an analysis based on the difference

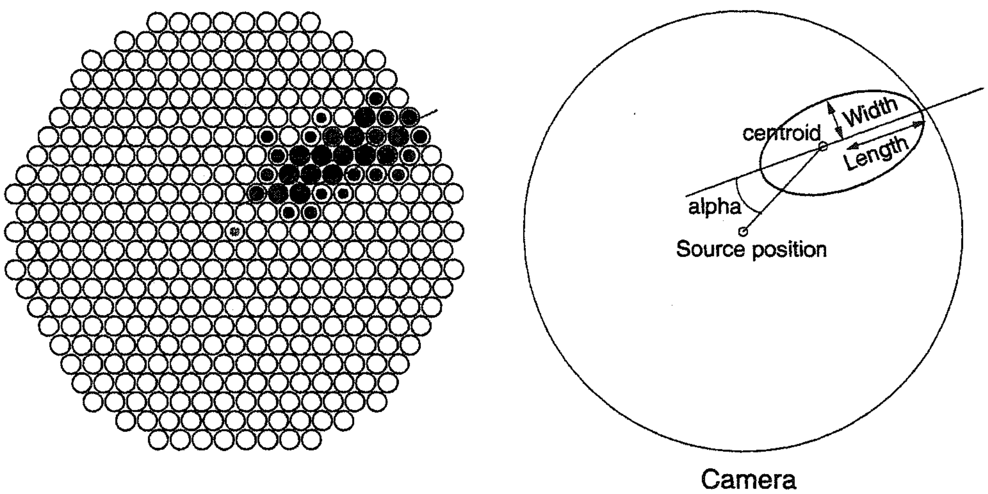

Figure 5.12. A real gamma-ray image and a schematic picture of image parameters

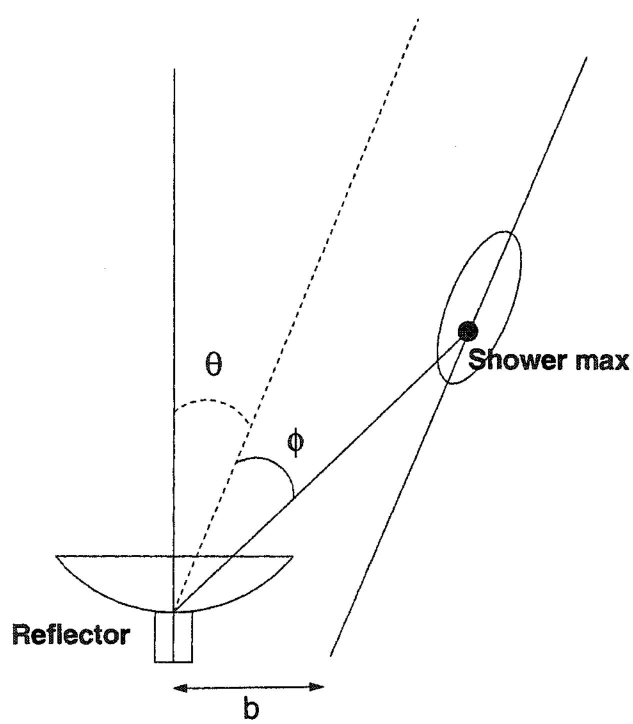

Figure 5.13. Quantities determine the image parameter "Distance." The dotted line is parallel to the trajectory of the particle.

in the dominant location in the image parameter hyper space is the most effective method to discriminate hadronic events from gamma-ray-like events. Differences in the EAS development for gamma-ray- and CR-initiated events, described in section 1.3.2, are manifested as differences in the image parameters. The gamma-ray images are basically elliptical in shape. The lateral spread of the EAS is characterized by the *Width* (equation A.9) and vertical development of the shower is characterized by the *Length* (equation A.8). Isotropy of the CR arrival direction is projected onto a spread in *Alpha* angle space. The *Distance* parameter encodes both the incident angle (θ in Figure 5.13), the impact parameter (b), and extra angle ϕ due to the impact parameter.

The statistical significance of gamma-ray detection is determined by finding excesses in gamma-ray-like events over the background CR events. Discrimination of images produced by gamma-ray-induced showers from those produced by background CRs is done by applying a set of cuts to the image parameters. Finding a set of cuts which maximize the signal to background ratio while minimizing the loss of signal is an important part of the analysis sequence.

5.4 Analysis Methods

Two different analysis methods were applied on the selected SBG data set. The first is the most standard analysis method used routinely to analyze Whipple data. The second is a new spectrum-dependent method. The standard analysis uses a set of cuts called "Supercuts2000," which is optimized to detect Crab-Nebula-like sources with a power spectral index of ~ 2.5; i.e.,

$$\frac{dF}{dE} \propto E^{-2.5}.$$

Although "Supercuts2000" has been used for most of the Whipple data sets, there is always the possibility that it can miss small gamma-ray signals submerged by overwhelming background events. It was not optimized to detect them. This could occur, for example, because the threshold energy of the instrument/analysis (the peak of energy sensitivity curve) is dependent on the power low spectral index of the sources. Since we do no have prior knowledge of the spectrum of potential sources at GeV - TeV energies, an analysis method has been developed which accounts for the potentially different spectral index utilizing the multidimensional maximal likelihood method (MLM).

5.4.1 Supercuts2000 and the Crab Nebula

Supercuts2000 consists of the following set of cuts on the image parameters:

$$
\begin{aligned}
0.13^\circ < LENGTH &< 0.25^\circ \\
0.05^\circ < WIDTH &< 0.12^\circ \\
0.4^\circ < DISTANCE &< 1.0^\circ \\
ALPHA &< 15^\circ
\end{aligned}
$$

We also make the following cut to reduce the background of partial muon events,

$$\frac{LENGTH}{SIZE} < 0.0004.$$

The cuts on parameter values are all given in degrees. This set of cuts is derived to maximize the statistical signal significance from the Crab Nebula, which is known to have a differential spectra index ~ 2.5 (section 1.1.2). Supercuts2000 efficiently removes $\sim 98\%$ of the background CR events and leaves $\sim 50\%$ of the gamma-ray-like events.

Figure 5.14 shows results of 25 ON/OFF pairs of Crab Nebula runs analyzed with Supercuts2000. The plot is a histogram of events which passed the cuts. The horizontal axis is the *Alpha* angle; the vertical axis is the number of events. An excess can clearly be seen in the number of events with $Alpha \leq 15^\circ$. For this kind of pair analysis, the gamma-ray rate is simply given by

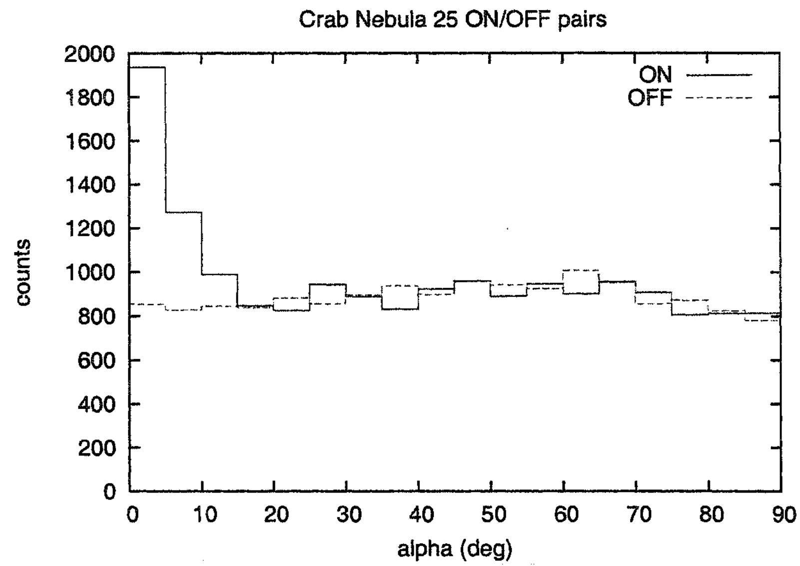

Figure 5.14. Crab Nebula alpha plot with Supercuts2000. The signal excess in this plot shows 21.2 σ significance.

$$R_\gamma = \frac{N_{ON} - N_{OFF}}{time} \tag{5.34}$$

where N_{ON} and N_{OFF} are the number of events which passed the cut from ON and OFF runs (corresponding to the first three *Alpha* bins in the plot 5.14). The occurrence of CR and gamma-ray events is a Poisson process. Assuming N_{ON} and N_{OFF} are much larger than one, their distributions become Gaussian and the corresponding variance is

$$\begin{aligned} \Delta N_{ON} &\simeq \sqrt{N_{ON}} \\ \Delta N_{OFF} &\simeq \sqrt{N_{OFF}}. \end{aligned} \tag{5.35}$$

The signal significance is defined as

$$\sigma = \frac{R_\gamma}{\Delta R_\gamma}. \tag{5.36}$$

Using simple error propagation, the statistical significance becomes

$$\sigma = \frac{N_{ON} - N_{OFF}}{\sqrt{N_{ON} + N_{OFF}}}. \tag{5.37}$$

For analysis involving TRK runs or ON runs without OFF runs, the background rate is estimated from the number of events in the α-histogram with $20° < \alpha < 65°$. This number is scaled using the "*Tracking ratio*," which is calculated using many OFF runs in the season. The rate of excess gamma-ray events is given by

$$R_\gamma = \frac{N_{ON} - r \times N_{20°-65°}}{time}. \tag{5.38}$$

The tracking ratio r is determined by the ratio of OFF run events with *Alpha* between 20° and 65° "CR background" region to events with *Alpha* between 0° and 15° "signal" region. An example of a combined OFF run alpha plot in shown in Figure 5.15. From this plot, the calculated tracking ratio is

$$\begin{aligned} r \pm \Delta r &= \frac{N_{0°-15°}}{N_{20°-65°}} \pm \Delta r \\ &= 0.304 \pm 0.002 \end{aligned}$$

where $N_{20°-65°}$ and $N_{0°-15°}$ are the number of events with *Alpha* between 20° and 65° and events with *Alpha* between 0° and 15°, respectively. The significance is given (under the Gaussian assumption) by error propagation as

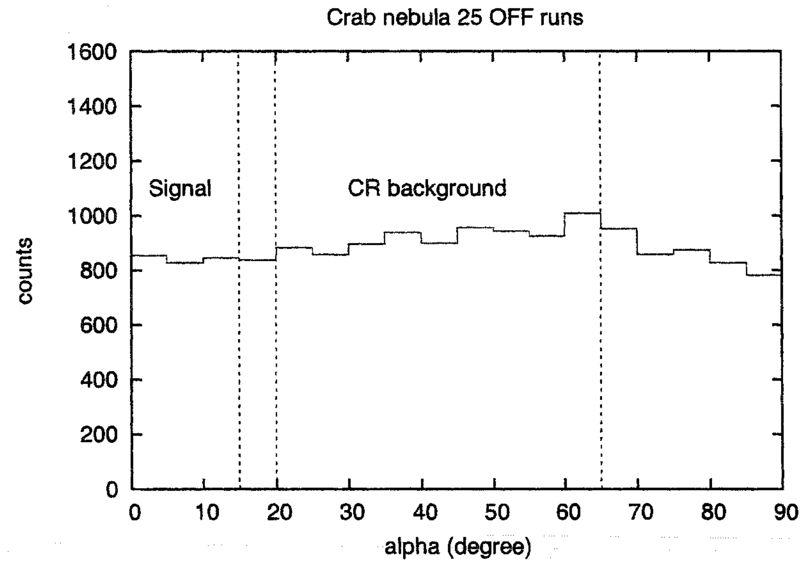

Figure 5.15. Combined Crab Nebula OFF alpha plot with Supercuts2000. Calculated tracking ratio is 0.304±0.002.

$$\sigma = \frac{N_{0^\circ-15^\circ} - r(N_{20^\circ-65^\circ})}{\sqrt{N_{0^\circ-15^\circ} + r^2(N_{20^\circ-65^\circ}) + (\Delta r)^2(N_{20^\circ-65^\circ})^2}}. \tag{5.39}$$

With this method, the significance for the combined Crab Nebula data (the same data set used for Figure 5.14) is 24.0 (compared to 21.2 from ON/OFF analysis).

Since N_{ON} and N_{OFF} are directly proportional to exposure time, signal significance is proportional to $\sqrt{time}$. Customarily, an observation which results in $\sigma \geq 5$ is claimed as statistically meaningful detection.

As was previously mentioned, the energy at which the telescope system is most sensitive (often called *energy threshold* or *peak energy*) is strongly dependent on the energy spectrum of the source . For example, the Whipple telescope has an energy threshold for the Crab-Nebula-like source (index $\sim$ 2.5) with Supercuts2000, at approximately 400 GeV. For sources whose spectrum is unknown, it is possible that Supercuts2000 will fail to detect their signal. Hence, a new system of optimizing cuts with any given spectrum was developed.

5.4.2 MLM Method

A new analysis which can be applied to sources with any spectral index has been developed and used to analyze the observations of the selected SBGs (Chapter 3). A large part of the designing and coding of this method was done by Vladimir Vassiliev (UCLA) and Jeter Hall (University of Utah). The goal was to develop an automated system to both define cuts for sources with any spectrum and avoid the tuning of these cuts by hand. Moreover, it is capable of finding optimized sets of cuts which have more complicated shapes in the chosen parameter space (or phase space). Supercuts2000 can be considered a multidimensional BOX-type cut in five-dimensional phase space. The MLM method can produce an optimized set of cuts which have more complicated hyperspatial geometry. The parameters we utilize for our analysis are *(Distance)*^{2}, *Length, Width, log(Size), Length/Size,* and *Alpha.* The optimized set of cuts are derived with simulated gamma-ray events and real background OFF data for given spectral index. After that, the cuts are applied to real ON and OFF data to find the signal significance as described above.

5.4.2.1 Simulated Gamma-ray Event Preparation

Simulated gamma-ray events or muon events (section 5.2.4) are generated using three steps; shower simulation, weighting due to main optical reflectivity, and electronics, with given parameters, namely, initial particle energy, incident zenith angle, and impact parameter. Phenomena that occur in the atmosphere, including EAS, Čerenkov radiation, and also attenuation by the air, are simulated by KASCADE code [111]. The virtual Čerenkov photons generated are then weighted due to the Whipple optical reflectivity. The weighting factor is calculated as follows. First, 70% of the incoming photons are reflected by the main reflector. The lightcone efficiency is estimated as 26%. Assuming a photon that hits the photocathode of a PMT has a 100% chance of being detected, the total detecting efficiency of the camera is 56% due to the total area of the lightcone and reflectivity on the surface of the PMTs. As a consequence, $0.7 \times 0.56 = 0.39$ is the weighting factor. The photons which passed these steps are then fed into the Whipple hardware (chain of electronics gains) simulation codes and the final events are generated. A large number of simulated events with various incident energies and zenith angles are pregenerated and stored for analysis. The energy resolution of the simulated event energy is four bins per decade. Pixel noise is added to the events by padding with selected real runs.

5.4.2.2 Determination of Spectral Index Dependent Cuts

The first step in the determination of the cuts is to inject OFF events into a multidimensional histogram. A set of cuts is formed by performing an optimized integration over the volume of hyper space in this histogram. The number of OFF events is scaled by the total ON data exposure to be analyzed. The multidimensional boxes or "cells" with OFF event counts less than two are removed from further analysis at this point to avoid false detection by poor statistics. Then, properly padded gamma-ray events simulated in small energy bins (four bins per decade in photon energy) are injected into the histogram as well to create an "artificial ON" event set. The rate at which the signal is injected from each energy bin is determined by a power law spectrum with a chosen power index. If the multidimensional cells of the histogram are labeled with the index j, then the total number of injected gamma-ray events can be written as

$$\begin{aligned} g &= \sum_j g_j \\ &= \sum_j \sum_i f_0 \left\{ \frac{E_i}{E_0} \right\}^{-\gamma} \end{aligned} \tag{5.40}$$

where E_i and E_0 are the center values of the i_{th} energy bin and reference energy respectively and f_0 is the overall injection strength, which is tuned in such a way that the recovered signal significance becomes equivalent to the Crab Nebula flux at 1 TeV.

The probability of finding the event count C_j in the j_{th} cell with the OFF event count K_j^{off} is determined by the Poisson distribution. Assuming there are no real gamma-ray events in the corresponding artificial ON data, the probability is given by

$$L_j(C_j) = e^{-b_j}\left\{\frac{b_j^{K_j^{off}}}{K_j^{off}!}\right\}e^{-\alpha b_j}\left\{\frac{\alpha b_j^{C_j}}{C_j!}\right\} \tag{5.41}$$

where b_j is background event count, and α is a ratio between ON and OFF exposure.

$$\alpha = \frac{time_{ON}}{time_{OFF}}.$$

The log of total likelihood is the summation over an integration volume,

$$\begin{aligned} ln(L_{f_\gamma=0}) &= \sum_j L_j(C_j) \\ &= \sum_j \{-b_j + K_j^{off} ln(b_j) - ln(\Gamma(K_j^{off}+1))\} + \\ &\quad + \sum_j \{-\alpha b_j + C_j ln(\alpha b_j) - ln(\Gamma(C_j+1))\} \end{aligned} \tag{5.42}$$

where $ln(N!) = \Gamma(N+1)$, and Γ is the Gamma function. From the condition of likelihood maximization,

$$\frac{\partial ln(L_{f_0=0})}{\partial b_j} = 0$$

we have

$$b_j = \frac{K_j^{off} + C_j}{1+\alpha}.$$

If, however, there is a gamma-ray source present (real or injected), whose signal strength, f_γ, is unknown, then the likelihood must be modified, such that the probability of detecting C_j ON events and K_j^{off} OFF events is

$$\begin{aligned} ln(L_{f_\gamma \neq 0}) &= \sum_j \{ - \tilde{b}_j + K_j^{off} ln(\tilde{b}_j) - ln(\Gamma(K_j^{off} + 1)) \} + \\ &+ \sum_j \{ - (\alpha \tilde{b}_j + f_\gamma g_j) + C_j ln(\alpha \tilde{b}_j + f_\gamma g_j) - \\ &- ln(\Gamma(C_j + 1)) \}. \end{aligned} \tag{5.43}$$

Similarly, from the condition of likelihood maximization,

$$\frac{\partial ln(L_{f_\gamma \neq 0})}{\partial \tilde{b}_j} = 0.$$

Thus we have

$$\tilde{b}_j = \frac{1}{2}\Big\{ \frac{K_j^{off} + C_j}{1+\alpha} - f_\gamma \frac{g_j}{\alpha} \Big\} + \sqrt{\frac{1}{4}\Big\{ \frac{K_j^{off} + C_j}{1+\alpha} - f_\gamma \frac{g_j}{\alpha} \Big\}^2 + f_\gamma \frac{K_j^{off} g_j}{\alpha(1+\alpha)}}.$$

Now, we calculate the ratio between two likelihoods ($\equiv \lambda$). With equation 5.43 and equation 5.42, λ can be written as

$$\begin{aligned} \lambda &\equiv ln\left(\frac{L_{f_\gamma \neq 0}}{L_{f_\gamma = 0}} \right) \\ &= \sum_j \Big\{ - (1+\alpha)(\tilde{b}_j(f_\gamma) - b_j) - f_\gamma g_j + \\ &+ K_j^{off} ln\left(\frac{\tilde{b}_j(f_\gamma)}{b_j} \right) + C_j ln\left(\frac{\tilde{b}_j(f_\gamma)}{b_j} + f_\gamma \frac{g_j}{\alpha b_j} \right) \Big\}. \end{aligned} \tag{5.44}$$

According to Wilks theorem (see, for example, [112]), $2ln(\lambda)$ asymptotically follows a χ^2 distribution with r degrees of freedom. In this case, $r = 1$, since f_γ is the only parameter involved; thus,

$$2ln(\lambda) \sim \chi^2(1).$$

If the "ON" data set is an artificial ON run, then it peaks at the actual value of injected strength $f_\gamma = f_0$. Let us denote the j_{th} component of the above summation as LR_j. The last step is to determine a lower limit $\equiv L_0$ on the set of LR_j. The cells which have $LR_j > L_0$ then form a hyperspace in the histogram. The hyperspace determines the integration volume or, equivalently, the desired set of cuts. L_0 is determined in such way that the integration volume produces maximum total signal significance (as described in the previous section) with the OFF and artificially created ON run events. The signal significance in the case of real data is calculated by applying this set of cuts to the OFF and real ON runs.

This method has been tested successfully with the Crab Nebula. Alpha plots of the Crab Nebula using the MLM method with five different spectral indices are shown in Figure 5.16 - 5.20. The data set used is the same as the one in the standard analysis with Supercuts2000 (Figure 5.14). Twenty-five ON and 25 OFF (11.7 hours each) runs are combined. The simulated gamma-ray events are padded using one of the runs used in the set.

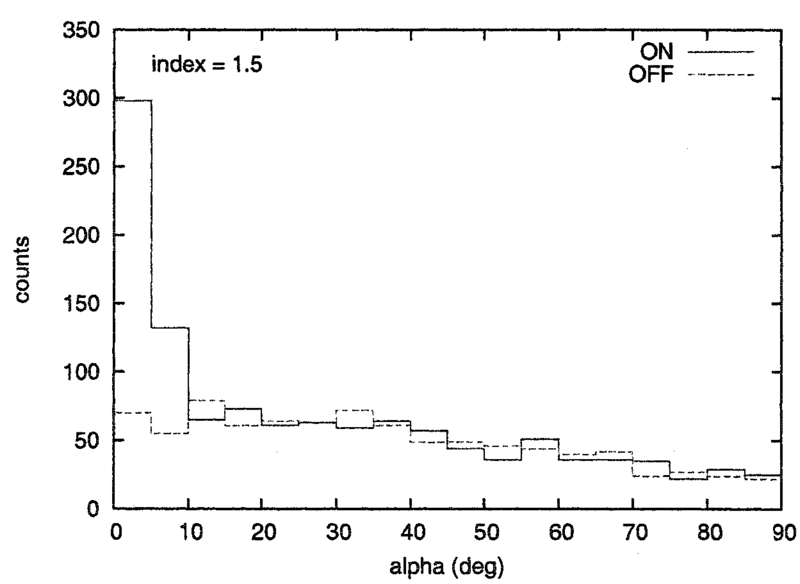

Figure 5.16. Crab alpha plot with the MLM method with given spectral index 1.5. Statistical significance is $\sigma = 11.15$.

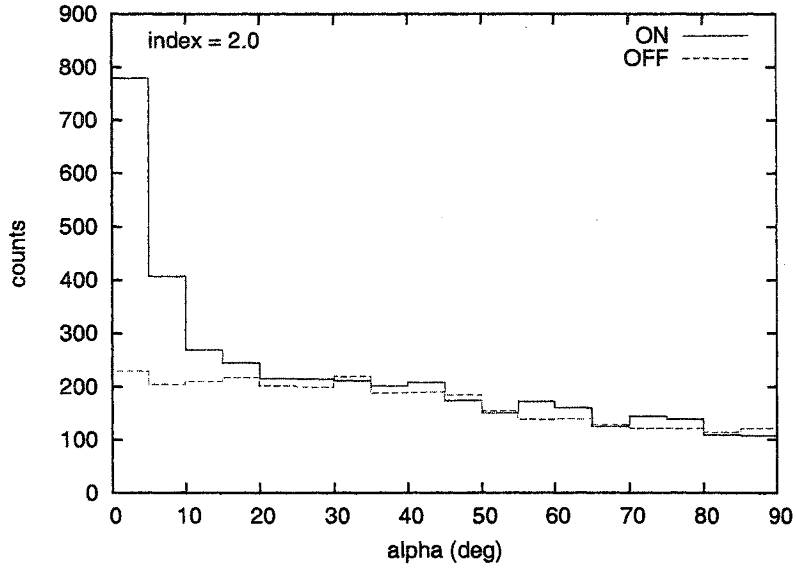

Figure 5.17. Crab alpha plot with the MLM method with given spectral index 2.0. Statistical significance is $\sigma = 17.9$.

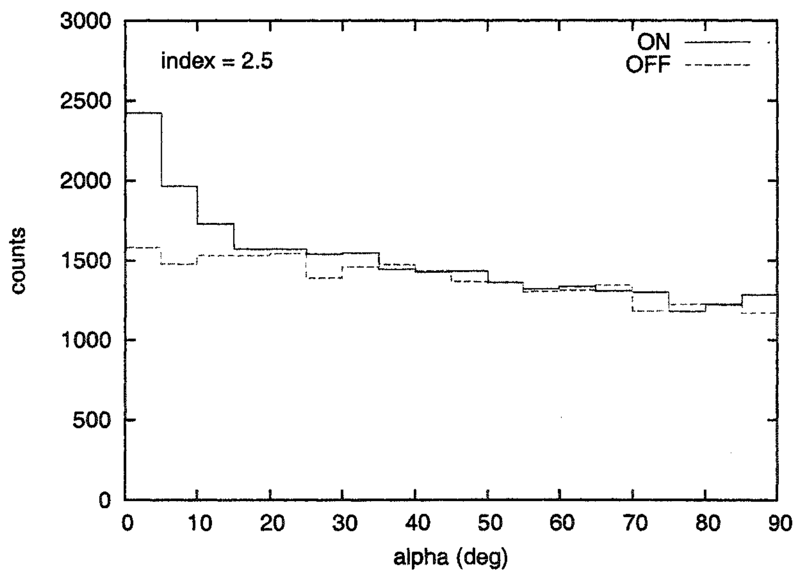

Figure 5.18. Crab alpha plot with the MLM method with given spectral index 2.5. Statistical significance is $\sigma = 14.7$.

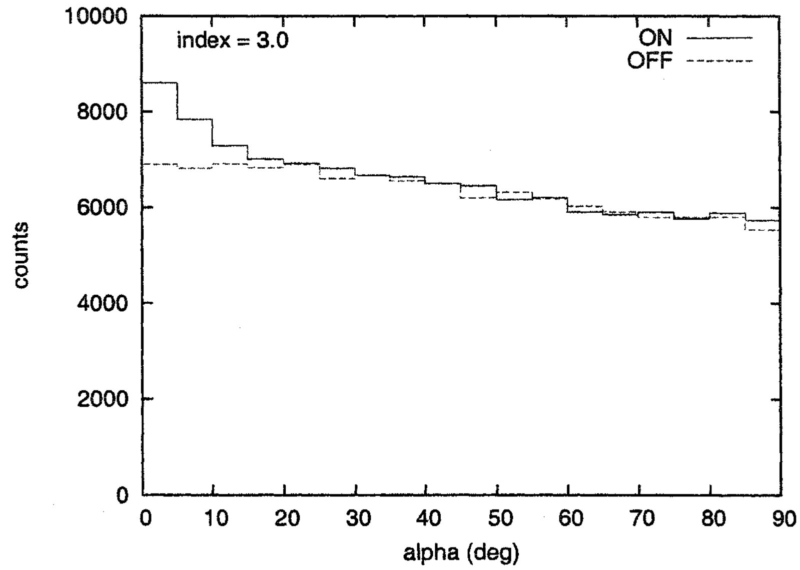

Figure 5.19. Crab alpha plot with the MLM method with given spectral index 3.0. Statistical significance is $\sigma = 14.7$.

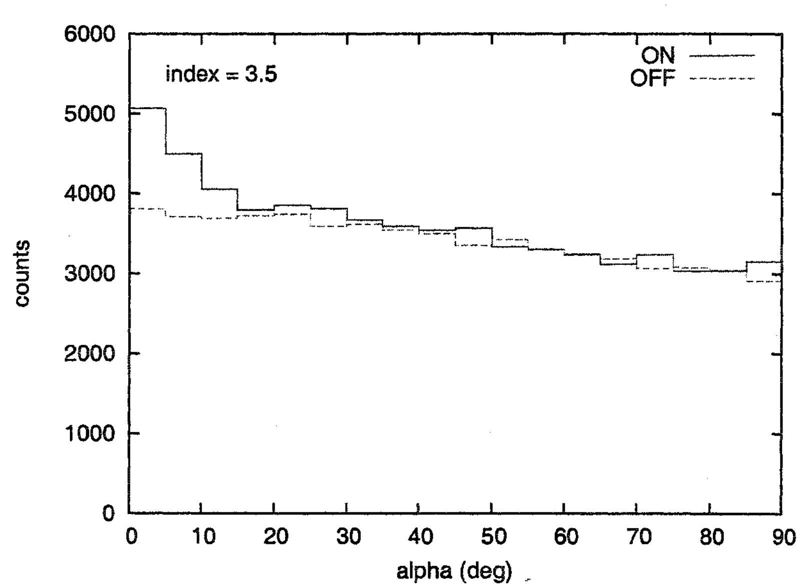

Figure 5.20. Crab alpha plot with the MLM method with given spectral index 3.5. Statistical significance is $\sigma = 12.4$.

CHAPTER 6

RESULTS AND DISCUSSION

Neither the standard nor the MLM method resulted in a detection of any of the selected sources ($> 3\sigma$, see Table 6.1). The possibilities of a power law spectra with indices of 2.0, 2.5, 3.0, and 3.5 were investigated with the MLM method for IC342. The MLM technique was also applied to M81 data set; however, the result of the MLM method with index 2.0 is not presented because the number of events which passed the cuts was not sufficient for a statistically significant estimate of the gamma-ray excess. This is a consequence of systematic errors in background evaluation and a lack of OFF data exposure. Alpha plots for IC342 and M81 obtained with the standard and the MLM methods are shown in Figure 6.1 through 6.15.

Upper limits on the flux at the 95% confidence level were derived for bins equally spaced in log energy. The Crab Nebula spectrum [13] is shown in the figure for comparison.

Table 6.1. Signal significances for the selected SBGs in units of σ.

Spectral index Sources	2.0	2.5	3.0	3.5
IC342 (MLM)	0.283	0.44	0.62	1.43
IC342 (SC2000)	–	-0.28	–	–
NGC3079 (SC2000)	–	1.77	–	–
M81 (MLM)	–	-0.24	-1.41	-1.15
M81 (SC2000)	–	0.21	–	–
M82 (SC2000)	–	-0.033	–	–

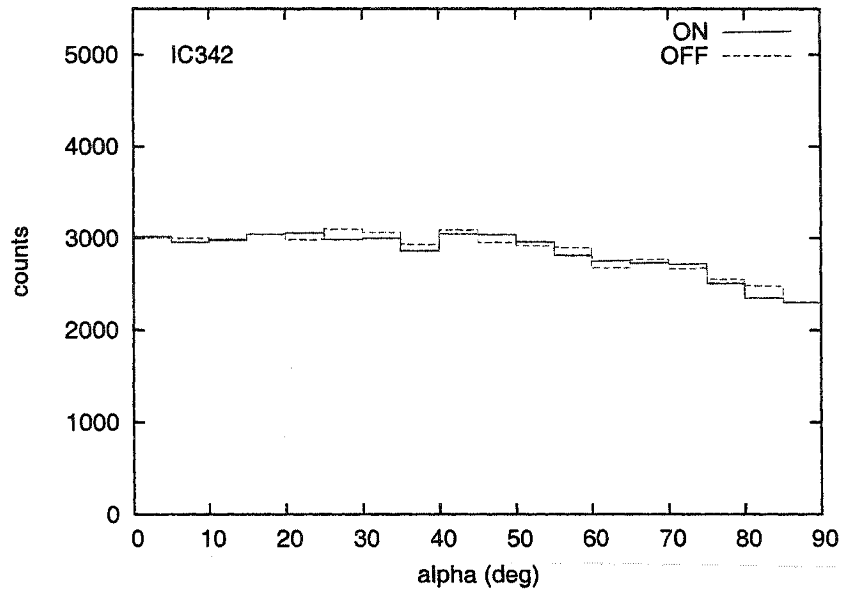

Figure 6.1. IC342 alpha plot obtained with Supercuts2000. The statistical significance of detection is $\sigma = -0.28$.

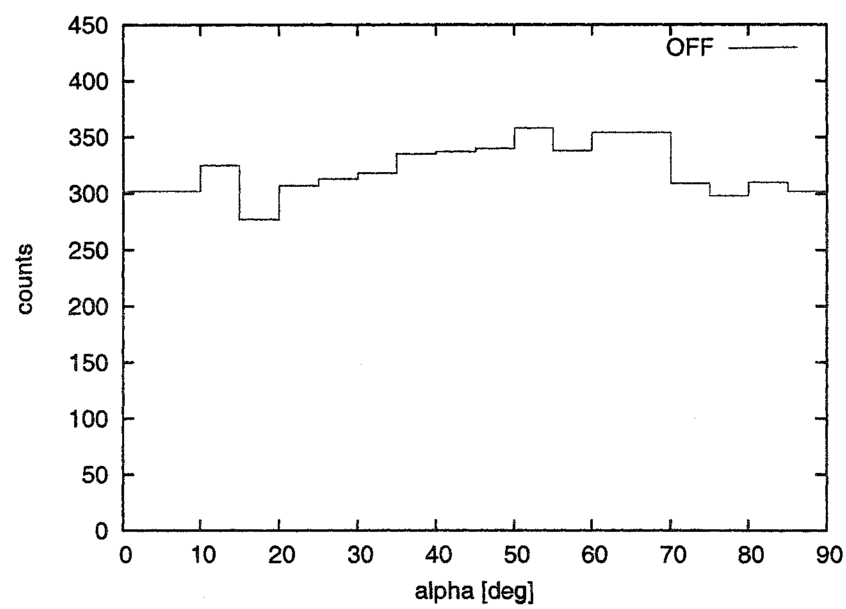

Figure 6.2. Alpha plot of NGC3079 OFF runs obtained with Supercuts2000. The tracking ratio determined from this data set is 0.31 ± 0.01.

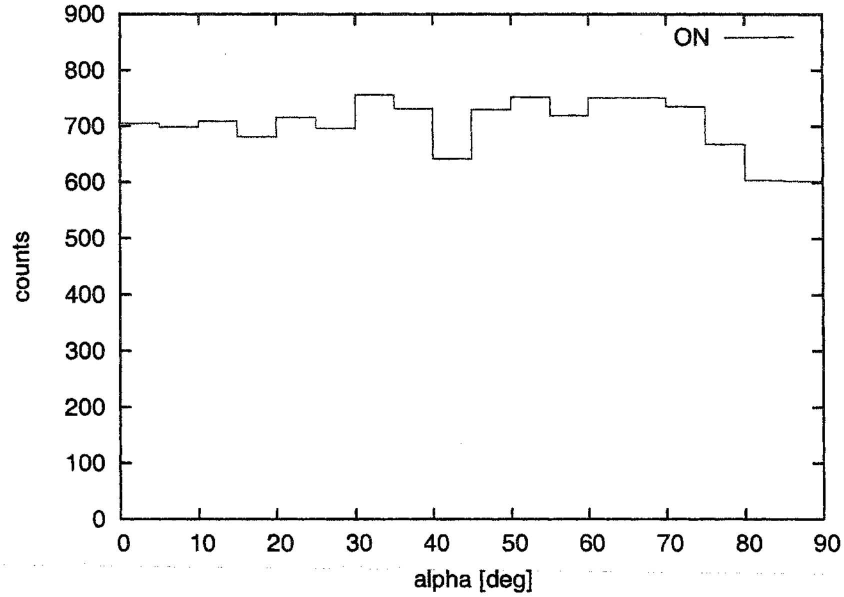

Figure 6.3. Alpha plot of NGC3079 ON runs obtained with Supercuts2000. The statistical significance is $\sigma = 1.93$.

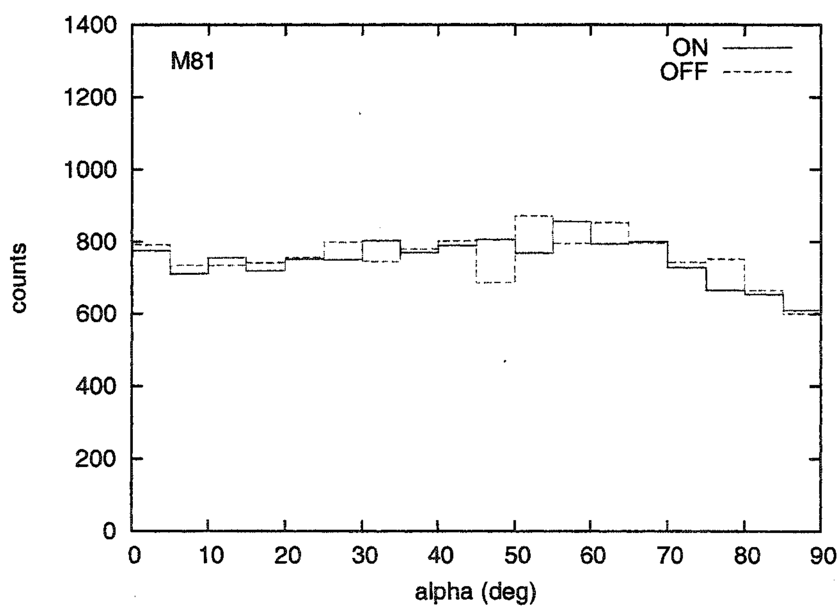

Figure 6.4. M81 alpha plot obtained with Supercuts2000. The statistical significance is $\sigma = -0.21$.

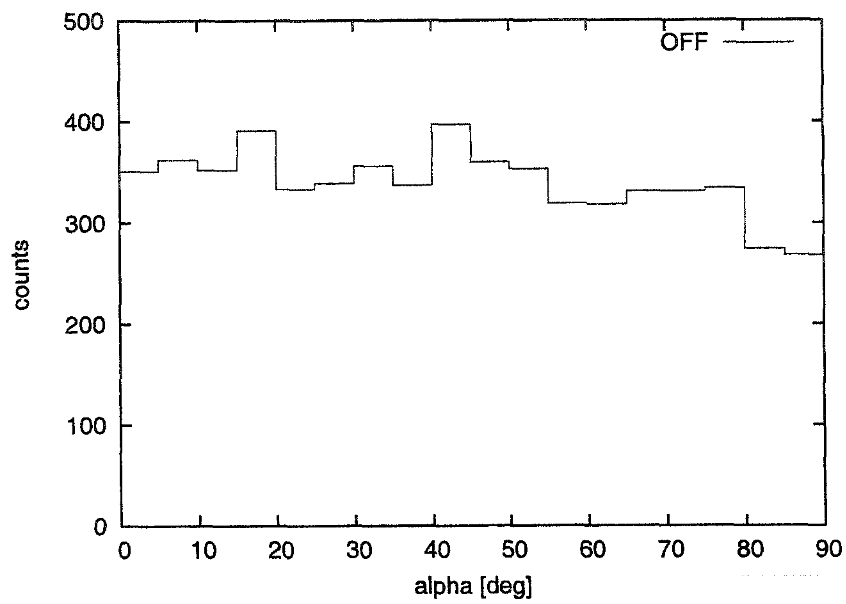

Figure 6.5. Alpha plot of M82 OFF runs in 2001 - 2002 season obtained with Supercuts2000. The tracking ratio determined from this data set is 0.34 ± 0.01

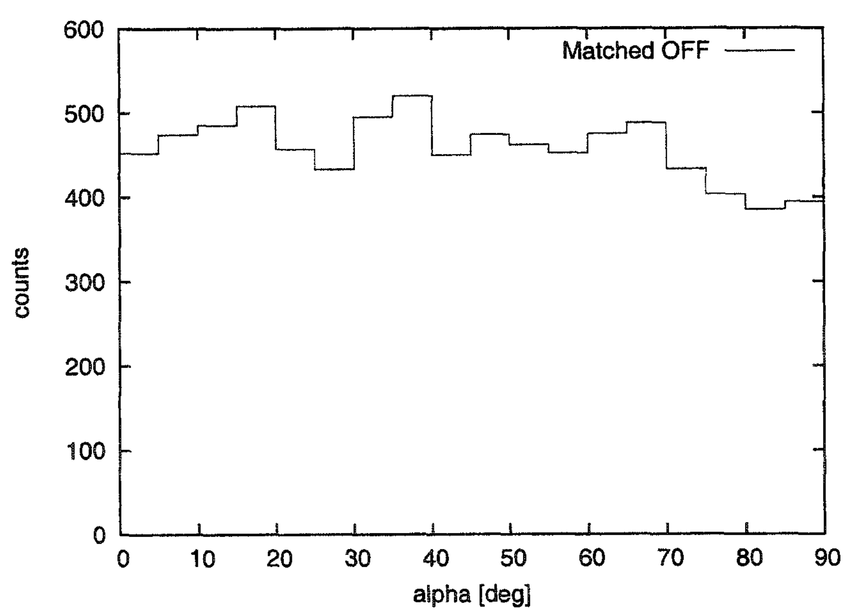

Figure 6.6. Alpha plot of "matched" OFF runs for M82 data in 2002 - 2003 season obtained with Supercuts2000. The tracking ratio determined from this data set is 0.33 ± 0.01

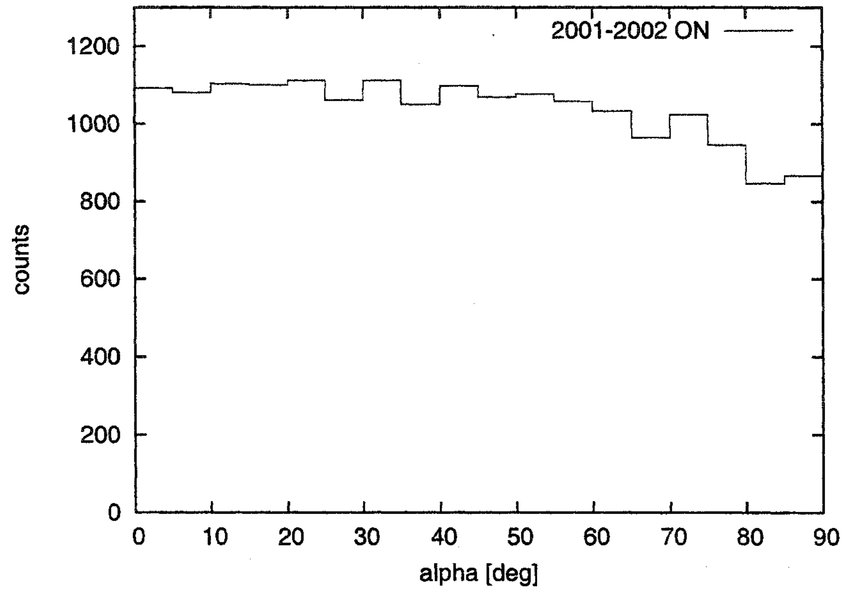

Figure 6.7. Alpha plot of M82 ON runs in 2001 - 2002 utilizing Supercuts2000. The statistical significance of detection is $\sigma = -0.17$ (tracking ratio = 0.34).

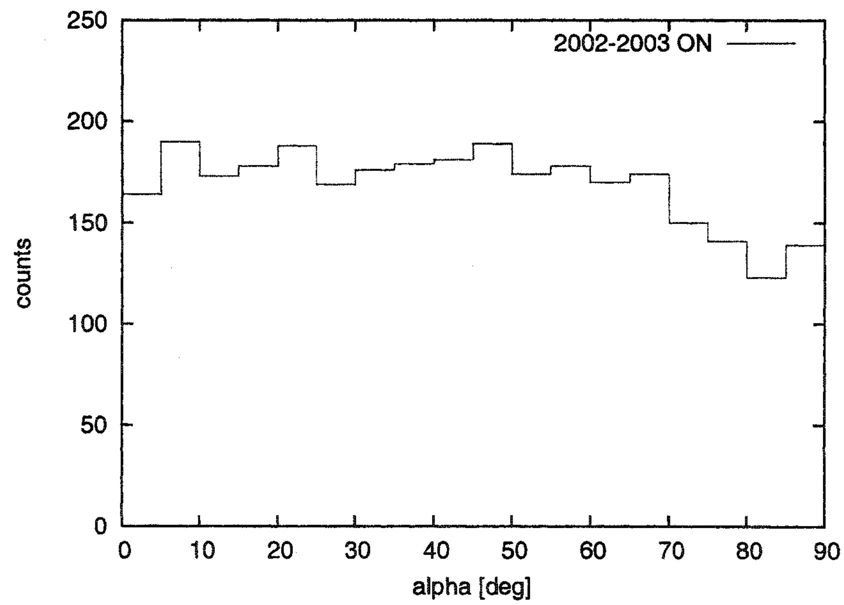

Figure 6.8. Alpha plot of M82 ON runs in 2002 - 2003 utilizing Supercuts2000. The statistical significance of detection is $\sigma = -0.088$ (tracking ratio = 0.33).

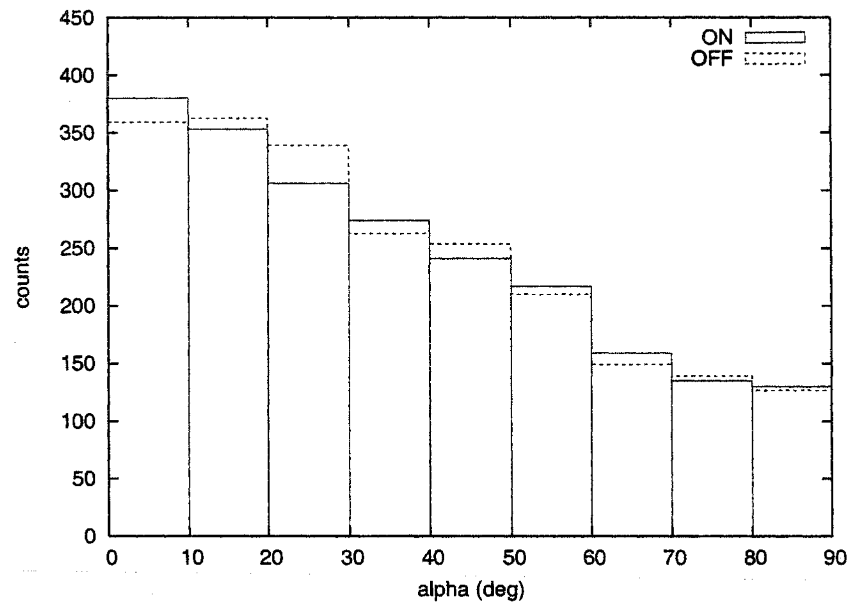

Figure 6.9. IC342 alpha plot utilizing MLM method with spectral index 2.0. The statistical significance of detection is $\sigma = 0.283$.

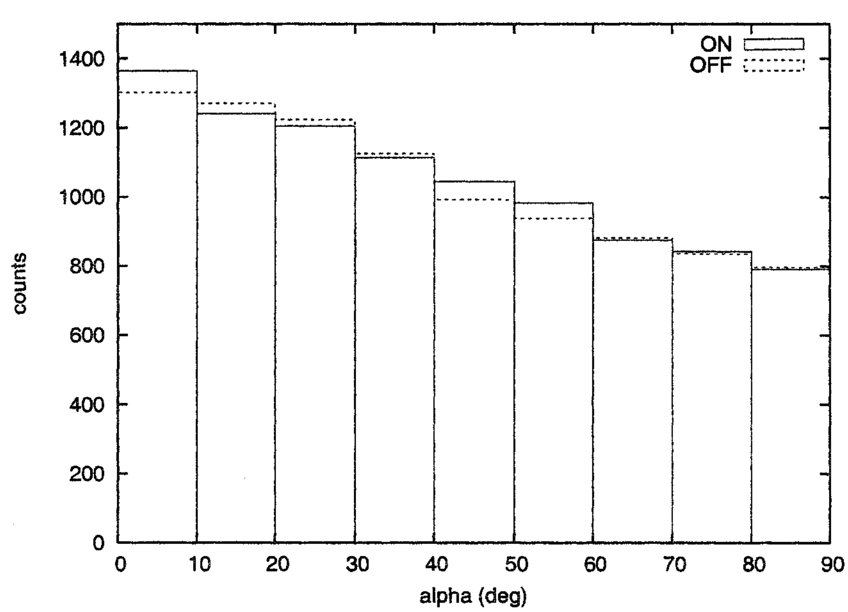

Figure 6.10. IC342 alpha plot utilizing MLM method with spectral index 2.5. The statistical significance of detection is $\sigma = 0.44$.

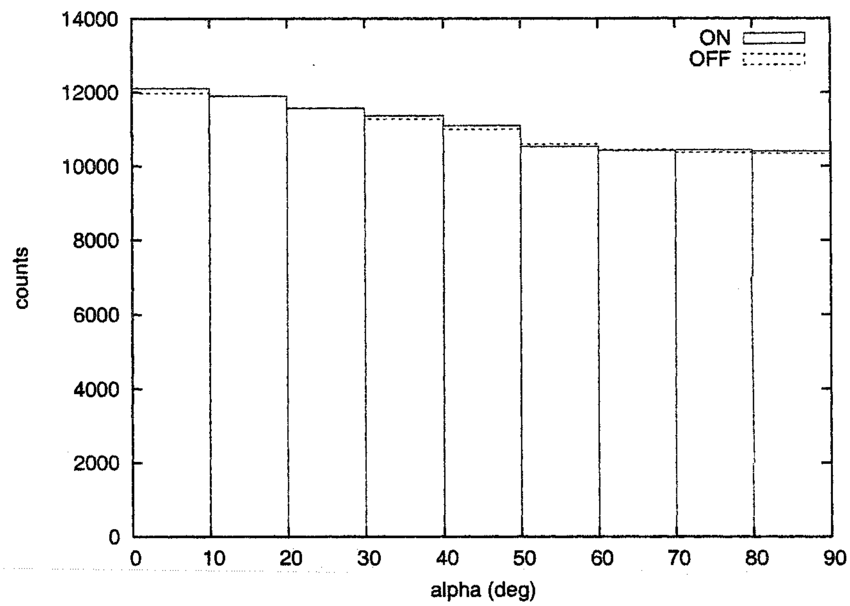

Figure 6.11. IC342 alpha plot utilizing MLM method with spectral index 3.0. The statistical significance of detection is $\sigma = 0.62$.

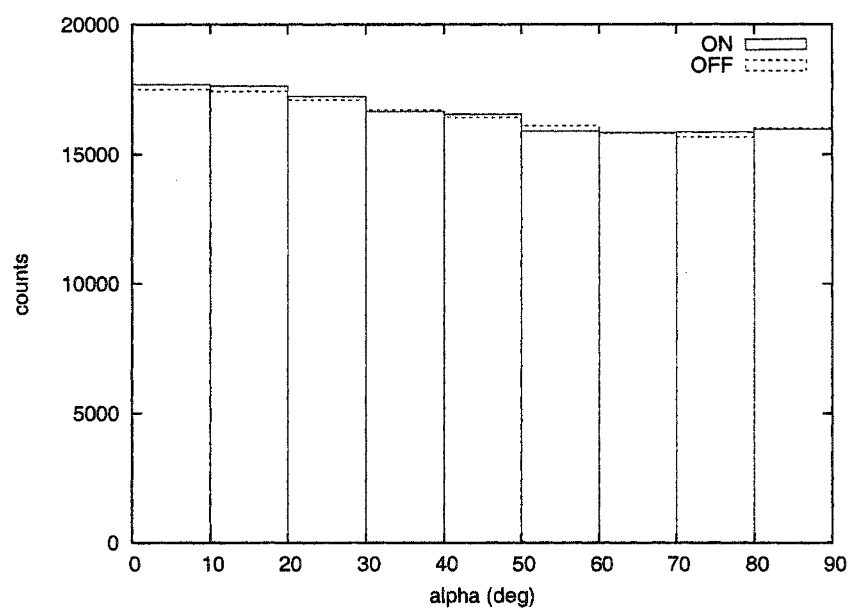

Figure 6.12. IC342 alpha plot utilizing MLM method with spectral index 3.5. The statistical significance of detection is $\sigma = 1.43$.

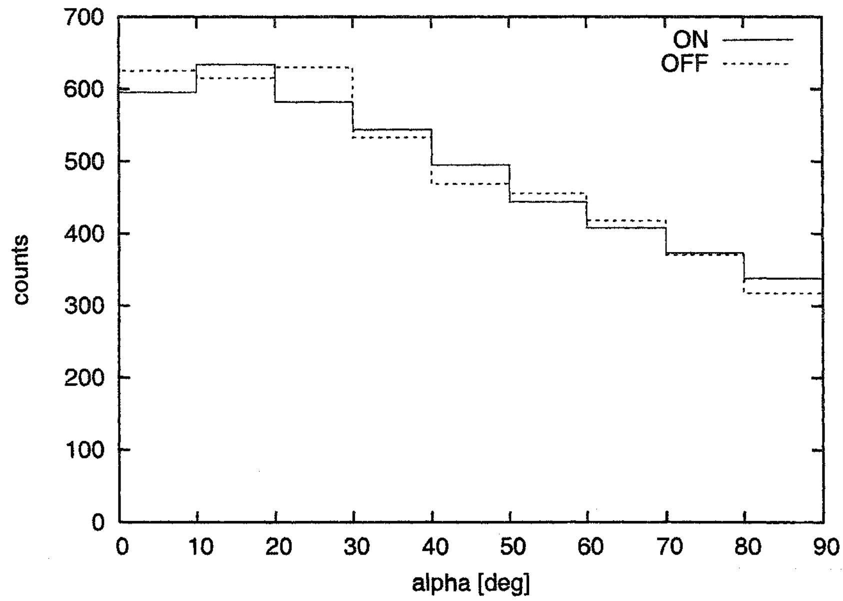

Figure 6.13. M81 alpha plot derived with MLM method with spectral index 2.5. The statistical significance of detection is $\sigma = -0.24$.

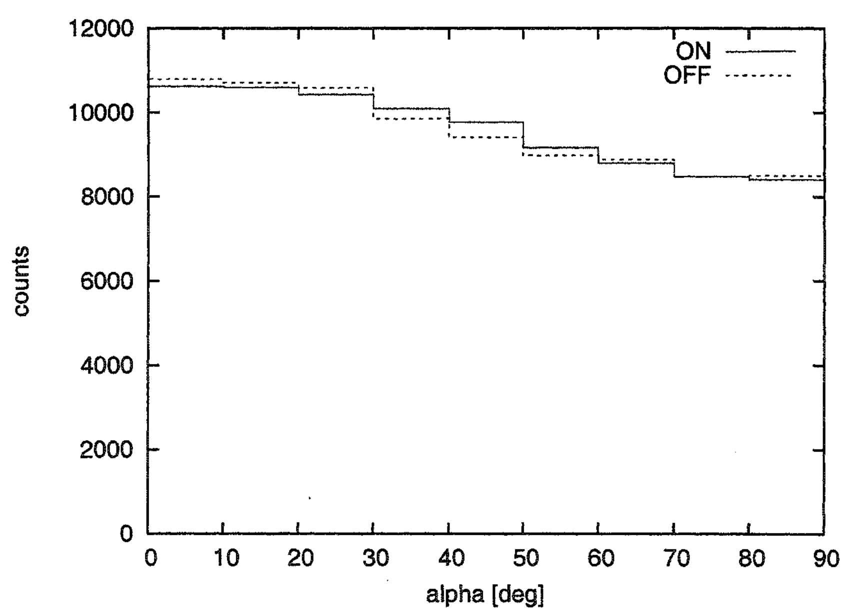

Figure 6.14. M81 alpha plot derived with MLM method with spectral index 3.0. The statistical significance of detection is $\sigma = -1.41$.

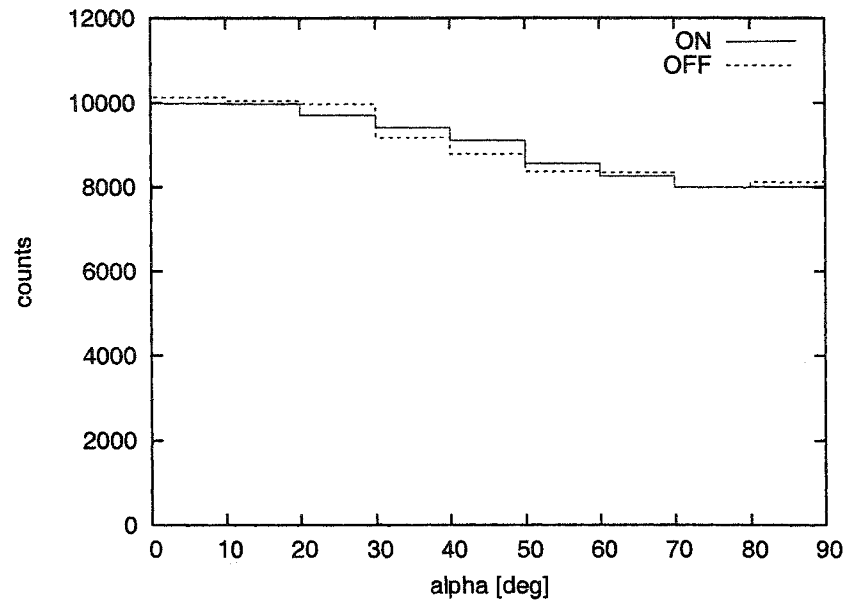

Figure 6.15. M81 alpha plot derived with MLM method with spectral index 3.5. The statistical significance of detection is $\sigma = -1.15$.

6.1 Flux Upper Limits Derivation

Upper limits on the flux, at the 95% confidence level, are calculated with the method described in Helene 1983 [113]. Given a probability density function $g(a)$, the probability of obtaining a value a greater than A purely by chance is

$$\lambda = \int_A^\infty g(a)da \tag{6.1}$$

If C and B denote the number of ON and OFF events which pass a set of cuts respectively, and the probability density is derived from Poisson distribution where N_0 is normalization constant, then

$$g(a) = N_0 \frac{e^{-(a+B)}(a+B)^C}{C!} \tag{6.2}$$

The upper limit on the number of signal counts, A, is found by setting a confidence level λ. For example, "95% confidence level" corresponds to $\lambda = 0.05$. The procedure is performed for event energy bin centered at $\bar{E}$ to find $A(\bar{E})$

$$A(\bar{E}) \geq \bar{E}\frac{dF(\bar{E})}{dE}\pi R^2(\bar{E})S_r(\bar{E})\frac{\Delta E}{\bar{E}}, \tag{6.3}$$

which limits $dF(\bar{E})/dE$, the differential flux of gamma rays at $\bar{E}$. $\pi R^2(\bar{E})$ is the sampling area for simulated gamma rays, and $S_r(\bar{E})$ is the fraction of simulated gamma rays which pass the cuts, i.e.,

$$S_r(\bar{E}) = \frac{N_{out}(\bar{E})}{N_{in}(\bar{E})} \tag{6.4}$$

where $N_{in}(\bar{E})$ is the number of simulated gamma-ray events with energy $\bar{E}$ generated, and $N_{out}(\bar{E})$ is the number of simulated gamma-ray events which are detected and pass the cuts. Therefore, the flux upper limit can be obtained from $A(\bar{E})$ as

$$\bar{E}^2\frac{dF(\bar{E})}{dE} \leq \frac{A(\bar{E})}{\pi R^2(\bar{E})S_r(\bar{E})}\frac{\bar{E}^2}{\Delta E} \tag{6.5}$$

For data sets which have enough OFF runs to be used with the MLM method, the upper limits are calculated in energy bins with the width $\Delta E/E = 0.43$. Four simulation energy bins are included for each bin in the MLM method. The upper limits are derived at $\sim$ 1 TeV for the rest of the sources. Table 6.2 shows the derived upper limits (see Figure 6.16 for the superimposed upper limits plot).

6.2 Interpretation and Future

The upper limits which we derived based on the available exposure for the selected SBGs constrain only the extreme predictions of the SNR hadronic CR

Table 6.2. Flux upper limits in units of [erg cm^{-2} s^{-1}]. The top row shows the energy center value in TeV.

Bin center energy (TeV)	0.125	0.221	0.393	0.698	1.24	2.21	3.92	6.98
IC342	3.95e-10	7.73e-11	3.82e-11	3.35e-11	1.7e-11	8.76e-12	2.1e-11	1.67e-11
M81	1.99e-10	5.89e-11	7.35e-11	3.59e-11	2.78e-11	3.2e-11	3.91e-11	4.8e-11
M82 (at 1TeV)					4.75e-11			
NGC3079 (at 1TeV)					4.1e-11			

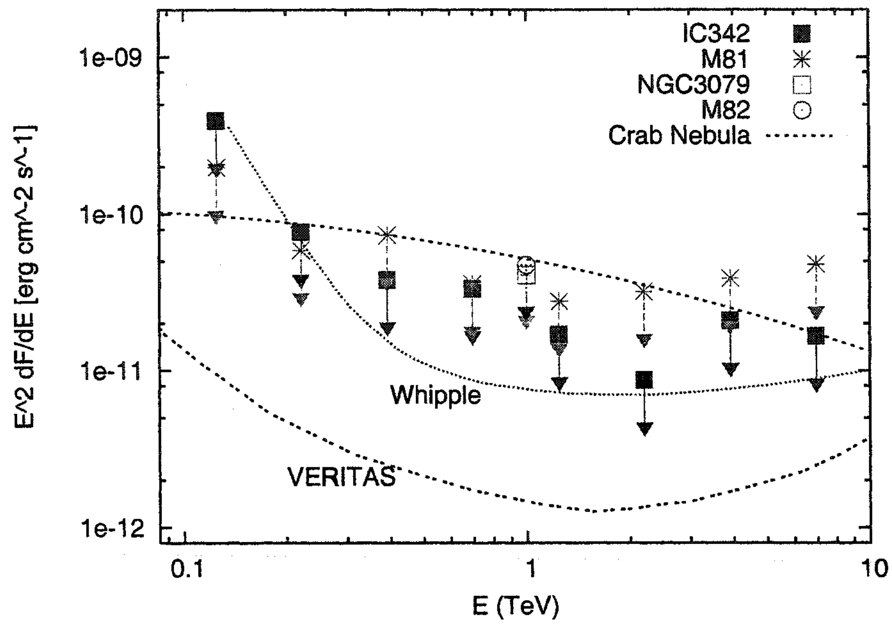

Figure 6.16. Gamma-ray flux upper limits for IC342, M81, M82 and NGC3079.

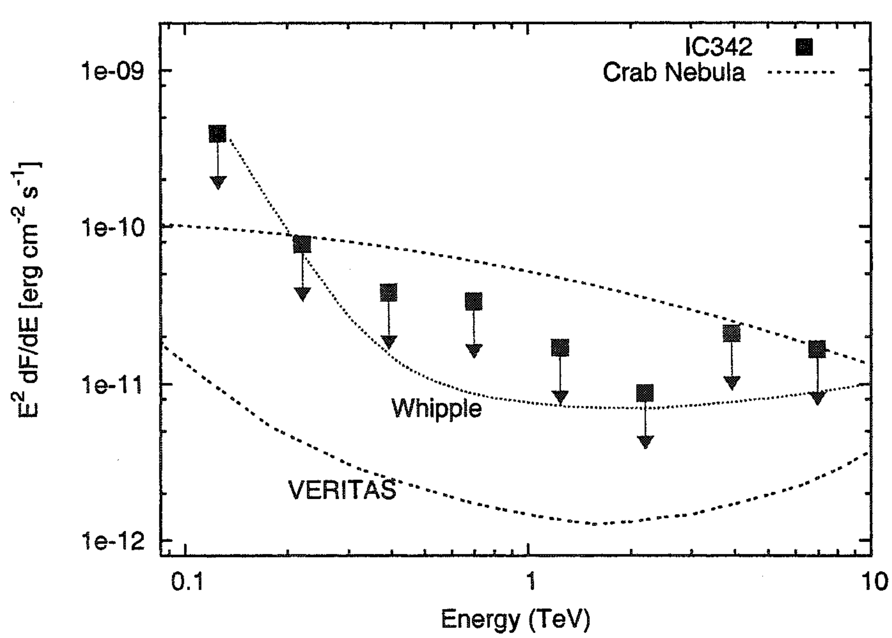

Figure 6.17. Gamma-ray flux upper limits for IC342.

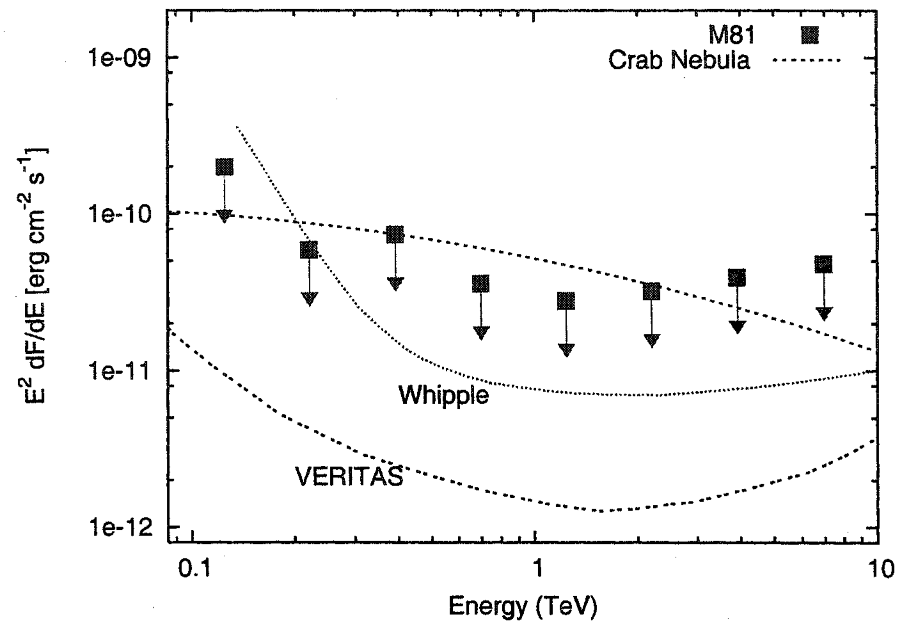

Figure 6.18. Gamma-ray flux upper limits for M81.

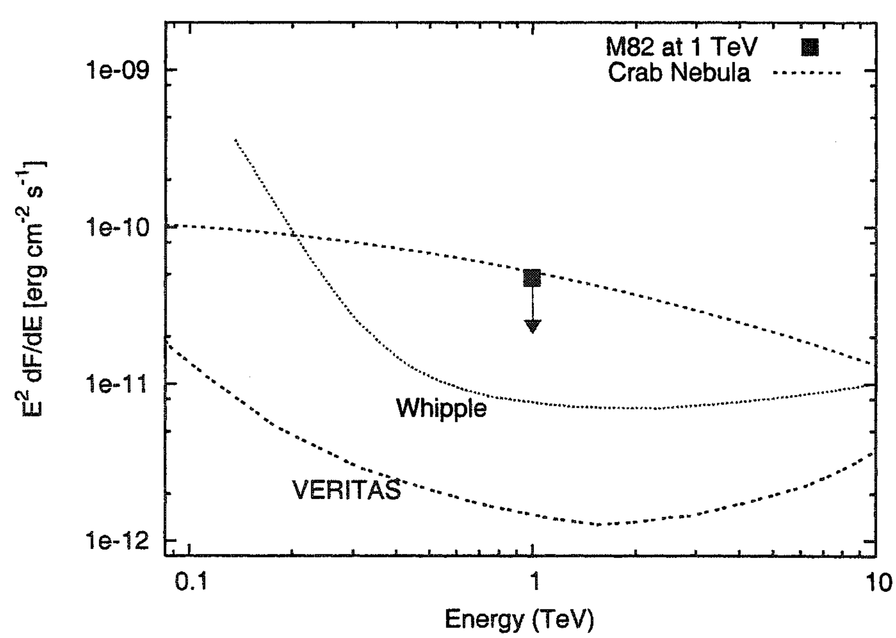

Figure 6.19. Gamma-ray flux upper limit for M82.

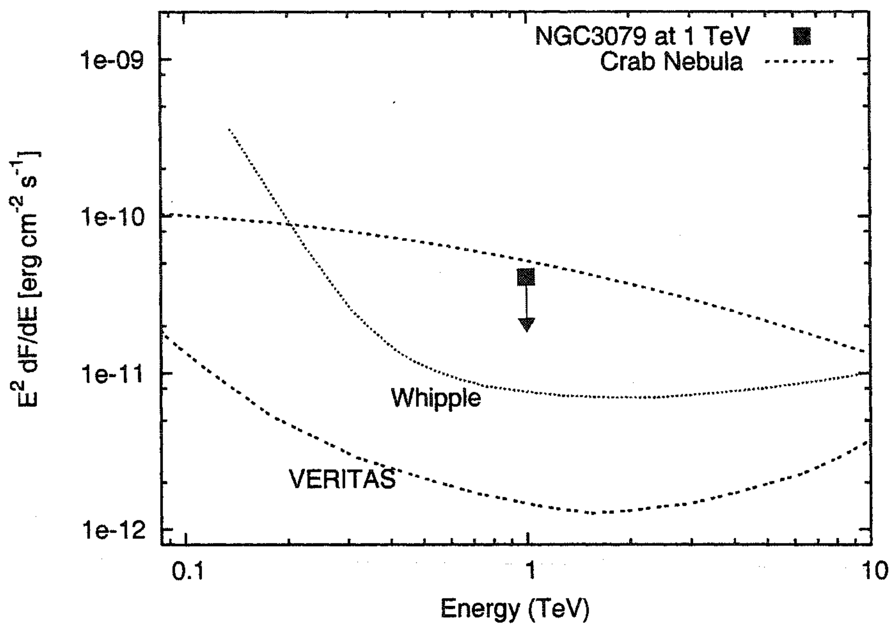

Figure 6.20. Gamma-ray flux upper limit for NGC3079.

acceleration scenario. As shown in Figure 3.3, the results are consistent with the flux estimate for M82, NGC3079, and IC342. The estimates show that it is possible to detect those sources and perhaps Arp220 in 50-hour exposure with a next-generation IACT instrument, such as, VERITAS.

We have discussed the possibilities of VHE gamma-ray emission from SBGs only in terms of hadronic CR interaction in dense gas environments. Including the report on detection of NGC253 [79], gamma-ray emission scenarios based on CR leptonic component, such as the IC mechanism, also have been discussed [114] [115] in publications. For M82, integrated VHE gamma-ray flux predicted [115] is above sensitivities of current IACTs (see Figure 6.21). This encourages future observation of SBGs as potential VHE gamma-ray emitters.

6.2.1 VERITAS

VERITAS is an array of four 12-m diameter telescopes, which is being constructed at Horseshoe Canyon on Kitt Peak, Arizona. The array system has many advantages over a single telescope instrument, the most important of which is the

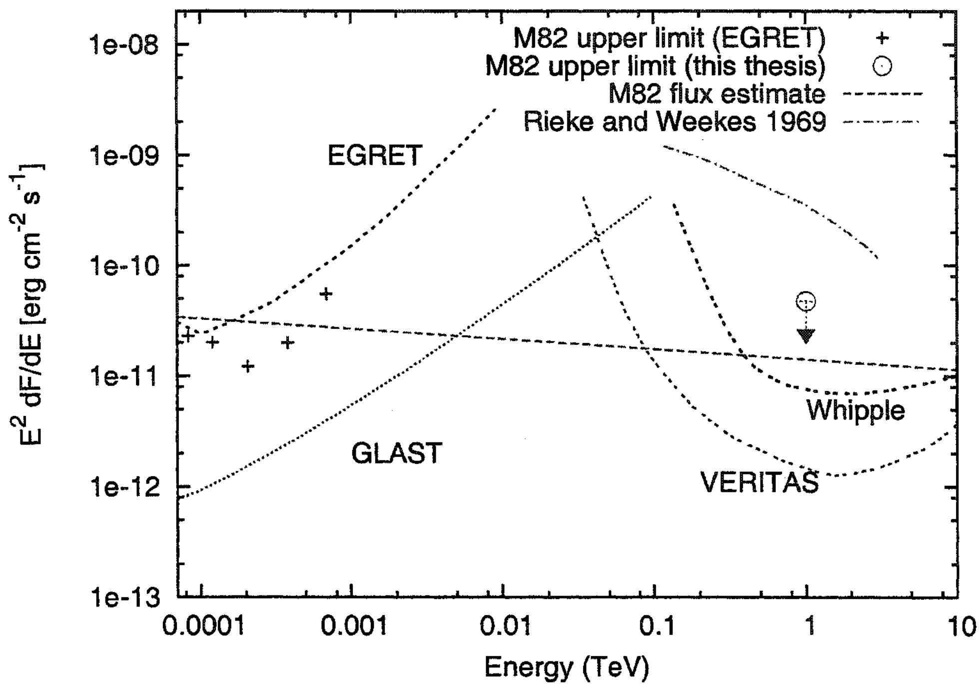

Figure 6.21. Flux estimate for M82 with flux upper limits. Sensitivities of EGRET, GLAST, Whipple, and VERITAS are also plotted (see Figure 1.1 for details). A curve of differential gamma-ray flux predicted as a result of IC with CR electrons is also shown (calculated from integrated flux curve presented by Rieke and Weekes 1969 [115]).

capability of stereoscopic observation, which allows a much higher efficiency of background rejection and considerably improved determination of the arrival direction and energy of the primary (see Figure 6.22 and 6.23). For a single telescope, images made by local muons are similar to the gamma-ray images and are the dominant background at low energies ($\leq$ 200 GeV). Stereoscopic observation eliminates these events at the trigger level, vastly reducing the background. The construction and testing of all four VERITAS telescopes are planned to be completed by the end of 2006.

6.3 Conclusion

The sources and mechanisms of VHE CR acceleration have long remained unknown. SNRs are believed to be the sites of the acceleration of CRs with energies

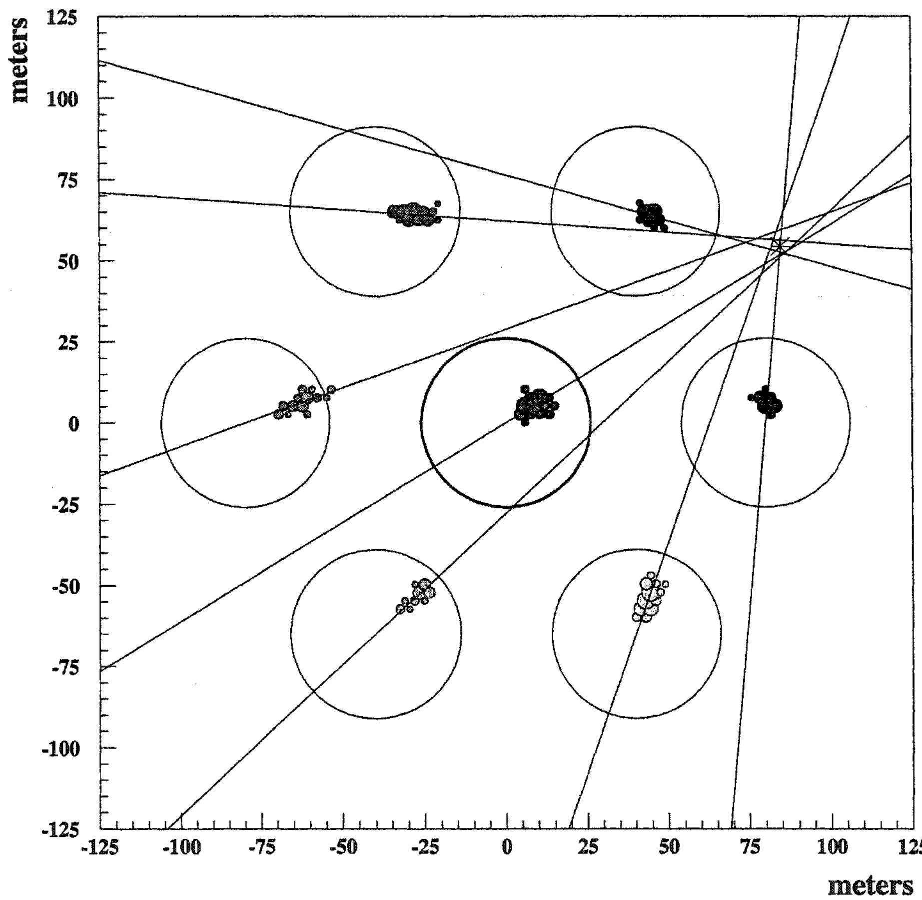

Figure 6.22. Schematic of stereo detection of a gamma-ray event. The direction and impact point of the shower core can be reconstructed using stereo images of the shower.

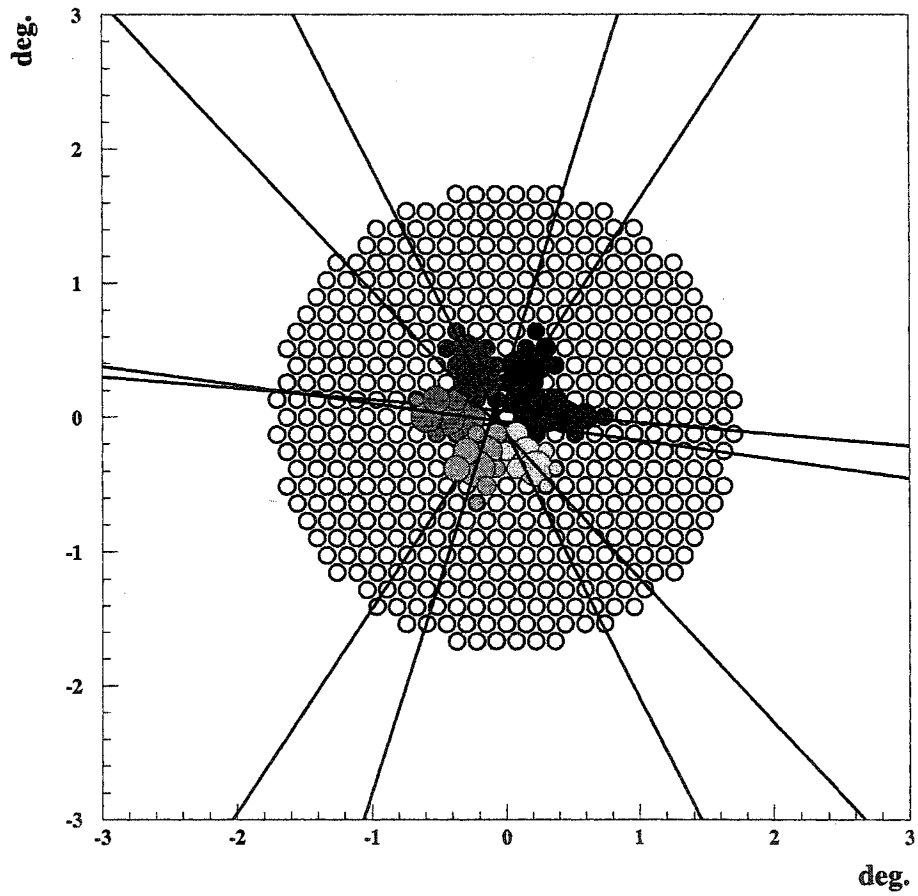

Figure 6.23. Superimposed gamma-ray event images from each camera enables reconstruction of arrival direction of the primary.

up to $\sim 10^{15}$ eV. SBGs are astronomical objects which provide plausible indirect evidence of acceleration of hadronic CRs, through emission of gamma rays from neutral pion decay produced in interactions between proton CRs and ISM nuclei. In SBGs, cumulative enhancement of VHE gamma-ray emission is expected due to the combination of critical parameter values, such as SN rate, ISM density, and local magnetic field strength. Detection of these gamma rays with energy ≥ 100 GeV is most efficiently done by ground-based IACTs which have large effective gamma-ray collecting areas of $\sim 10^5$ m^2.

TeV gamma-ray observations of SBGs promising for high energy emission were conducted by the Whipple 10m IACT at the Fred Lawrence Whipple observatory between 2001 and 2004. The SBGs, M81, M82, NGC3079, and IC342 were selected based on an estimation of the VHE gamma-ray flux and on their morphology and characteristics at other wave bands such as X-ray, IR, and radio. Although the observations by the Whipple telescope resulted in a null detection, the derived upper limits are consistent with the estimates. They do not exclude possibilities of VHE gamma-ray emission from SBGs produced by hadronic CR interaction with ISM gas nuclei. The estimates indicate that the flux of VHE gamma rays from the SBGs may be detectable with enough exposure by the next generation of IACTs, such as VERITAS, due to their improved sensitivities. Observations by EGRET set upper limits for M82 in energy range from ~ 70 MeV to ~ 1 GeV [78]. The limits constrain our flux estimate for M82 to be about three times smaller if a power-law-like spectrum is assumed. However, it does not exclude the possibility for M82 to be observable by the VERITAS (see Figure 6.21) even under such conservative assumptions.

The gamma-ray emissions from SBGs are diffusive and quasi-steady in nature and thus provide new possibilities, such as measuring the EBL. Direct measurement of the EBL in the mid and far IR region is impossible due to the relatively large zodiacal light and the Galactic star light foregrounds. However, indirect measurement can be done by investigation of the attenuation of high energy spectrum of distant objects, resulting from pair production absorption, which takes place when VHE gamma rays propagate through cosmological distances. AGN have been utilized to set upper limits of EBL spectral density. The intrinsic, highly variable gamma-ray radiation of AGN are not well understood due to the lack of knowledge of the gamma-ray production mechanism in the vicinity of the black hole or AGN jets. The time variability of the VHE gamma-ray spectrum of AGN produces additional complications. Study of VHE gamma-ray emitting SBGs may provide a more stable measure of the EBL with a better understood emission mechanism if such sources are detected at distances > 100 Mpc. The detection of a large number of SBGs is essential in using their VHE gamma-ray emission to measure the EBL. Since IACTs are not effective instruments for all sky gamma-ray surveys due to limited FOV, complementary information from next-generation satellite gamma-ray instruments, such as GLAST, is important to establish a detection of the large number of sources, and then characterize them with VERITAS observations.

APPENDIX

IMAGE PARAMETRIZATION

The image parameters used in this dissertation are difined as [116]

$$
\begin{aligned}
q &= \int_A \rho(x_1, x_2) da && \text{(A.1)} \\
d_{x_i} &= \int_A \rho(x_1, x_2) x_i da && \text{(A.2)} \\
Q_{x_i x_j} &= \int_A \rho(x_1, x_2) x_i x_j da && \text{(A.3)} \\
\widetilde{Q}_{x_i x_j} &= \frac{Q_{x_i x_j}}{q} - \frac{d_{x_i} d_{x_j}}{q^2} && \text{(A.4)} \\
d &= \widetilde{Q}_{x_1 x_1} - \widetilde{Q}_{x_2 x_2} && \text{(A.5)} \\
z &= \sqrt{d^2 + 4\widetilde{Q}^2_{x_1 x_2}} && \text{(A.6)}
\end{aligned}
$$

and

$$
\begin{aligned}
SIZE &= q && \text{(A.7)} \\
(LENGTH)^2 &= \frac{\widetilde{Q}_{x_1 x_1} + \widetilde{Q}_{x_2 x_2} + z}{2} && \text{(A.8)} \\
(WIDTH)^2 &= \frac{\widetilde{Q}_{x_1 x_1} + \widetilde{Q}_{x_2 x_2} - z}{2} && \text{(A.9)}
\end{aligned}
$$

where, $i, j = 1, 2$. x_1, x_2 are the coordinates of the camera plane, da is an infinitesmal area segment of the camera, and $\rho(x_1, x_2)$ is digitized charge (qADC) density at a point (x_1, x_2). A schematic picture of a gamma-ray image with these parameters is shown in Figure 5.12.

REFERENCES

[1] Hartman, R. C. *et al.* The Third EGRET Catalog of High-Energy Gamma-Ray Sources. *Astrophysical Journal Supplements* **123**, 79–202 (1999).

[2] Weekes, T. C. *Very High Energy Gamma-ray Astronomy* (The Institute of Physics Publishing, Bristol, UK, 2003).

[3] Punch, M. *et al.* Detection of TeV photons from the active galaxy Markarian 421. *Nature* **358**, 477–478 (1992).

[4] Muraishi, H. *et al.* Evidence for TeV gamma-ray emission from the shell type SNR RX J1713.7-3946. *Astronomy & Astrophysics* **354**, L57–L61 (2000).

[5] Aharonian, F. A. *et al.* High-energy particle acceleration in the shell of a supernova remnant. *Nature* **432**, 75–77 (2004a).

[6] Aharonian, F. *et al.* Evidence for TeV gamma ray emission from Cassiopeia A. *Astronomy & Astrophysics* **370**, 112–120 (2001).

[7] Itoh, C. *et al.* Detection of diffuse TeV gamma-ray emission from the neaby starburst galaxy NGC 253. *Astronomy & Astrophysics* **396**, L1–L4 (2002).

[8] Tsuchiya, K. *et al.* Detection of Sub-TeV Gamma Rays from the Galactic Center Direction by CANGAROO-II. *Astrophysical Journal Letters* **606**, L115–L118 (2004).

[9] Kosack, K. *et al.* TeV Gamma-Ray Observations of the Galactic Center. *Astrophysical Journal Letters* **608**, L97–L100 (2004).

[10] Aharonian, F. *et al.* Very high energy gamma rays from the direction of Sagittarius A*. *Astronomy & Astrophysics* **425**, L13–L17 (2004b).

[11] Fleysher, R., Nemethy, P. & for the Milagro Collaboration. Discovery of Diffuse TeV Gamma-Ray Emission from the Galactic Plane. *ArXiv Astrophysics e-prints* (2005).

[12] Weekes, T. C. *et al.* Observation of TeV gamma rays from the Crab nebula using the atmospheric Cerenkov imaging technique. *Astrophysical Journal* **342**, 379–395 (1989).

[13] Hillas, A. M. *et al.* The Spectrum of TeV Gamma Rays from the Crab Nebula. *Astrophysical Journal* **503**, 744–759 (1998).

[14] Nolan, P. L. *et al.* Observations of the Crab pulsar and nebula by the EGRET telescope on the Compton Gamma-Ray Observatory. *Astrophysical Journal* **409**, 697–704 (1993).

[15] Dolan, J. F. *et al.* The high-energy X-ray spectrum of the Crab Nebula observed from OSO-8. *Astrophysical Journal* **217**, 809–814 (1977).

[16] Buckley, J. H. *et al.* Constraints on cosmic-ray origin from TeV gamma-ray observations of supernova remnants. *Astronomy & Astrophysics* **329**, 639–658 (1998).

[17] Fegan, S. TeV observations of SNRs and unidentified sources. *ArXiv Astrophysics e-prints* (2001).

[18] Koyama, K. *et al.* Evidence for Shock Acceleration of High-Energy Electrons in the Supernova Remnant SN:1006. *Nature* **378**, 255–256 (1995).

[19] Mastichiadis, A. & de Jager, O. C. TeV emission from SN 1006. *Astronomy & Astrophysics* **311**, L5–L8 (1996).

[20] Koyama, K. *et al.* Discovery of Non-Thermal X-Rays from the Northwest Shell of the New SNR RX J1713.7-3946: The Second SN 1006? *Publications of the Astronomical Society of Japan* **49**, L7–L11 (1997).

[21] Enomoto, R. *et al.* The acceleration of cosmic-ray protons in the supernova remnant RX J1713.7-3946. *Nature* **416**, 823–826 (2002).

[22] Thompson, D. J. *et al.* SAS-2 galactic gamma-ray results. 1: Diffuse emission. In *The Structure and Content of the Galaxy and Galactic Gamma Rays*, 3–14 (1977).

[23] Hermsen, W. COS-B views on the diffuse Galactic gamma-ray emission and some point sources. *Space Science Reviews* **49**, 17–39 (1988).

[24] Sreekumar, P. *et al.* EGRET Observations of the Diffuse Gamma Ray Emission from the Galactic Plane. *Bulletin of the American Astronomical Society* **25**, 846 (1993).

[25] Hunter, S. D. *et al.* EGRET Observations of the Diffuse Gamma-Ray Emission from the Galactic Plane. *Astrophysical Journal* **481**, 205–240 (1997).

[26] Sreekumar, P. *et al.* Observations of the Large Magellanic Cloud in high-energy gamma rays. *Astrophysical Journal Letters* **400**, L67–L70 (1992).

[27] Torres, D. F., Reimer, O., Domingo-Santamaría, E. & Digel, S. W. Luminous Infrared Galaxies as Plausible Gamma-Ray Sources for the Gamma-Ray Large Area Space Telescope and the Imaging Atmospheric Cerenkov Telescopes. *Astrophysical Journal Letters* **607**, L99–L102 (2004).

[28] Volk, H. J., Aharonian, F. A. & Breitschwerdt, D. The Nonthermal Energy Content and Gamma-Ray Emission of Starburst Galaxies and Clusters of Galaxies. *Space Science Reviews* **75**, 279–297 (1996).

[29] Lieu, R., Ip, W.-H., Axford, W. I. & Bonamente, M. Nonthermal Origin of the EUV and Soft X-Rays from the Coma Cluster:Cosmic Rays in Equipartition with the Thermal Medium. *Astrophysical Journal Letters* **510**, L25–L28 (1999).

[30] Primack, J. R., Bullock, J. S., Somerville, R. S. & MacMinn, D. Probing galaxy formation with TeV gamma ray absorption. *Astroparticle Physics* **11**, 93–102 (1999).

[31] Vassiliev, V. V. Extragalactic background light absorption signal in the TeV gamma-ray spectra of blazars. *Astroparticle Physics* **12**, 217–238 (2000).

[32] Vassiliev, V. V. TeV Observations and Extragalactic Background Light. *APS Meeting Abstracts* A3006 (2002).

[33] Ressell, M. T. & Turner, M. S. The Grand Unified Photon Spectrum A Coherent View of the Diffuse Extragalactic Background Radiation. *Bulletin of the American Astronomical Society* **22**, 753 (1990).

[34] Quinn, J. *et al.* Detection of Gamma Rays with E > 300 GeV from Markarian 501. *Astrophysical Journal Letters* **456**, L83–L86 (1996).

[35] Wright, E. L. COBE observations of the cosmic infrared background. *New Astronomy Review* **48**, 465–468 (2004).

[36] Schubnell, M. S. Time Variability in the TeV Gamma Ray Emission from the Blazar Markarian 421. *Bulletin of the American Astronomical Society* **26**, 1467 (1994).

[37] Amenomori, M. *et al.* Observation of Multi-TEV Gamma Rays from the Crab Nebula using the Tibet Air Shower Array. *Astrophysical Journal Letters* **525**, L93–L96 (1999).

[38] Atkins, R. *et al.* Observation of TeV Gamma Rays from the Crab Nebula with Milagro Using a New Background Rejection Technique. *Astrophysical Journal* **595**, 803–811 (2003).

[39] Matthews, J. & Pierre Auger Observatory Collaboration. Status and Performance of the Pierre Auger Observatory. *AAS/High Energy Astrophysics Division* **8**, 34.03 (2004).

[40] Jackson, J. D. *Classical Electrodynamics* (John Wiley & Sons, New York, 1975).

[41] Čerenkov, P. A. *Dokl.Acad.Nauk SSSR* **2**, 451 (1934).

[42] Frank, I. M. & Tamm, I. E. *Dokl.Acad.Nauk SSSR* **14**, 107 (1937).

[43] Rossi, B. & Greisen, K. Cosmic-Ray Theory. *Reviews of Modern Physics* **13**, 240–309 (1941).

[44] Gaisser, T. K. *Cosmic Rays and Particle Physics* (Cambridge University Press, Cambridge and New York, 1990).

[45] Hillas, A. M. Differences between Gamma-Ray and Hadronic Showers. *Space Science Reviews* **75**, 17–30 (1996).

[46] Rao, M. V. S. & Sreekantan, B. V. *Extensiv Air Showers* (World Scientific, Singapore, 1998).

[47] Ginzburg, V. L. & Syrovatskii, S. I. *The Origin of Cosmic Rays* (Macmillan, New York, 1964).

[48] Berezhko, E. G. & Völk, H. J. Kinetic theory of cosmic ray and gamma-ray production in supernova remnants expanding into wind bubbles. *Astronomy & Astrophysics* **357**, 283–300 (2000).

[49] Marcaide, J. M. *et al.* How is really decelerating the expansion of SN1993J? In *Proceedings of the 6th EVN Symposium*, 239 (2002).

[50] Ilovaisky, S. A. & Lequeux, J. A Study of Galactic Supernova Remnants. II. Supernova Rate, Galactic Radio Emission and Pulsars. *Astronomy & Astrophysics* **20**, 347–356 (1972).

[51] Berkhuijsen, E. M. Supernova rate and the number of supernova remnants in M31, M33 and the Galaxy. *Astronomy & Astrophysics* **140**, 431–440 (1984).

[52] van den Bergh, S. & McClure, R. D. Supernova rates and galaxy inclinations. *Astrophysical Journal* **359**, 277–279 (1990).

[53] Tammann, G. A., Loeffler, W. & Schroeder, A. The Galactic supernova rate. *Astrophysical Journal Supplements* **92**, 487–493 (1994).

[54] Fermi, E. On the Origin of the Cosmic Radiation. *Physical Review* **75**, 1169–1174 (1949).

[55] Bell, A. R. The acceleration of cosmic rays in shock fronts. I. *Monthly Notices of the Royal Astronomical Society* **182**, 147–156 (1978a).

[56] Bell, A. R. The acceleration of cosmic rays in shock fronts. II. *Monthly Notices of the Royal Astronomical Society* **182**, 443–455 (1978b).

[57] Longair, M. S. *High Energy Astrophysics. An Informal Introduction for Students of Physics and Astronomy* (Cambridge University Press, Cambridge, 1981).

[58] Drury, L. On particle acceleration in supernova remnants. *Space Science Reviews* **36**, 57–60 (1983).

[59] Malkov, M. A. & Diamond, P. H. Modern theory of Fermi acceleration: A new challenge to plasma physics. *Physics of Plasmas* **8**, 2401–2406 (2001).

[60] Glaser, V. & Ferrell, R. A. Lifetime of the Neutral Pion. *Physical Review* **121**, 886–892 (1961).

[61] Ribas, I. Distances and fundamental properties of eclipsing binaries in the LMC and M31. In *Astronomical Society of the Pacific Conference Series*, 261–269 (2004).

[62] Matteucci, F., Renda, A., Pipino, A. & Della Valle, M. Modelling the nova rate in galaxies. *Astronomy & Astrophysics* **405**, 23–30 (2003).

[63] Kim, S. *et al.* A Neutral Hydrogen Survey of the Large Magellanic Cloud: Aperture Synthesis and Multibeam Data Combined. *Astrophysical Journal Supplements* **148**, 473–486 (2003).

[64] Torres, D. F. Theoretical Modeling of the Diffuse Emission of Gamma Rays from Extreme Regions of Star Formation: The Case of ARP 220. *Astrophysical Journal* **617**, 966–986 (2004).

[65] Lonsdale, C. J. *et al.* The time evolution of the radio supernovae in Arp 220. In *IAU Symposium*, 386+ (2001).

[66] Paglione, T. A. D., Jackson, J. M. & Ishizuki, S. The Average Properties of the Dense Molecular Gas in Galaxies. *Astrophysical Journal* **484**, 656–663 (1997).

[67] Gupta, M. & Webber, W. R. The abundance of N-14 at the cosmic-ray source - A study using new fragmentation cross sections. *Astrophysical Journal* **340**, 1124–1134 (1989).

[68] Ormes, J. & Freier, P. On the propagation of cosmic rays in the Galaxy. *Astrophysical Journal* **222**, 471–483 (1978).

[69] Coziol, R., Torres, C. A. O., Quast, G. R., Contini, T. & Davoust, E. The Pico DOS Dias Survey Starburst Galaxies. *Astrophysical Journal Supplements* **119**, 239–253 (1998).

[70] Gao, Y. & Solomon, P. M. HCN Survey of Normal Spiral, Infrared-luminous, and Ultraluminous Galaxies. *Astrophysical Journal Supplements* **152**, 63–80 (2004).

[71] Mannucci, F. *et al.* The infrared supernova rate in starburst galaxies. *Astronomy & Astrophysics* **401**, 519–530 (2003).

[72] van Buren, D. & Greenhouse, M. A. A more direct measure of supernova rates in starburst galaxies. *Astrophysical Journal* **431**, 640–644 (1994).

[73] Condon, J. J., Condon, M. A., Gisler, G. & Puschell, J. J. Strong radio sources in bright spiral galaxies. II - Rapid star formation and galaxy-galaxy interactions. *Astrophysical Journal* **252**, 102–124 (1982).

[74] Mauersberger, R., Henkel, C. & Chin, Y.-N. Dense gas in nearby galaxies. VIII. The detection of OCS. *Astronomy & Astrophysics* **294**, 23–32 (1995).

[75] Paglione, T. A. D., Jackson, J. M., Ishizuki, S. & Rieu, N. First Observations of extragalactic CSJ = 1 goes to 0. *Astronomical Journal* **109**, 1716–1723 (1995).

[76] Bayet, E., Gerin, M., Phillips, T. G. & Contursi, A. The submillimeter C and CO lines in Henize 2-10 and NGC 253. *Astronomy & Astrophysics* **427**, 45–59 (2004).

[77] Cappi, M. *et al.* Diffuse thermal emission from very hot gas in starburst galaxies. *Astronomy & Astrophysics* **350**, 777–790 (1999).

[78] Blom, J. J., Paglione, T. A. D. & Carramiñana, A. Diffuse Gamma-Ray Emission from Starburst Galaxies and M31. *Astrophysical Journal* **516**, 744–749 (1999).

[79] Itoh, C., Enomoto, R., Yanagita, S., Yoshida, T. & Tsuru, T. G. Galactic Gamma-Ray Halo of the Nearby Starburst Galaxy NGC 253. *Astrophysical Journal Letters* **584**, L65–L68 (2003).

[80] Karachentsev, I. D., Sharina, M. E., Dolphin, A. E. & Grebel, E. K. Distances to nearby galaxies around IC 342. *Astronomy & Astrophysics* **408**, 111–118 (2003).

[81] Krismer, M., Tully, R. B. & Gioia, I. M. IC 342/Maffei Group of Galaxies and Distances for Two of its Members. *Astronomical Journal* **110**, 1584–1587 (1995).

[82] Lo, K. Y. *et al.* Aperture synthesis observations of CO emission from the nucleus of IC 342. *Astrophysical Journal Letters* **282**, L59–L63 (1984).

[83] Downes, D. *et al.* HCN in the center of the galaxy IC 342. *Astronomy & Astrophysics* **262**, 424–432 (1992).

[84] Crosthwaite, L. P. *et al.* CO and Neutral Gas in the Disk of the Spiral Galaxy IC 342. *Astronomical Journal* **122**, 797–814 (2001).

[85] Becklin, E. E. *et al.* Infrared emission and star formation in the central regions of the galaxy IC 342. *Astrophysical Journal* **236**, 441–447 (1980).

[86] Turner, J. L. & Ho, P. T. P. VLA observations of massive star formation in spiral nuclei. *Astrophysical Journal Letters* **268**, L79–L83 (1983).

[87] Martin, R. N. & Ho, P. T. P. Hot gas in the nucleus of IC 342. *Astrophysical Journal Letters* **308**, L7–L10 (1986).

[88] Ho, P. T. P. & Martin, R. N. VLA observations of extragalactic NH3 in IC 342. *Astrophysical Journal* **272**, 484–487 (1983).

[89] Ho, P. T. P., Martin, R. N., Turner, J. L. & Jackson, J. M. VLA imaging of extragalactic ammonia - Hot gas in the nucleus of IC 342. *Astrophysical Journal Letters* **355**, L19–L22 (1990).

[90] Harris, A. I. *et al.* First observations of the CO J = 6-5 transition in starburst galaxies. *Astrophysical Journal Letters* **382**, L75–L79 (1991).

[91] Ishizuki, S., Kawabe, R., Ishiguro, M., Okumura, S. K. & Morita, K. A molecular gas bar fuelling starburst activity in galaxy IC342. *Nature* **344**, 224–226 (1990).

[92] Meier, D. S., Turner, J. L. & Hurt, R. L. Molecular Gas Properties of the Starburst Nucleus of IC 342: High-Resolution ^{13}CO (2-1) Imaging. *Astrophysical Journal* **531**, 200–209 (2000).

[93] Meier, D. S. & Turner, J. L. Molecular Gas and Star Formation in the Nucleus of IC 342: ^{18}CO and Millimeter Continuum Imaging. *Astrophysical Journal* **551**, 687–701 (2001).

[94] Boker, T., Forster-Schreiber, N. M. & Genzel, R. Near-Infrared Imaging Spectroscopy of IC 342: Evolution of a Bar-Driven Central Starburst. *Astronomical Journal* **114**, 1883–1898 (1997).

[95] Telesco, C. M., Dressel, L. L. & Wolstencroft, R. D. The genesis of starbursts and infrared emission in the centers of galaxies. *Astrophysical Journal* **414**, 120–143 (1993).

[96] Fabbiano, G. & Trinchieri, G. X-ray observations of spiral galaxies. II - Images and spectral parameters of 13 galaxies. *Astrophysical Journal* **315**, 46–67 (1987).

[97] Bregman, J. N., Cox, C. V. & Tomisaka, K. X-Ray Emission from the Starburst Galaxy IC 342. *Astrophysical Journal Letters* **415**, L79–L82 (1993).

[98] White, P. M. & Bothun, G. The Intrinsic Structure and Color of IC 342 from CCD Observations. *Publications of the Astronomical Society of the Pacific* **115**, 1135–1142 (2003).

[99] Athanassoula, E. Morphology of bar orbits. *Monthly Notices of the Royal Astronomical Society* **259**, 328–344 (1992).

[100] Schinnerer, E., Böker, T. & Meier, D. S. Molecular Gas and the Nuclear Star Cluster in IC 342: Sufficient Inflow for Recurring Star Formation Events? *Astrophysical Journal Letters* **591**, L115–L118 (2003).

[101] Böker, T., van der Marel, R. P. & Vacca, W. D. CO Band Head Spectroscopy of IC 342: Mass and Age of the Nuclear Star Cluster. *Astronomical Journal* **118**, 831–842 (1999).

[102] Ptak, A. & Griffiths, R. Hard X-Ray Variability in M82: Evidence for a Nascent Active Galactic Nucleus? *Astrophysical Journal Letters* **517**, L85–L89 (1999).

[103] Reichen, M., Kaufman, M., Blecha, A., Golay, M. & Huguenin, D. Far UV imaging of M 81 and comparison to other spiral tracers. *Astron. Astrophys. Suppl. Ser.* **106**, 523–554 (1994).

[104] Immler, S. & Wang, Q. D. ROSAT X-Ray Observations of the Spiral Galaxy M81. *Astrophysical Journal* **554**, 202–215 (2001).

[105] Swartz, D. A. *et al.* Chandra X-Ray Observations of the Spiral Galaxy M81. *Astrophysical Journal Supplements* **144**, 213–242 (2003).

[106] Filippenko, A. V. & Sargent, W. L. W. The kinematics of a violent outflow from the nucleus of the SC galaxy NGC 3079. *Astronomical Journal* **103**, 28–40 (1992).

[107] Veilleux, S. *et al.* The nuclear superbubble of NGC 3079. *Astrophysical Journal* **433**, 48–64 (1994).

[108] Sofue, Y. *et al.* Ultra-High-Density Molecular Core and Warped Nuclear Disk in the Deep Potential of Radio Lobe Galaxy NGC 3079. *Astrophysical Journal Letters* **547**, L115–L118 (2001).

[109] Mauersberger, R., Henkel, C., Wilson, T. L. & Harju, J. Dense gas in nearby galaxies. II - CS emission from spiral galaxies. *Astronomy & Astrophysics* **226**, L5–L8 (1989).

[110] Cawley, M. F. The Application of Noise Padding to the Cherenkov Imaging Technique. In *Towards a Major Atmospheric Cherenkov Detector – II for TeV Astro/Particle Physics*, 176 (1993).

[111] Kertzman, M. P. & Sembroski, G. H. Computer Simulation Methods for Investigating the Detection Characteristics of TeV Air Chenerkov Telescopes. *Nuclear Instruments and Methods in Physics Research* **343**, 629–643 (1994).

[112] Li, T. P. & Ma, Y. Q. Analysis methods for results in gamma-ray astronomy. *Astrophysical Journal* **272**, 317–324 (1983).

[113] Helene, O. Upper limit of peak area. *Nuclear Instruments and Methods in Physics Research* **212**, 319–322 (1983).

[114] Pohl, M. On the predictive power of the minimum energy condition. 2: Fractional calorimeter behaviour in the diffuse high energy gamma emission of spiral galaxies. *Astronomy & Astrophysics* **287**, 453–462 (1994).

[115] Rieke, G. H. & Weekes, T. C. Production of Cosmic Gamma Rays by Compton Scattering in Discrete Sources. *Astrophysical Journal* **155**, 429–437 (1969).

[116] Reynolds, P. T. *et al.* Survey of candidate gamma-ray sources at TeV energies using a high-resolution Cerenkov imaging system - 1988-1991. *Astrophysical Journal* **404**, 206–218 (1993).